STRUCTURAL ANALYSIS OF A JET TRAINER COCKPIT

A THESIS SUBMITTED TO
THE GRADUATE SCHOOL OF NATURAL AND APPLIED SCIENCES
OF
MIDDLE EAST TECHNICAL UNIVERSITY

BY

MUHİTTİN NAMİ ALTUĞ

IN PARTIAL FULFILLMENT OF THE REQUIREMENTS
FOR
THE DEGREE OF MASTER OF SCIENCE
IN
AEROSPACE ENGINEERING

FEBRUARY 2012

Approval of the thesis:

STRUCTURAL ANALYSIS OF A JET TRAINER COCKPIT

submitted by **MUHİTTİN NAMİ ALTUĞ** in partial fulfillment of the requirements for the degree of **Master of Science in Aerospace Engineering Department, Middle East Technical University** by,

Prof. Dr. Canan Özgen _____
Dean, Graduate School of **Natural and Applied Sciences**

Prof. Dr. Ozan Tekinalp _____
Head of Department, **Aerospace Engineering**

Assist. Prof. Dr. Melin Şahin _____
Supervisor, **Aerospace Engineering Dept., METU**

Examining Committee Members:

Prof. Dr. Yavuz YAMAN _____
Aerospace Engineering Dept., METU

Assist. Prof. Dr. Melin ŞAHİN _____
Aerospace Engineering Dept., METU

Assist. Prof. Dr. Demirkan ÇÖKER _____
Aerospace Engineering Dept., METU

Assist. Prof. Dr. Ercan GÜRSES _____
Aerospace Engineering Dept., METU

Dr. Muvaffak HASAN _____
Chief Engineer, TAI

Date: 10.02.2012

I hereby declare that all information in this document has been obtained and presented in accordance with academic rules and ethical conduct. I also declare that, as required by these rules and conduct, I have fully cited and referenced all material and results that are not original to this work.

Name, Last Name : Muhittin Nami Altuğ

Signature :

ABSTRACT

STRUCTURAL ANALYSIS OF A JET TRAINER COCKPIT

Altuğ, Muhittin Nami
M.Sc., Department of Aerospace Engineering
Supervisor: Assist. Prof. Dr. Melin Şahin

February 2012, Pages 128

This thesis presents structural analysis of a cockpit of a jet trainer type aircraft and the correlation studies performed by using ground pressurisation test results. For this purpose, first the response of the complex integrated fuselage structure is investigated under the complex type cabin pressure load. Then, cockpit part of the fuselage structure is modelled using commercial finite element software MSC/PATRAN® and MSC/NASTRAN®. The finite element model (FEM) of the cockpit structure is improved by the examination of the ground pressurisation test data and is finalised after achieving a good correlation between the finite element analysis (FEA) and the test results. This final form of the FEM of the cockpit structure serving as a benchmark is proved to be reliable for any future modifications.

Keywords: Structural Analysis, Jet Trainer Aircraft, Cockpit, Finite Element Modelling and Analysis, Experimental Correlation

ÖZ

BİR JET EĞİTİM UÇAĞI KOKPİTİNİN YAPISAL ANALİZLERİ

Altuğ, Muhittin Nami
Yüksek Lisans, Havacılık ve Uzay Mühendisliği Bölümü
Tez Yöneticisi : Yrd. Doç. Dr. Melin Şahin

Şubat 2012, 128 sayfa

Bu tez, bir jet eğitim uçağı kokpitinin yapısal analizlerini ve yer basınçlandırma test sonuçları ile korelasyonu çalışmalarını sunmaktadır. Ulaşılmak istenen nihai amaca yönelik, ilk olarak bütünleşik gövde yapısının karmaşık bir yük türü olan kabin basıncı yükü altında davranışı incelenmiştir. Sonra, gövdenin kokpite ait bölgesi MSC/PATRAN® ve MSC/NASTRAN® ticari sonlu elemanlar yazılımları kullanılarak modellenmiştir. Kokpite ait bu sonlu elemanlar modeli yer basınçlandırma test verileri incelenerek geliştirilmiş ve sonlu elemanlar analizleri ile test sonuçları arasında iyi bir korelasyon sağlanmasıyla da son halini almıştır. Bu çalışma ile ayrıca kokpit modelinin elde edilmiliş bu son halinin ileriki çalışmalara güvenilir bir referans teşkil edeceği de ispatlanmıştır.

Anahtar Kelimeler: Yapısal Analiz, Jet Eğitim Uçağı, Kokpit, Sonlu Elemanlar Model ve Analizi, Deneysel Korelasyon

to my Mami

ACKNOWLEDGMENTS

I would like to express my gratitude to my supervisor Assist Prof. Dr. Melin Şahin for his guidance and patience throughout this study.

I must also express my appreciation to my superiors at TAI, Dr. Gürsel Erarslanoğlu and Dr. Muvaffak Hasan for providing me the necessary data and their guidance.

I want to thank my colleagues Ali Baki Uygur, Ömer Faruk Türkmen and Selçuk Topçu for their help and perfect performance during the ground pressurisation test.

I would also like to thank my colleagues Enver Özakkaş, Bilgin Çelik, Muhsin Öcal, Zuhal Gökbulut, Abdulkadir Çekiç, Emre Ünay, Engin Kahraman, Fatih Mutlu Karadal, Derya Gürak, Ahmet Ufuk Yavuz, Mehmet Efruz Yalçın and Erdoğan Tolga İnsuyu for giving me the strength to complete this work.

Last, but not least, I would like to express my deepest thanks to my sister Rihal and her husband Martin for their endless support and Eda for her support at every stage of this study, understanding and love.

TABLE OF CONTENTS

LIST OF TABLES

TABLES

LIST OF FIGURES

FIGURES

CHAPTER 1

INTRODUCTION

1.1 Motivations of the Study

Because of very high procurement and operating costs for the new-generation jet trainer aircrafts, modernization of the older aircrafts has become inevitable for many countries. Also, aircrafts are forced to be modernised for efficiency and safety reasons according to the constantly updated international aviation rules. Modernization programs for the jet trainer aircrafts are generally carried out in two main branches: modernization of avionic systems and structural modifications. Avionics in the aircrafts are installed especially in the cockpit region in order to improve the human-machine interface for the pilots. Installations of the avionic equipments in the cockpit are performed with support structures and sometimes these supports may change the main load path of the fuselage structure. In addition, for the older aircrafts, aging problem of the metal fuselage structure has become a dangerous situation over the years. Structural modification of the fuselage is generally the most economical solution to extend the life of the aircraft. For the non-manufacturer countries that have purchased jet trainer aircraft from another country, load path information on the aircraft is very critical at the beginning of the structural modification. Under the operational static loads, each sub-structure of the integrated fuselage structure shares the loads according to their design. Especially under complex loads, for example cabin pressure, predicting these load distributions among

the structures is a very hard task. Because under cabin pressure, the responses of the sub-structures of the fuselage not only depend on their own elastic properties, but also strictly depend on boundary conditions, i.e. their form of integration. Under the light of these requirements, fuselage structure modernization in a jet trainer aircraft is a must for the non-manufacturer countries, hence, there is an immense need to construct an experimentally validated high-fidelity finite element models.

1.2 Objectives of the Study

The objectives of this study can be listed as follows:

- Investigating the load carrying/transfer mechanism of the cockpit structure
- Having a detailed FEM of the cockpit structure
- Investigating the complex type cabin pressure load
- Having the response of the complex integrated fuselage structure
- Obtaining a methodology for strain gauge (SG) testing
- Performing a correlation study
- Validating FEM via experimental test results

1.3 Literature Survey

The importance of air dominance in the defence of countries is increasing. This is only possible with air force equipped with the most modern aircrafts and highly-qualified personnel. A combat pilot training is a laborious as well as a costly job. Technological developments and major advances in warfare aircrafts also bring up the necessity of the development of jet trainer aircrafts and the systems for the pilot training.

Today, in many countries, training aircrafts are about to complete their lives or do not meet the requirements of the day. The difficulties in operation and maintenance

of the current training aircrafts are effective in forcing the need for innovation and development in this field.

Especially together with advances in the field of electronics, digital displays and easy-use control panels are integrated to the last generation jet aircrafts. Thus, the possibility of collection of more sensitive data has emerged. Using this information during a high speed manoeuvre gives rise to the search for a more ergonomic environment for the pilot. Avionic modernizations for the jet trainer aircrafts, therefore, become inevitable.

Today in the world, there are different kinds of jet trainer aircrafts used by many countries. The famous company Northrop Grumman produced 1,187 T-38s between 1959 and 1972, the year in which the production program ended. Today, from those aircrafts, nearly half of them are still in service by U.S. Air Force, U.S. Navy, NASA (Figure 1.3.1) and air forces around the world. Since 1961, more than 70,000 Air Force pilots have been trained in the T-38. The average T-38 has flown 15,000 hours, and the high-time aircraft has flown 19,000 hours. T-38 is maintained by the production of replacement wings and new structural components to make the service life of the platform longer. T-38s are currently going through structural and avionics programs (T-38C) to extend their service life to 2020 [1].

Figure 1.3.1: NASA Dryden's T-38 trainer aircraft in flight over Cuddeback Dry Lake in Southern California [2]

Another jet trainer, namely Dassault/Dornier Alpha Jet-E has been sold to a number of countries in Africa and in the Middle East and this jet trainer aircraft modernised to Alpha Jet-3 (Lancier). In this aircraft, multi-functional controls and a glass cockpit that will train pilots in the use of navigation and attack systems of the latest and future generation fighter aircraft are fitted [3].

BAE Hawk, another jet trainer, is used in a wide range of air forces for training purposes. Hawk is modernised lots of times and there are lots of variants of it. The Advanced Jet Trainer, the latest version of Hawk trainers, is equipped with glass cockpit, inertial navigation, and other improvements [4].

Also, Northrop Grumman F-5B, Aermacchi MB-339, L-39 Albatross, G-4 Super Galeb are some of the examples for jet trainers, having ongoing modernization programs today.

Fuselage Structure

The fuselage is the main structure or body of the aircraft. The function of an aircraft fuselage is to provide support for the following structures: structure for wings and tail, structure that contains the cockpit for the pilot and structure that allows aircraft to carry cargo, passengers, and other equipments. In single-engine aircraft, it also hoses the power plant. One type of fuselage structure is the monocoque fuselage that uses formers, frame assemblies and bulkheads to give shape to the fuselage, and it relies on the skin to carry the primary stresses. A very crucial problem related to monocoque construction is sustaining enough strength while keeping the weight within allowable limits. To overcome this problem, a modification, namely semi-monocoque construction, was developed. In addition to formers, frame assemblies, and bulkheads, the semi-monocoque construction has the skin reinforced by longitudinal members. Primary bending loads are taken by the longerons. They are supplemented by other longitudinal members, called stringers. Bulkheads, frames and formers are the vertical structural members of the fuselage. These vertical members are located at intervals to carry concentrated loads and at points where fittings are used to attach other units, such as the wing, power plant, stabilizers, etc. [5]. The members of the semi-monocoque construction are shown in Figure 1.3.2.

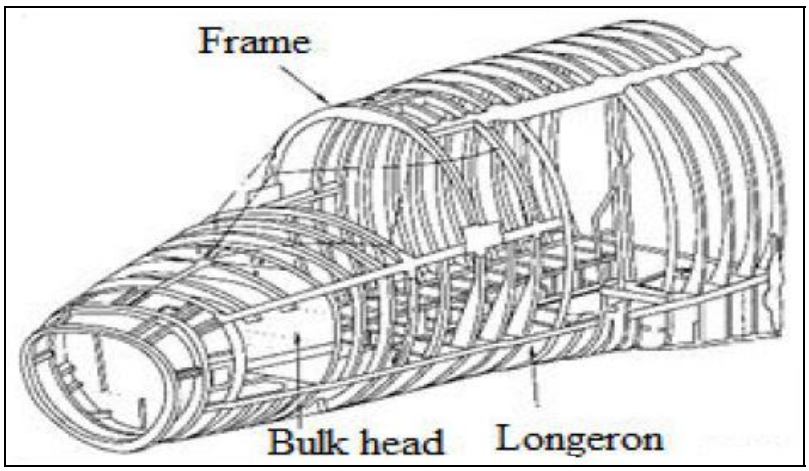

Figure 1.3.2: Semi-monocoque construction [5]

Fuselage structures are subject to various types of loads. There are differences in the generation of these loads. Aerodynamic forces on the fuselage skin are relatively low; on the other hand, the fuselage supports large concentrated loads resulted from the attachments such as wing and landing gear and it carries payloads, which may cause large inertia forces. Furthermore, for aircrafts designed for high altitude flight, the fuselage structure must resist internal pressure [6].

The jet fuselage geometry is composed of three parts: a tapered nose section, forward fuselage that involves cockpit and rear fuselage [7].

Canopy and Windshield

The need for visibility for the pilot of an aircraft and for protecting himself against the wind stream has placed emphasis on the design of canopy and windshield. The visibility is provided by the transparent materials which are recently made up of composite materials. The shape of the canopy is based on streamlining requirements regarding aerodynamic efficiency. The development of aircrafts with pressurised cabins introduced complications. The need for high mechanical strength without adding excessive weight to withstand the cabin pressures resulted in decreased window areas and in curved surfaces to obtain strength without excessive weight [9]. Canopy and windshield on the aircraft is shown in Figure 1.3.3.

Figure 1.3.3: Alpha Jet-E, Canopy and Windshield structures [10]

Cabin Pressurisation

Inside a pressurised cabin, people can be transported comfortably and safely for long duration, especially if the cabin altitude is maintained at 8.000 [ft], or below, where the use of oxygen equipment is not required. Pressurised air is pumped into fuselage by cabin superchargers which release a relatively constant volume of air at all altitudes up to a designed maximum. From the fuselage the device called outflow valve releases the air. Since the superchargers provide a constant inflow of air to the pressurised area, the outflow valve, by regulating the air exit, is the major controlling element in the pressurisation system. The degree of pressurisation and, therefore, the operating altitude of the aircraft are limited by several critical design factors. Primarily the fuselage is designed to withstand a particular maximum cabin differential pressure. Cabin differential pressure is the ratio between inside and outside air pressures and is a measure of the internal stress on the fuselage skin. If the differential pressure becomes too high, structural damage to the fuselage may occur [5].

Finite Element Theory

Classical analytical methods consider a differential element and develop the governing equations, usually in the form of partial differential equations. When applied to real-life problems, it is often difficult to obtain an exact solution to these equations considering complex geometry and boundary conditions. The finite element method (FEM) can be defined simply as a method of finding approximate solutions for partial differential equations [11].

FEM requires a problem defined in geometrical domain to be subdivided into a finite number of smaller regions (a mesh). These regions are connected at points called nodes. Element behaviour is approximated in terms of nodal variables called degrees of freedom. Elements are assembled considering loading and boundary conditions. The governing equations in the FEM are integrated over each finite element and the solution assembled over the entire problem domain. Consequently, a set of finite linear equations in terms of a set of unknown parameters is obtained over each element. Solution of these equations is performed using linear algebra techniques [12], [13].

In engineering problems, unknowns are infinite in a continuum. The finite element procedure reduces such unknowns to a finite number by expressing the unknown field variables in terms of assumed approximating functions (interpolating functions/shape functions) within each element. The approximating functions are defined in terms of field variables of nodes. Thus in the FEM, the unknowns are the field variables of the nodal points. Once these are found, the field variables at any point can be found by using interpolation functions [14].

Steps in finite element analysis can be summarised as follows:

- Selecting suitable field variables and the elements.
- Discretising the continuum
- Selecting interpolation functions
- Finding the element properties/stiffness
- Assembling element properties/global stiffness to get global properties.
- Imposing the boundary conditions and loading conditions.
- Solving the system equations to get the nodal unknowns.
- Making the additional calculations to get the required values [14], [15].

FEM Construction

For many structural Finite Element Analysis (FEA) applications, there are always decisions made by the design or analytical engineer on just how to simplify a real structure into a simulation model.

Successful simplification depends on;

- Understanding the physics of the problem
- Understanding the behaviour of the elements
- Selecting the correct element, the number of elements and their distribution
- Critically evaluating the results and making modification in the conceptual model to improve the accuracy [16].

While simplifying a structure into a model, one can use coarse, fine and very fine meshes. Each type of these meshes serves for different analysis purposes. The ultimate decision of combining these different types is complicated and subjective [17]. There are many sub-components of aircraft. Since they are interacting with each other, they form a complex environment causing boundaries and loading conditions on the aircraft to be complex too. Guessing load paths that result from

these conditions can be a hard task. Figure 1.3.4 shows the complexity of airframe structure.

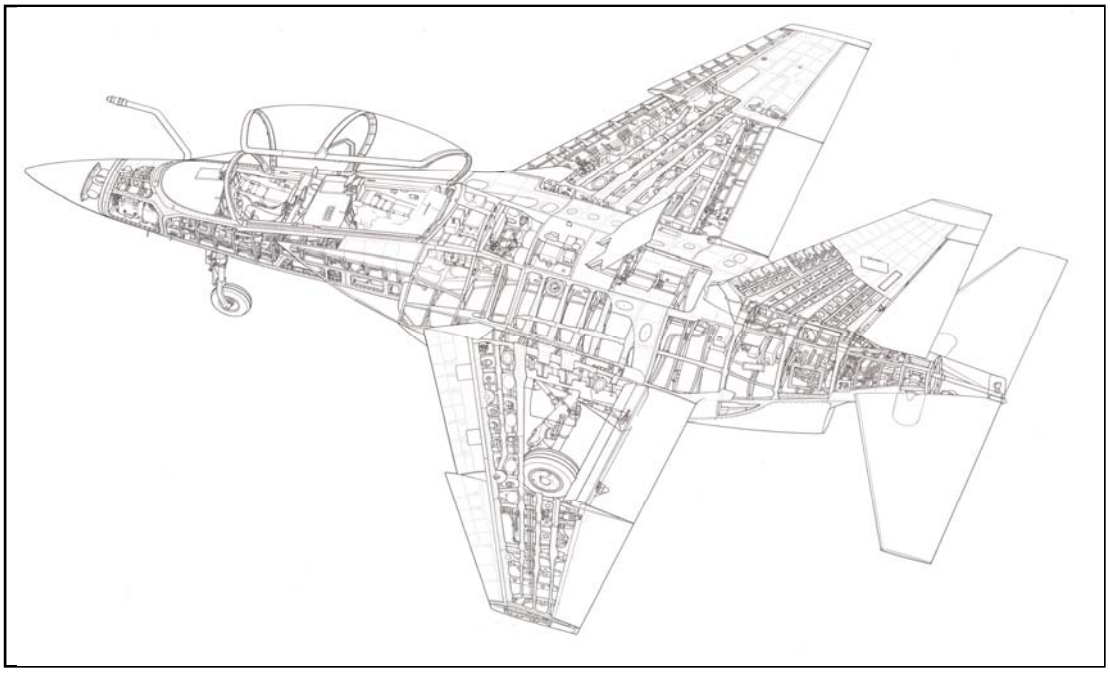

Figure 1.3.4: Aermacchi M-346 cutaway drawing [18]

In making an analysis of large structural components such as a wing, fuselage etc., modelling with simple (low order) elements is most desirable. These simple models can provide reasonably accurate information about the overall load paths, and the simplicity of the elements allows easier interpretation of the results. They are also ideal for parametric studies in preliminary design and optimisation. The use of higher order elements is appropriate while making a detailed analysis of local areas, such as a plate with cut-out or a crack or local buckling of a panel etc. [17].

Modelling of the complex structural components with low order elements as mentioned above is the essence of Global FEM. The main objective of the Global FEM is to reproduce the global stiffness and overall load paths. Global FEM contains enough detail to accurately describe the structural behaviour. It includes the major

structural elements. The Global FEM does not use detailed models for components and it is a collection of several individual models (Figure 1.3.5).

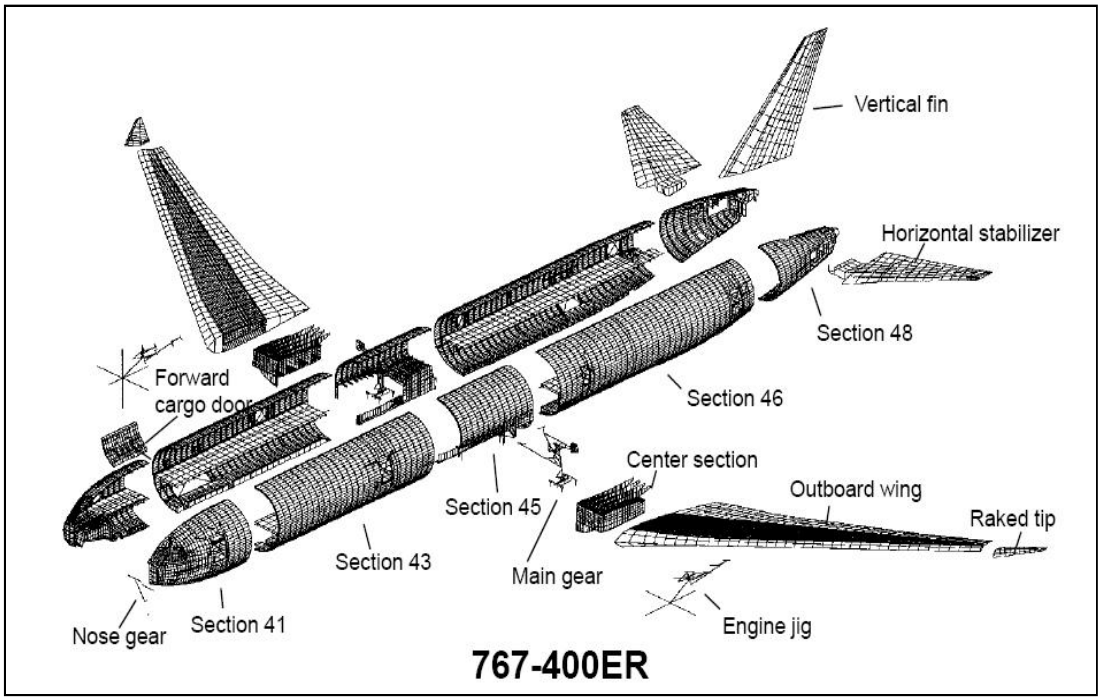

Figure 1.3.5: Integrated FEM for Boeing 767-400ER [17]

Advantages:

- Easier to find errors.
- Use simple elements.
- Use simple modelling concepts.
- Keep the model size small [19].

Since the 1990s, all primary structures of commercial airplanes like the B777 and A340 are certified using such FEM analysis [20]

A given structure which is too complex for classical analysis can be solved by FEM in a powerful way for determining stresses and deflections. The method appears complex due to the fact that thousands of elements or members of an airframe

structure have each its own set of equations. Because of the very large number of equations and corresponding data involved, finite element method is only possible when performed by computer [21].

Many commercial programs use finite element analysis methods, to name a few, ANSYS® [22], ABAQUS® [23], MSC.Patran® /MSC.Nastran® [24]. In this thesis MSC.Patran®/ MSC.Nastran® are used since it is well appreciated in aerospace industry and can be well-suited for aerospace applications.

Structural Testing

Despite encouraging results from simulation and experimental modelling, structural testing is still a valuable tool in the industrial development of product and process. Through testing, the response of the structure under applied loads (force, pressure, temperature, shock, vibration and other loading conditions) is determined. Its success depends on careful choice of testing method, instrumentation, data acquisition, and allocation of resources [25].

Structural Testing Activities

Structural testing has three major steps. The first one is the planning of the test. At this phase, the requirements and the type of test are specified. Examples of different types can be full scale, coupon tests and quality assurance tests. The second step is the preparation. This step involves specifying load type, magnitude of loading and making the loading equipments and subsystems ready for the test. Also instrument and subsystem calibrations are made at this stage. The final step is the execution. This refers to obtaining data from transducers and processing data which involves data transmission, signal conditioning etc. [25]

Strain Gauges as Measuring Devices

The purpose of a strain gauge is to convert the physical changes occurring in a structure due to applied loading into an electrical change, usually by altering voltage or current [25]. Three types of strain gauges are used on airframe fatigue and static tests for measuring strain. These are axial, shear, and rosette gauges, as shown in Figure 1.3.6.

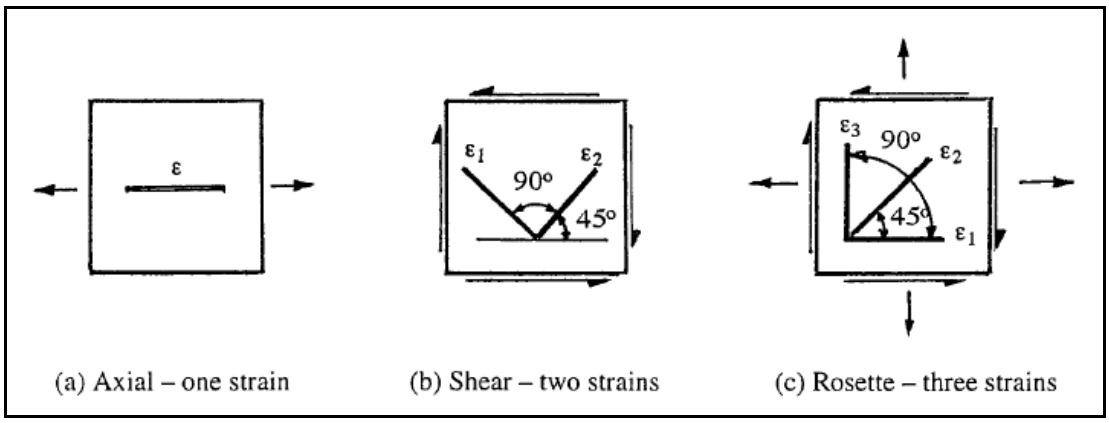

Figure 1.3.6: Strain gauge types [25]

In some cases a single strain gauge will provide sufficient information. In many cases, however, two or more strain gauges will be necessary to supply the information necessary to calculate the stresses. Two-dimensional stress state can often be used as an adequate model for actual stress distributions. In this case the positions of the strain gauges must be carefully chosen, taking into account the stresses which are of interest. If the principal directions are known, strains of interest can be measured by a $0^0/90^0$ rosette. If the principal directions are not known, three armed rosettes will be required [27].

Temperature Compensation

Some errors may occur during the measurement. One of the sources of errors can be environmental factors, for example. These factors may be temperature, humidity, corrosive atmospheres, electromagnetic noise, etc. [26].

If there is no temperature compensation, during a test under temperature effects, output signals from strain gauges are not related only to strains that are expected to be generated by the applied load. One should also consider the temperature effect in the test results. To suppress temperature effects, a dummy gauge should be placed on a non-deforming area on the structure to be tested. As it is normally impossible to find a non-deforming area, the gauge is usually bonded on a small sheet of a material corresponding to that of the component. This sheet is attached to the structure as close as possible to the active gauge. It is recommended to use active and dummy gauges from the same batch in order to obtain the same tolerances for the gauge factor and to keep temperature effects as low as possible [27].

Correlation

The certification rule for the validation of the FEM that is to be used for the structural analysis is stated as follows below;

"Analyses including finite element models used in place of tests must be demonstrated to be reliable for the structure under evaluation and the load levels that have to be covered. This would normally be provided by correlation with experimental results on the same structure or through comparison with other known and accepted methods and results or through a combination of both" [28]

1.4 Limitations of the Study

In this study, only the cockpit part of the jet trainer fuselage is investigated.

In the static analysis, cabin pressure load is applied to the model. The model is solved by the algorithm of linear static analysis. Assumptions of the analysis are the following: displacements are small, stiffness matrix and boundary conditions do not change and displacements are directly proportional to the loads.

In the detailed FEM of the cockpit structure, canopy was not modelled due to the lack of information about the canopy hook mechanism, which is responsible for locking the canopy to the longerons. Under internal pressure, at the cockpit region, modelling of the canopy becomes unnecessary when the hook mechanism information is missing. Because the level and the type of the load transferred from canopy to the longerons depend on the stiffness and behaviour of the mechanism. Instead of modelling, canopy-hook loads were gathered from the manufacturer company.

Opposed to the canopy, windshield structure is modelled except its transparent part. The transparent structure is not modelled because a material property of that part is unknown. In this situation, the moments on the longerons exerted by the windshield pressure loads has to be neglected.

Another assumption is concerned with a plastic sealant which is located between the canopy and the longerons. The working principle of these plastic sealants is to stick the canopy to the fuselage when air pressure, namely sealant pressure, is given inside the sealants. So under the cabin pressure, this simple sticking mechanism prevents the pressure leakage from the cabin. In detailed FEM, it is not concerned due to unknown contact loads occurring between canopy and the longerons.

In the real structure of the model, there is a canopy drive mechanism which is responsible for opening and closing the canopy. In the mechanism there is a drive shaft, which lays between the bushings of the canopy support fittings. These fittings are located either side of the aircraft. In the study, canopy support fittings and drive shaft are not modelled. It is thought that modelling these structures does not have a very large impact on the load path of the cockpit under cabin pressure. Also modelling the fittings brings an additional run time to the FEM.

In addition, in the FEM, the primary structures are modelled according to Global FEM approach. Fasteners and fittings are not modelled for assembling the primary structures. Because there are lots of different types of fasteners in the aircraft, modelling the fasteners with assigning each of their stiffness is time-consuming. However, at some local points where necessary, rigid-type elements are used for connection. Also cut-outs, except longeron, are not modelled based on the same Global FEM approach.

Strain gauge installations are bounded on the aircraft by the limitations of the minimum space required for the installation. The reason is that structure to be modified is already assembled and the environmental condition for the labour is not the same with the condition during the production phase. For the manufacturer company, it is easier to install the strain gauges on the desired parts before the assembly.

In static test, ground pressurisation is applied into the cockpit. Also, there is no temperature compensation used during the test because the test is performed approximately at room temperature.

1.5 Contents of the Study

This study is composed of five chapters. The first chapter is the introduction which involves literature survey that gives background information for the main topics of the study. Limitations of the study are also included in this chapter. The second chapter is about the modelling and the analysis parts of the study. In this particular chapter, finite element modelling techniques are presented in detail. The third chapter is concerned with ground pressurisation test. The procedure of the test is mainly described and the results are presented and discussed. The fourth chapter is about the correlation between the finite element analysis and the test results. The final chapter presents the concluding remarks and recommendations for future work.

CHAPTER 2

FINITE ELEMENT MODELING AND ANALYSIS OF COCKPIT STRUCTURE

2.1 Introduction

In this section, finite element model of a jet trainer type cockpit structure is constructed and static analysis is performed within the framework of finite element analysis techniques. Firstly, cockpit sub-structures and their structural functions are described. Secondly, finite element model construction and model verification methods are presented. Then, finite element analysis is performed by applying the loads and boundary conditions specified to the model.

2.2 Structural Model of the Cockpit

The cockpit structure consists of a typical semi-monocoque structure. The primary structures of the cockpit such as longerons, frames, bulkheads and skins are assembled for resisting the cockpit to the manoeuvre, aerodynamic and internal pressure loads. As a general feature of a jet trainer aircraft, there are two cockpits in the structural model which are; a student (front) cockpit and an instructor (rear) cockpit. In the model, the right and the left sides of the cockpit regions are

structurally and geometrically symmetric. General view of the cockpit structure is shown in Figure 2.2.1.

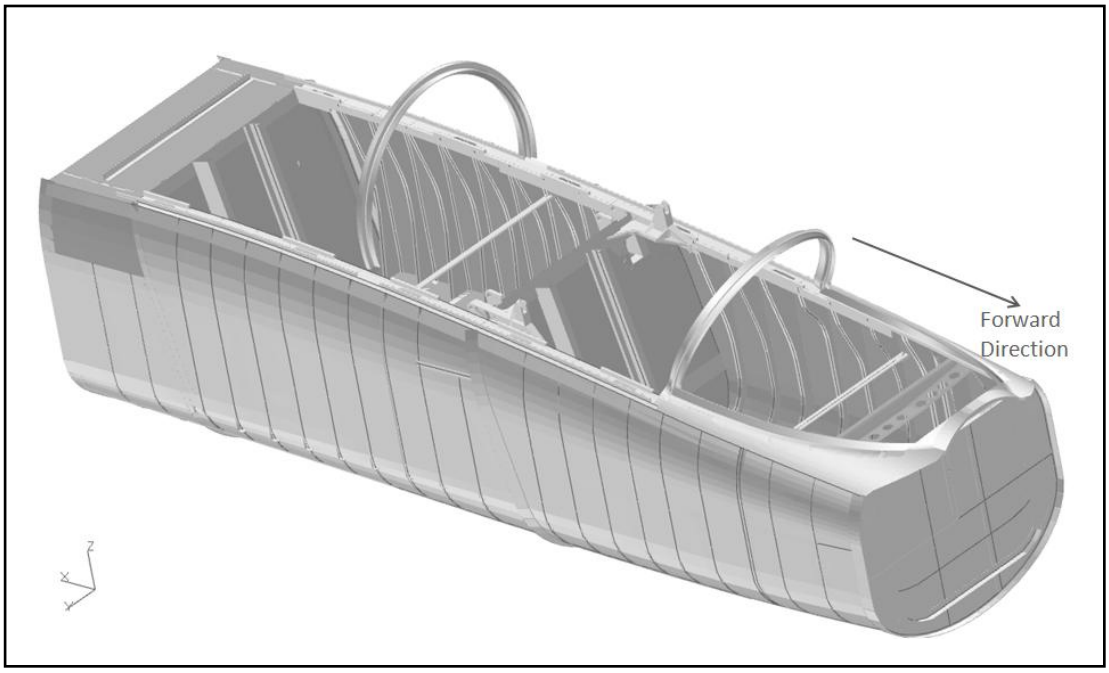

Figure 2.2.1: General view of cockpit structure

The modelled structure is composed of upper and lower longerons locating through the cockpits, side skins extending between upper and lower longerons and frames which are symmetrically placed on the two sides of the cockpit. There are two types of frames in the model that are called continuous and discontinuous frames. Continuous frames are formed with side frames and bottom frames lying between the lower longerons. Side and bottom frames are attached to the lower longerons. Discontinuous frames consist of only the side frames. Between some of the frames there are also intercostals. Also there are bulkheads, floors and decks to complete the primary structures of the model. Bulkheads have stiffeners with side, upper and lower caps to reinforce their main webs. In addition to the stiffeners and caps, seating rails are modelled on the bulkheads which are located at the back of the pilot's ejection seat. Floor webs are reinforced with the help of floor beams and webs of the

decks are also reinforced with stiffeners. Because structural analysis will be done under specified load condition, potentially critical structures that can significantly affect the validation of the study are added to the model. These are the tie bars, sheet support, windshield and horse shoe which are connected between two-sides of the cockpit. Normally, it is expected that canopies which are connected to the upper longerons and canopy support fittings are comprised in the complete cockpit model. However, canopies and canopy support fittings are not modelled in this study. Figure 2.2.2 shows the description and the placements of the structures in the cockpit.

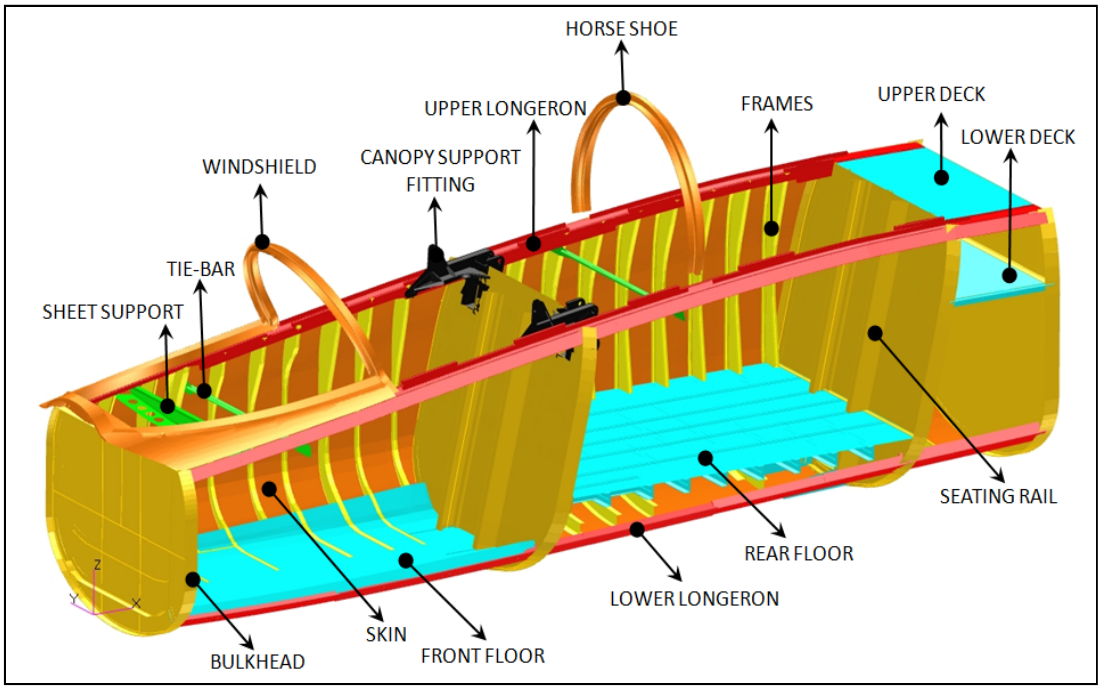

Figure 2.2.2: Descriptions of the cockpit structures

In the assembly, each primary structure has specific functions. The upper longeron mainly carries the axial loads from primary fuselage bending. In addition to this, it is subjected to lateral bending induced by cockpit and canopy pressures and aerodynamic forces. The supporting structure for the upper longeron under the lateral loads is provided by the bulkheads and tension ties. The upper longeron also transfers the vertical components of the windshield and canopy lock loads to the

adjacent frames. The lower longeron carries only axial load due to primary fuselage bending. The side skin panels carry fuselage shear flows and transfer the differential air pressures to the frames and bulkheads. The floor is subjected to cockpit pressure and shear flows due to fuselage net side loads. The frames react the external and internal pressure loads and distribute the net loads to the fuselage side skin and floor. The decks support the aft bulkhead of the cockpit and it carries a portion of the net side shear load of the fuselage. Horse shoe is one of the supporting member of the canopies and sheet support which lays between the upper longerons share the side loads of the longeron.

The functionalities of the modelled structures are provided with proper and sufficient attachments between the structures. Attachments are made with using fasteners, fittings or splices. In this study, the real structures of these kinds of attachments are not modelled. Instead of this, the functions of the attachments are simulated with some techniques, described in detail in this chapter.

The horizontal locations of the any structure in the cockpit are defined by taking the bulkhead and frame locations as the reference. The numbering of the bulkheads and frames is made sequentially from front through the back of the cockpit. Figure 2.2.3 shows the bulkhead and frame numbering in the cockpit. Here, B and F stand for bulkhead and frame respectively.

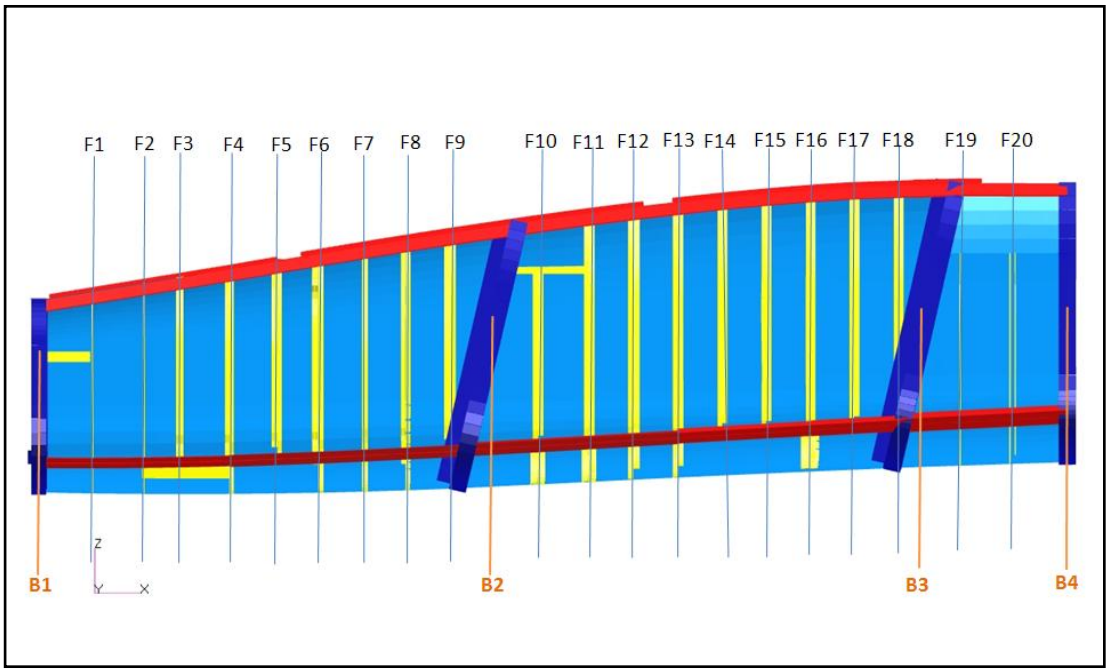

Figure 2.2.3: Bulkhead & Frame numbering

Side frames, intercostals and longerons are located symmetrically and the numbers of these structures are equal on both sides of the cockpit. The number and the locations of the structures involved in the model are given in Table 2.2.1 below.

Table 2.2.1: The number and location of the structures in the cockpit.

Part	Location	Number	Part	Location	Number
Frame (side)	F1	2	Bulkhead Web	B1	1
Frame (side)	F2	2	Bulkhead Web	B2	1
Frame (side)	F3	2	Bulkhead Web	B3	1
Frame (side)	F4	2	Bulkhead Web	B4	1
Frame (side)	F5	2	Bulkhead Caps	B1	4
Frame (side)	F6	2	Bulkhead Caps	B2	4
Frame (side)	F7	2	Bulkhead Caps	B3	4
Frame (side)	F8	2	Bulkhead Caps	B4	4
Frame (side)	F9	2	Bulkhead Stiffeners	B1	9
Frame (side)	F10	2	Bulkhead Stiffeners	B2	6
Frame (side)	F11	2	Bulkhead Stiffeners	B3	8
Frame (side)	F12	2	Bulkhead Stiffeners	B4	1
Frame (side)	F13	2	Skin	B1-B4	1
Frame (side)	F14	2	Upper Longeron	B1-B4	2
Frame (side)	F15	2	Lower Longeron	B1-B4	2
Frame (side)	F16	2	Front Floor Web	B1-B2	1
Frame (side)	F17	2	Front Floor Beams	B1-B2	2
Frame (side)	F18	2	Rear Floor Web	B2-B3	1
Frame (side)	F19	2	Rear Floor Beams	B2-B3	15
Frame (side)	F20	2	Upper Deck Web	B3-B4	1
Frame (bottom)	F1	1	Upper Deck Stiffeners	B3-B4	3
Frame (bottom)	F2	1	Lower Deck Web	B3-B4	1
Frame (bottom)	F4	1	Lower Deck Stiffeners	B3-B4	7
Frame (bottom)	F6	1	Windshield	B1-F5	1
Frame (bottom)	F7	1	Horse Shoe	F12-F13	1
Frame (bottom)	F8	1	Intercostal	B1-F1	2
Frame (bottom)	F10	1	Intercostal	F2-F4	2
Frame (bottom)	F11	1	Intercostal	F10-F11	2
Frame (bottom)	F12	1	Seating Rail	B2	1
Frame (bottom)	F13	1	Seating Rail	B3	1
Frame (bottom)	F16	1	Sheet Support	F1	1
Frame (bottom)	F19	1	Tie-Bar	F3	1
Frame (bottom)	F20	1	Tie-Bar	F12	1
TOTAL NUMBER OF THE STRUCTURES = 146					

2.3 Finite Element Model of the Cockpit

For the structural analysis purposes, finite element modelling (FEM) techniques are utilized in order to obtain mathematical model of the real structures. However, true simulation firstly depends on having a strong knowledge on the physical behaviour of the problem. Then, simplification begins with selecting the correct elements for the structures. As the complexity of the model increases, decision for combining these simplified elements becomes a difficult task.

In this study, the cockpit structure is modelled by using Global FEM approach. Global FEM contains enough detail to accurately describe the structural behaviour of the large models, in this case, a cockpit. The main objective of this type of modelling is to obtain global stiffness and overall load paths by using low order elements. The cockpit structure has lots of sub-structures in it. However, only the primary structures are modelled. Each primary component is simplified according to their structural missions in the cockpit. Based on this approach, fasteners, fittings and splices are not modelled at the connection regions. However, rigid type elements are used at some local points where necessary. Also cut-outs on the primary structures, except longeron cut-outs, are not modelled for the simplification reasons.

In model, canopy is not modelled due to the lack of information about the canopy hook mechanism. Cabin pressure reactions of the canopy are transmitted by the canopy hooks through the upper longerons of the cockpit. Because the hook mechanism information is missing, modelling of the canopy becomes unnecessary. Also, plastic sealants between the canopy and the upper longerons are not modelled due to the hardly predictable contact loads. In addition, canopy support fittings and drive shaft are not modelled due to the reasons that modelling these structures does not affect the load path significantly and it brings an additional run time to the FEM.

Selection of the Elements

In order to satisfy the designated strength to weight ratio, aircraft structures are generally formed with combination of thin panels with their longitudinal and transverse stiffeners. These stiffeners provide out of plane resistance for the panels. For the frames, bulkheads, floor and deck, in this study, the idealization is made such that webs of the structures are modelled with 2-D CQUAD4 (quadrangle) and CTRIA3 (triangle) elements and stiffeners are modelled by using CBEAM (1-D) elements. In this manner, web is modelled to resist mainly the shear load while beam elements resist mainly the bending and also shear loads with webs. In stiffened panels, to obtain a correct bending load distribution, offsets are given to the bar element neutral axis according to the thicknesses of the bars and the panels. During the design phases, conservative approach could be made with assigning CROD element properties to the frame, floor and deck stiffeners. In that way, initial sizing of a shear resistance web could be made. Also, during the simplification of the stiffeners, CROD element could be sufficient instead of using CBEAM element according to the load path. However in this study, because of the reason that the investigation is made for the existing structure, CBEAM elements are preferred to CROD elements. CTRIA3 elements are used only regions where CQUAD4 element generation is painful. Because it has higher stiffness property than CQUAD4 element, CTRIA3 element is not preferred for the simulation of the panel structures.

The structures that have major thickness variation, such as machined parts, are modelled by using CTETRA (3-D) solid elements. The reason is that the chamfers or flanges on the machined parts provide an additional stiffness to the main body of the part. In order to include this effect in the model, CTETRA element is used due to its better topological properties.

Also in the model, multi point constraint elements (MPC's) are used to connect the parts and distribute the point loads to the structures. There are two types of MPC elements used in the model. One of them is RBE2 element (Rigid Body Element-

Type 2) which is used for connection purposes. RBE2 element simulates the fasteners with its infinite stiffness. Deformations of the parts that connected to each other are directly transmitted with these elements. However, fasteners have finite stiffness values and deformations are not transmitted directly. Second MPC type used in the model is RBE3 element (Rigid Body Element-Type 3) which is for load distribution purposes. It distributes concentrated loads from a specified location to the other points that are connected to it. Distribution is made by considering the relative distances of the other points to the specified point.

The general view of the FEM of the cockpit structure is shown in Figure 2.3.1. In the figure, bar elements are displayed in their 1-D form.

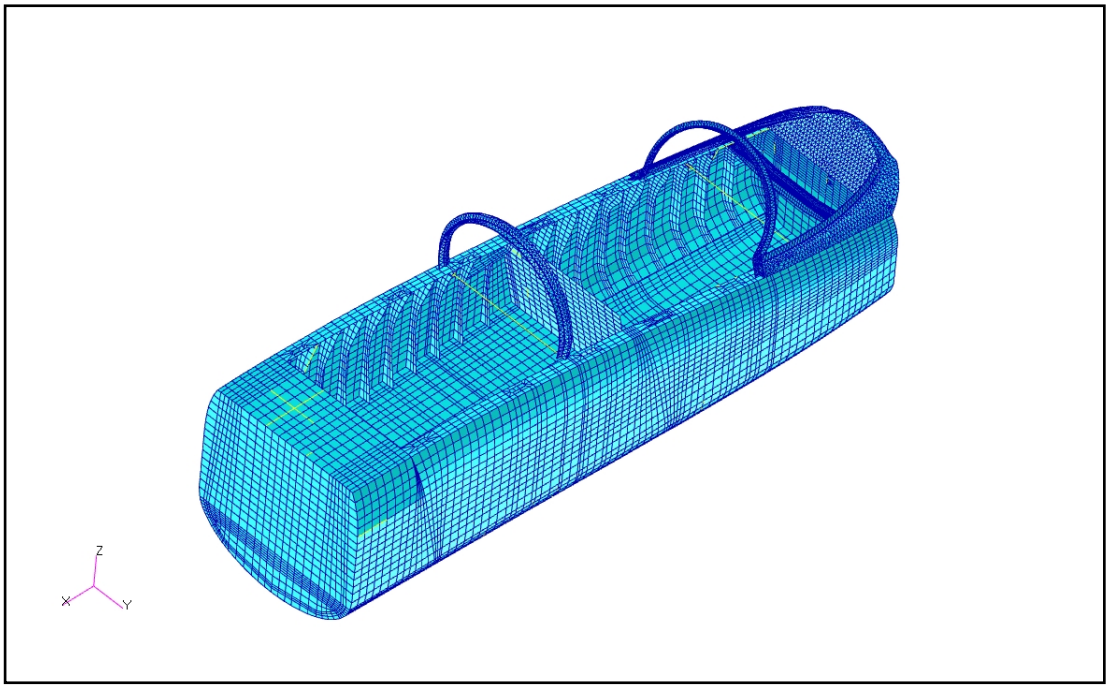

Figure 2.3.1: General view of cockpit FEM

The number of the elements and grid points (nodes) used in the model is given in Table 2.3.1.

Table 2.3.1: The number of the elements and grid point used in the model

Element Type	**Number**
CBEAM	4781
CQUAD4	18313
CTETRA	43971
CTRIA3	133
RBE2	96
RBE3	10
GRID POINTS	**108627**

Upper Longerons

Upper longeron is designed mainly for carrying the primary fuselage bending loads. Also it supports the windshield and the canopies. Because of these missions, it has form of a U-shape beam. Thus, there are three sections on the longerons called; web which supports the windshield and the canopies, outer flange which is connected with the skin and inner flange which supports the lateral structures of the cockpit. While web is modelled with CQUAD4 elements, outer and inner flange of the upper longeron is modelled by using CBEAM elements. Also at the canopy hook locations, webs are stiffened locally with hook flanges. Hook flanges are also modelled with CBEAM elements. For the distribution of the canopy loads to the upper longerons, RBE3 elements are used at the location of canopy hook cut-outs. There are totally five hook locations on one side of the cockpit. Two of them are at the front cockpit and three of them are placed at the rear cockpit. The detailed FEM of the upper longeron is shown in Figure 2.3.2.

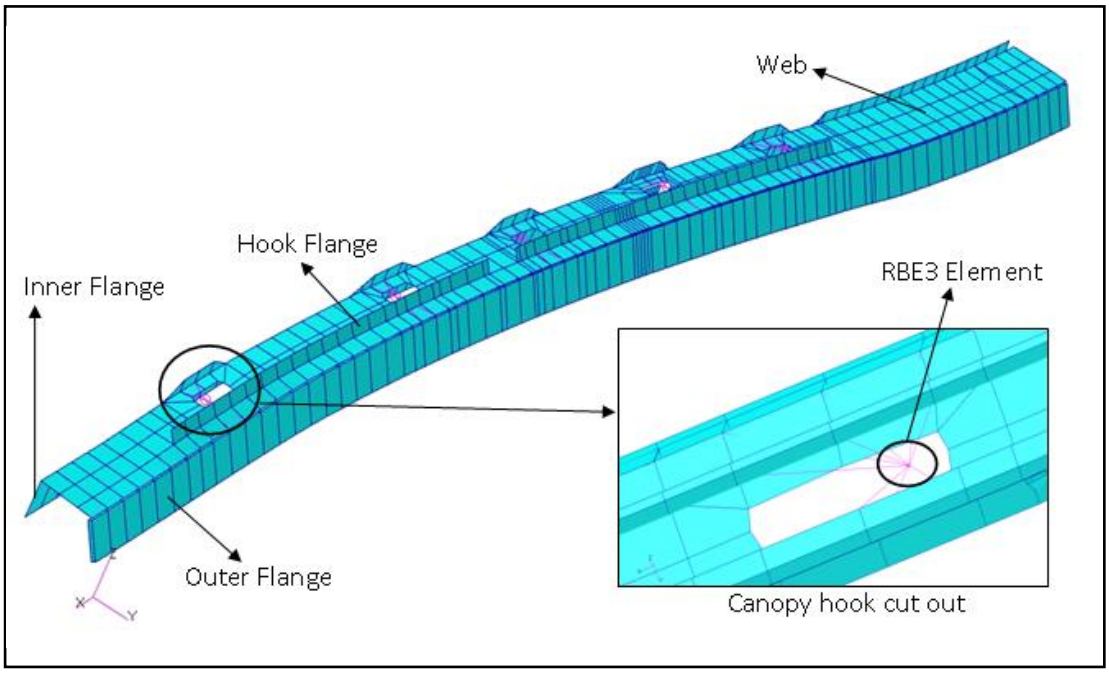

Figure 2.3.2: Detailed FEM of the upper longeron

Lower Longerons

Another fuselage bending carrying member of the cockpit is the lower longeron. Its form consists of a tapered T- shape beam. Lower longeron is connected to the skin from its base. Both sides of the lower longeron support the side and the bottom frames. At front cockpit, floor is connected to the outer side of the longeron. Lower longeron is modelled with CBEAM elements. The detailed FEM of the lower longeron is shown in Figure 2.3.3.

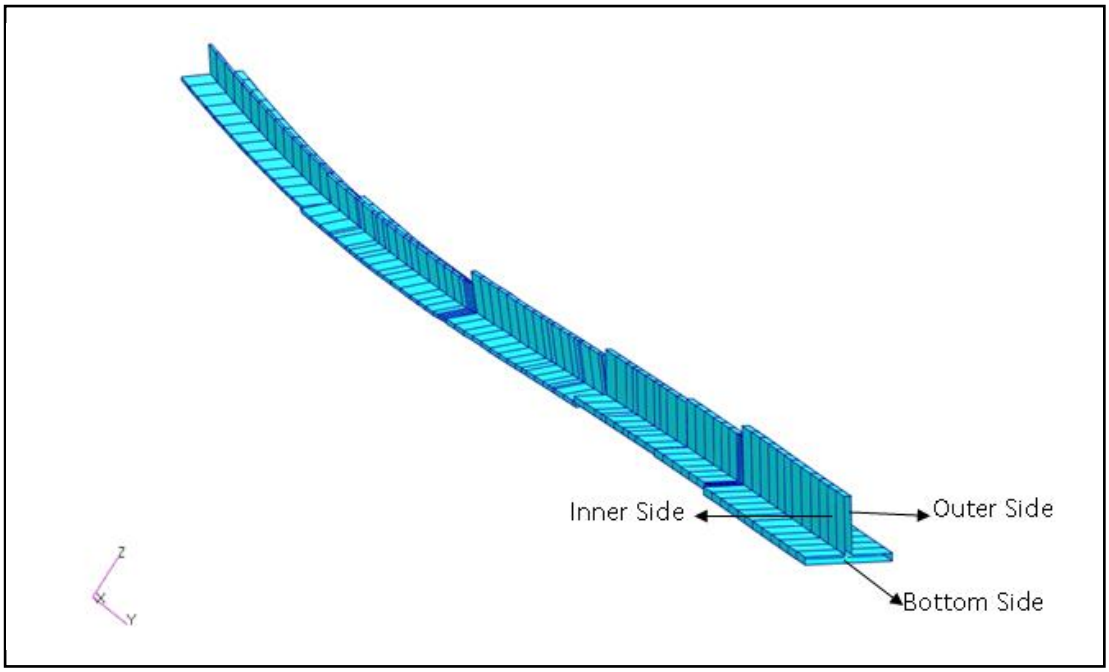

Figure 2.3.3: Detailed FEM of the lower longeron

Frames

Frame structure consists of three parts which are inner cap, web and the outer cap. The cross section is in Z and U-shape. Inner and outer cap are reinforcement members and prevent the frame web from buckling. For the continuous frames, side and the bottom frames are connected to the both sides of the lower longerons. Also there are intercostals between some frames. Intercostals carry a portion of longitudinal compression loads of the fuselage to prevent the skin from buckling. These structures, like frames, formed with web and flanges. For the frames and intercostals, the caps and flanges are modelled with CBEAM elements. While only CQUAD4 elements are used for modelling the intercostals webs, in addition to CQUAD4 elements, CTRIA3 elements are also used to model the frame webs. CTRIA3 elements are generated at the connection points of the lateral structures such as tie-bars. The detailed FEM of the frames and the intercostals is shown in Figure 2.3.4 and Figure 2.3.5 respectively.

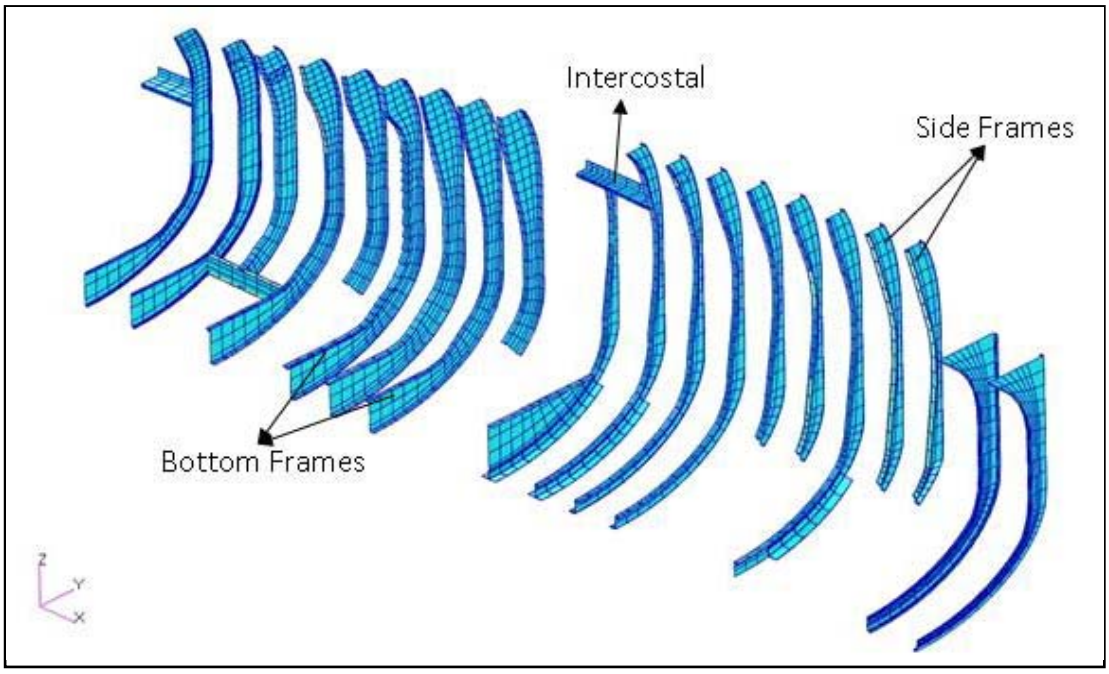

Figure 2.3.4: Detailed FEM of the frames and intercostals

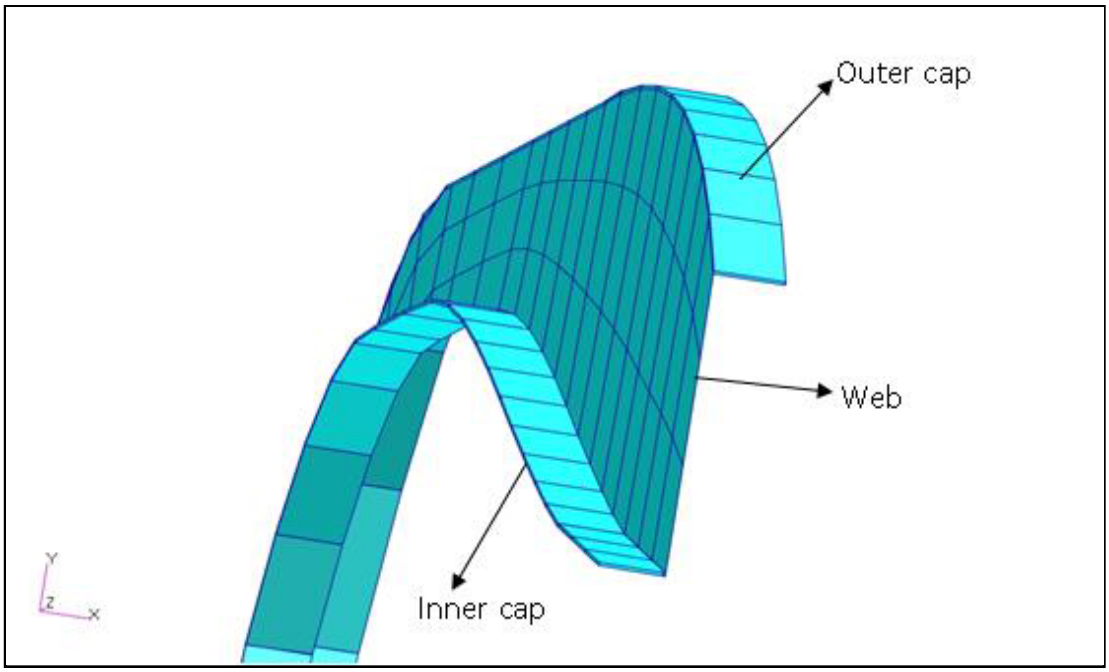

Figure 2.3.5: Detailed FEM of the frame

Bulkheads

Bulkhead is the main supporting member of the cockpit. It supports longerons, skins, floors and decks. Bulkhead also resists the compression loads which results from internal pressure. It consists of caps, web, and horizontal and vertical stiffeners. Caps are connected to the all side of the web. Side caps distribute the side shear loads from the skin. Lower caps support the floors and the skin, and upper caps carry a portion of the internal pressure loads of the cockpit. In the model, also seating rails are supported from the bulkheads which are located behind the pilots. In the real structure, bulkhead webs have cut-outs especially for the harness installations. However in the model, web cut-outs are not modelled for the simplification reasons. Stiffeners, caps and seating rails are modelled with CBEAM elements. CQUAD4 and CTRIA3 elements are used for the webs. CTRIA3 elements are generated only at mesh transition regions where especially at the connection points between parts. The detailed FEM of the bulkheads is shown in Figure 2.3.6 and Figure 2.3.7 respectively.

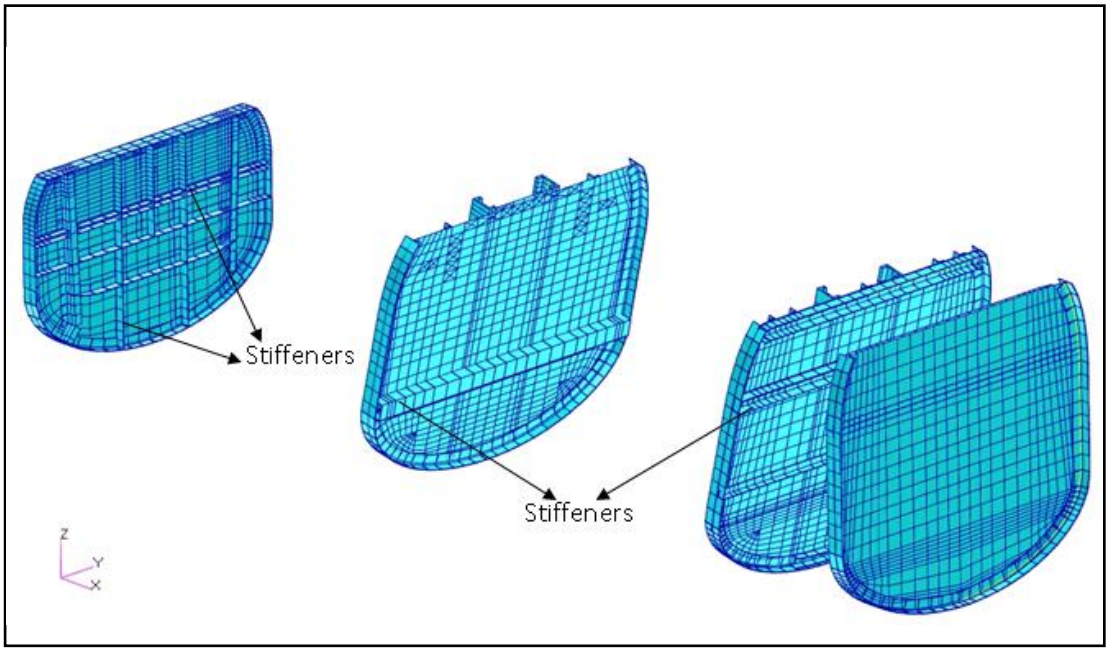

Figure 2.3.6: General view of bulkhead FEM

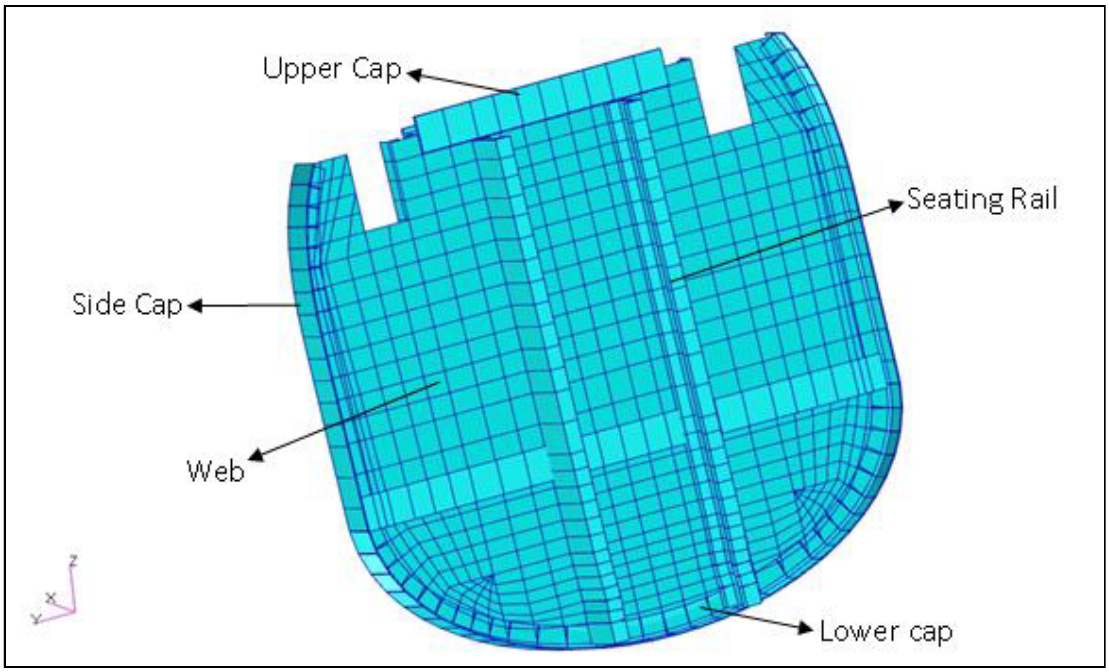

Figure 2.3.7: Detailed FEM of the bulkheads

Skin

The skin carries fuselage shear flows and transfers the differential air pressures to the frames and bulkheads. It is supported by longerons, bulkheads and frames. In the model, skin lies between the upper and the lower longerons. Because of its sheet form, skin is modelled mainly with CQUAD4 elements. Cut-outs are not modelled for the simplification reasons. At some transition regions, CTRIA3 elements are used during the meshing. The detailed FEM of the skin is shown in Figure 2.3.8.

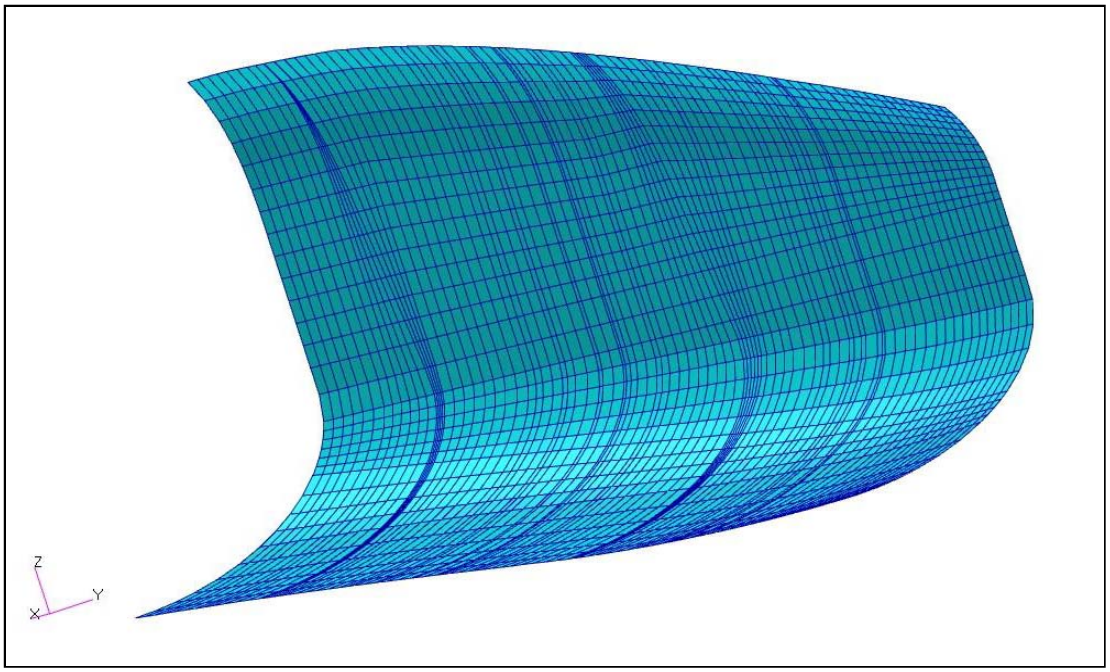

Figure 2.3.8: Detailed FEM of the skin

Front & Rear Floor

The front floor is placed between the lower longerons and supported also by the bottom frames. The rear floor is located between side frames and supported also by floor posts which are the stiff vertical beams under the floor. Floors are loaded mainly with cockpit pressure and consist of floor web with its reinforcement members, longitudinal and transverse beams. Beams of the floor are modelled with CBEAM elements while webs are modelled with CQUAD4 elements. The detailed FEM of the front and a rear floor is shown in Figure 2.3.9.

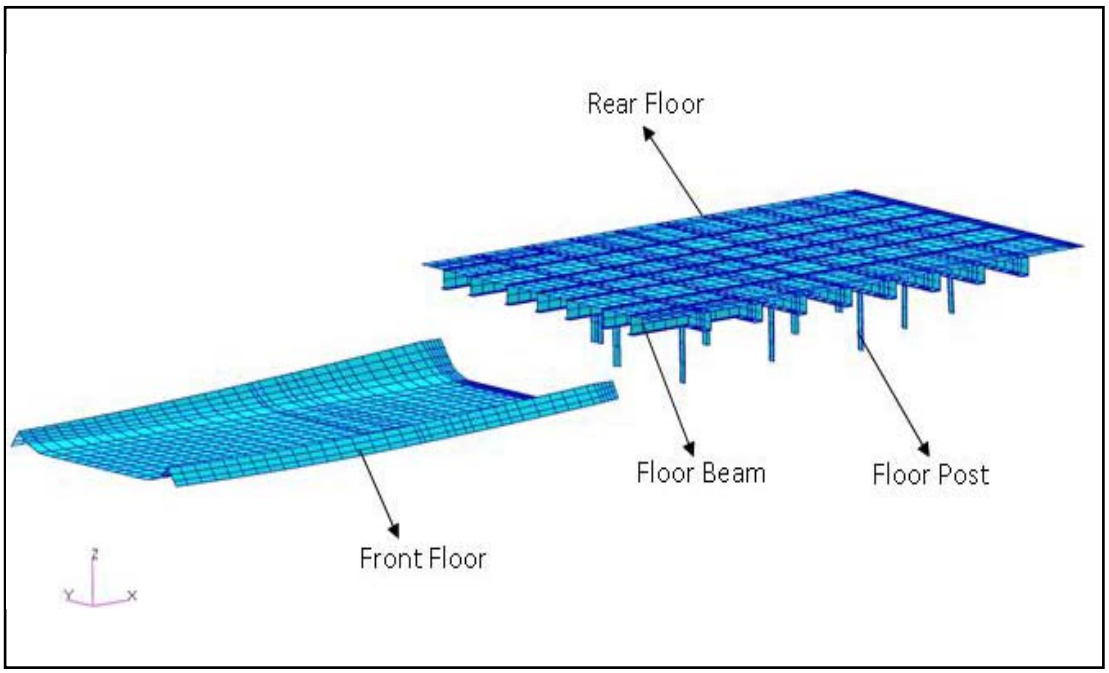

Figure 2.3.9: Detailed FEM of the front and rear floors

Upper & Lower Deck

The upper deck lies between the upper longerons whereas the lower deck is placed between the cockpit panels. Deck structure supports the seat rail at the rear cockpit. It also provides a mounting platform for the equipments. Deck consists of web with longitudinal and transverse stiffeners. Stiffeners are modelled by CBEAM elements and CQUAD4 elements are used in the modelling of the webs. The detailed FEM of the front and a rear floor is shown in Figure 2.3.10.

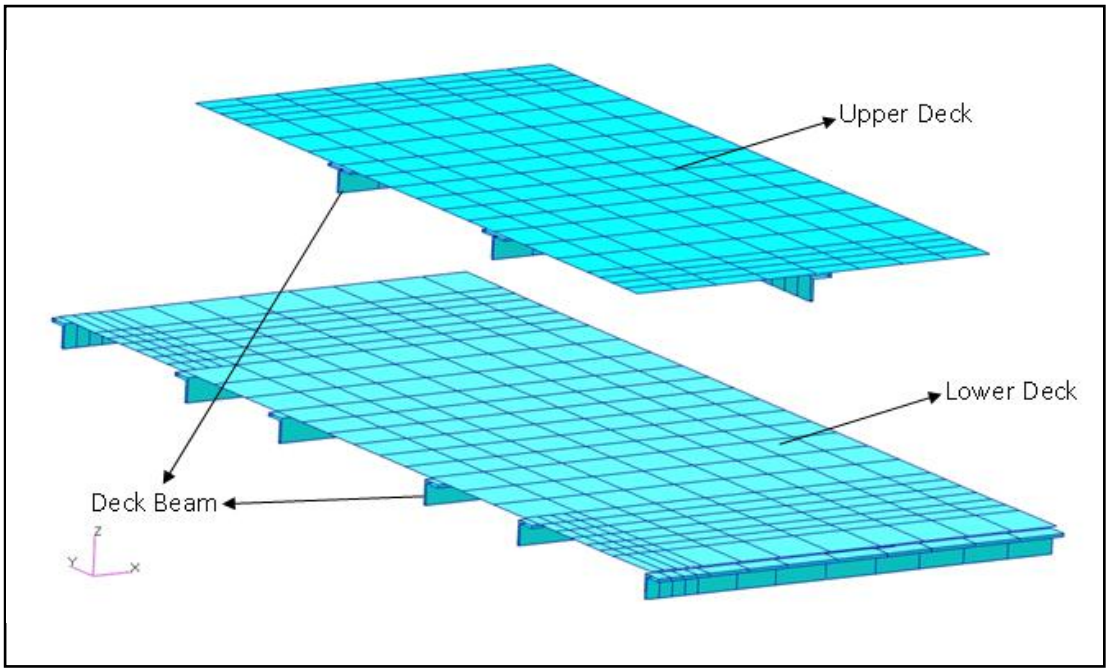

Figure 2.3.10: Detailed FEM of the upper and lower deck

Windshield

Windshield is modelled with CTETRA (3-D) solid elements. During the modelling, the volumetric parameters are considered in order to reflect the stiffness of the structure better. Windshield connection to the upper longerons is performed with the fasteners, piano type hinges and the fittings. Instead of modelling these attachment members, RBE2 elements are used at the connection points. While creating RBE2 elements, all of 3 translational and 3 rotational degrees of freedoms (DOF) are fixed. So, at the connection points, force and moments are directly transmitted between the windshield and the longerons. The detailed FEM of the windshield is shown in Figure 2.3.11.

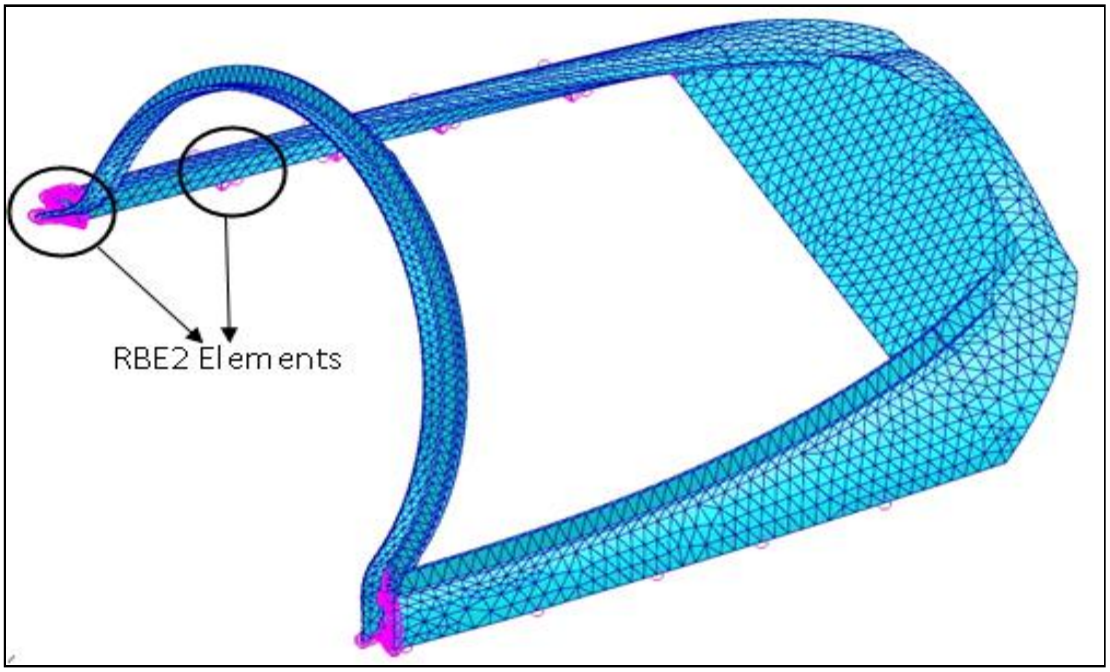

Figure 2.3.11: Detailed FEM of the windshield

Horse Shoe

Horse Shoe is modelled in order to add lateral stiffness to the cockpit, especially places where it connects to the upper longeron. As in the case of the windshield, it is modelled with CTETRA elements and attachment of horse shoe to the longeron is performed with RBE2 elements. RBE2 elements are used such that 6-DOF is constrained. In other words connections are in rigid-fixed forms. The detailed FEM of the horse shoe is shown in Figure 2.3.12.

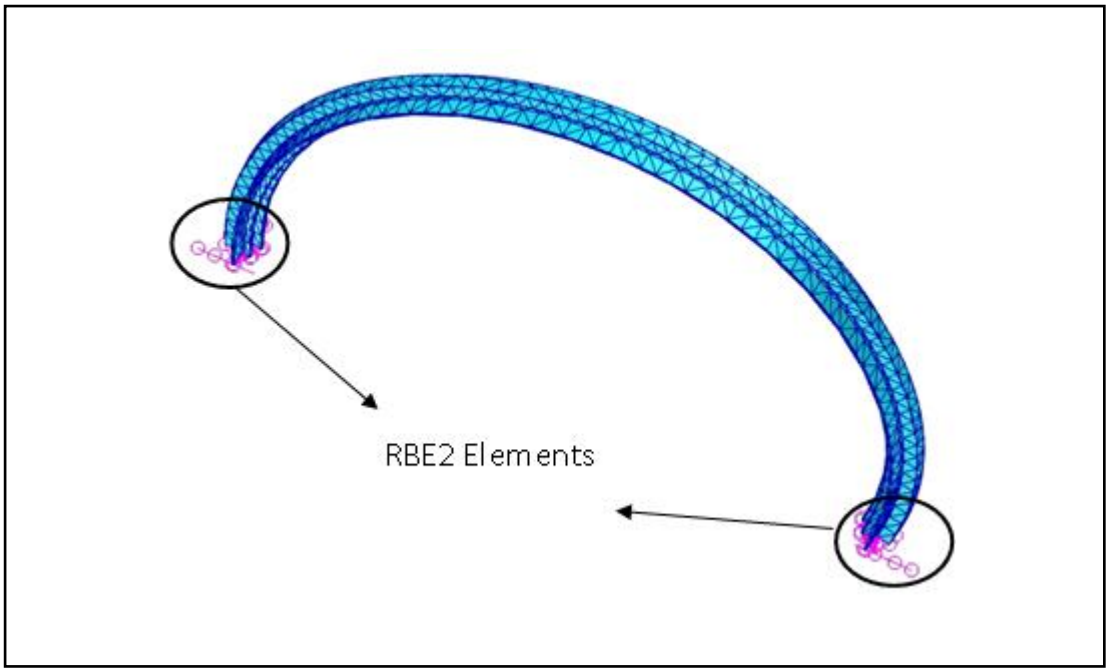

Figure 2.3.12: Detailed FEM of the horse shoe

Sheet support

The sheet support which mainly supports the secondary structures in the cockpit is modelled for adding the lateral stiffness to the model. Although there are cut outs on the structure, they are not modelled. Sheet support is modelled with CQUAD4 and CTRIA3 elements. RBE2 elements are used to connect the support to the upper longerons. Three translational DOF is assigned at the connection points. The detailed FEM of the sheet support is shown in Figure 2.3.13.

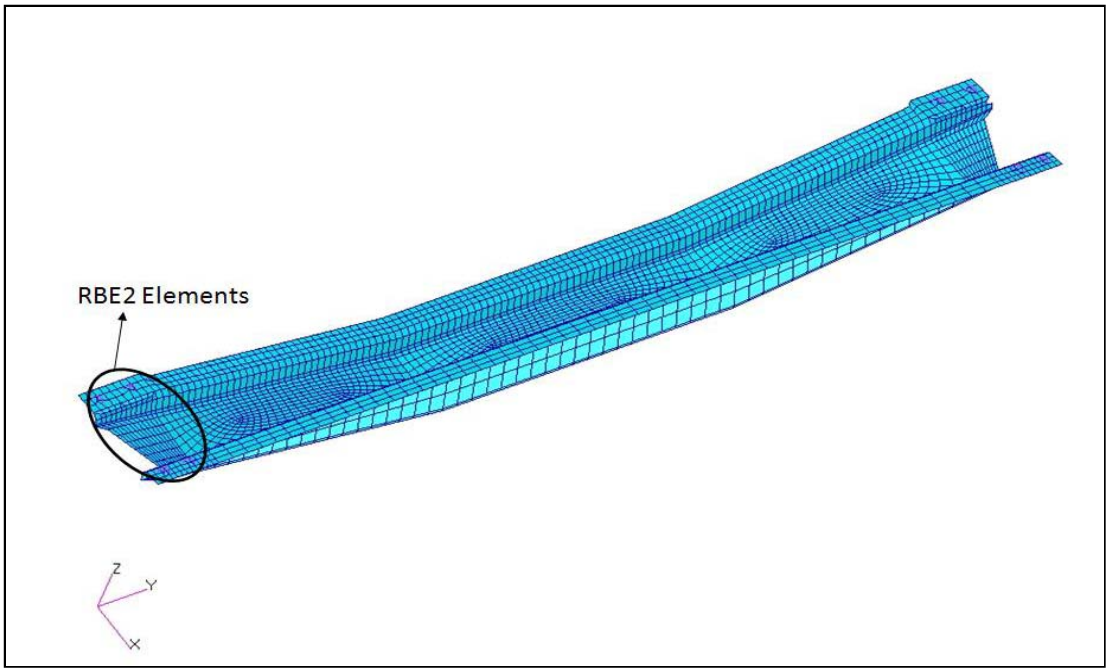

Figure 2.3.13: Detailed FEM of the sheet support

Tie-Bars

There are two tie bars in the model which are located at front and rear cockpit. These bars are connected to the frames and support the upper longerons against the lateral loads caused by the cabin pressure. The sides of the tie bar are in plate form and these side sections provide connection area on the frames. Main bar section is modelled with CBEAM elements. Although the side sections are in plate form, due to the simplification reasons, CBEAM elements are also used for these sections. Also the connections of the tie-bars to the frames are not modelled with rigid elements as in the case of the connection of the primary structures between each other. The detailed FEM of the tie bars are shown in Figure 2.3.14 and Figure 2.3.15 respectively.

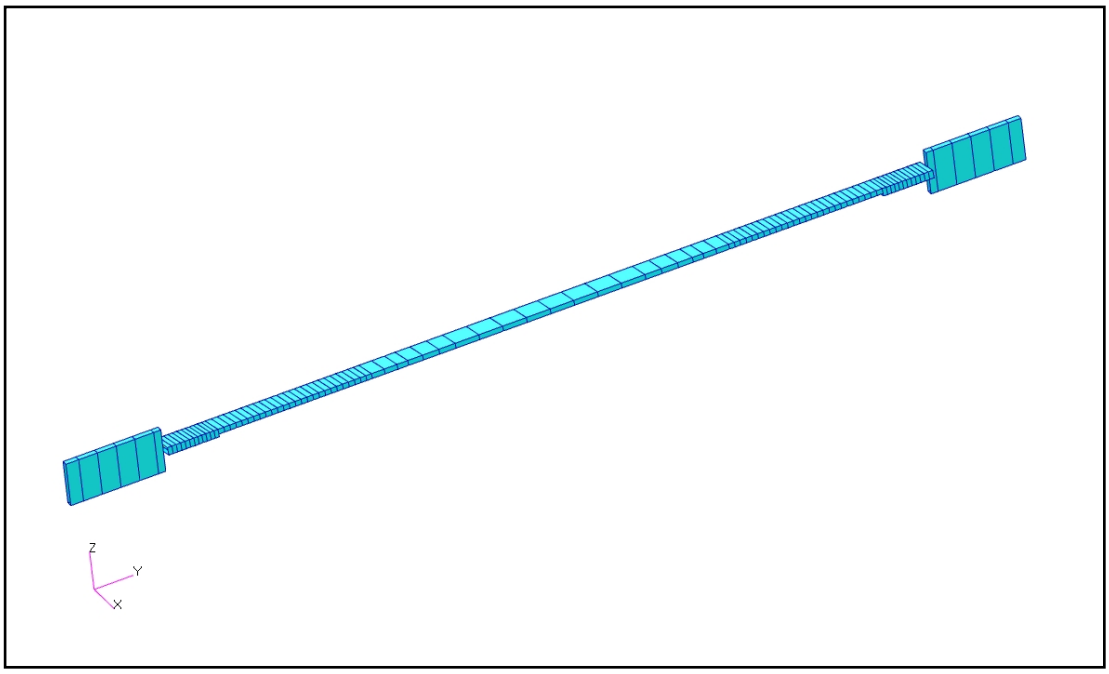

Figure 2.3.14: Detailed FEM of the front tie bar

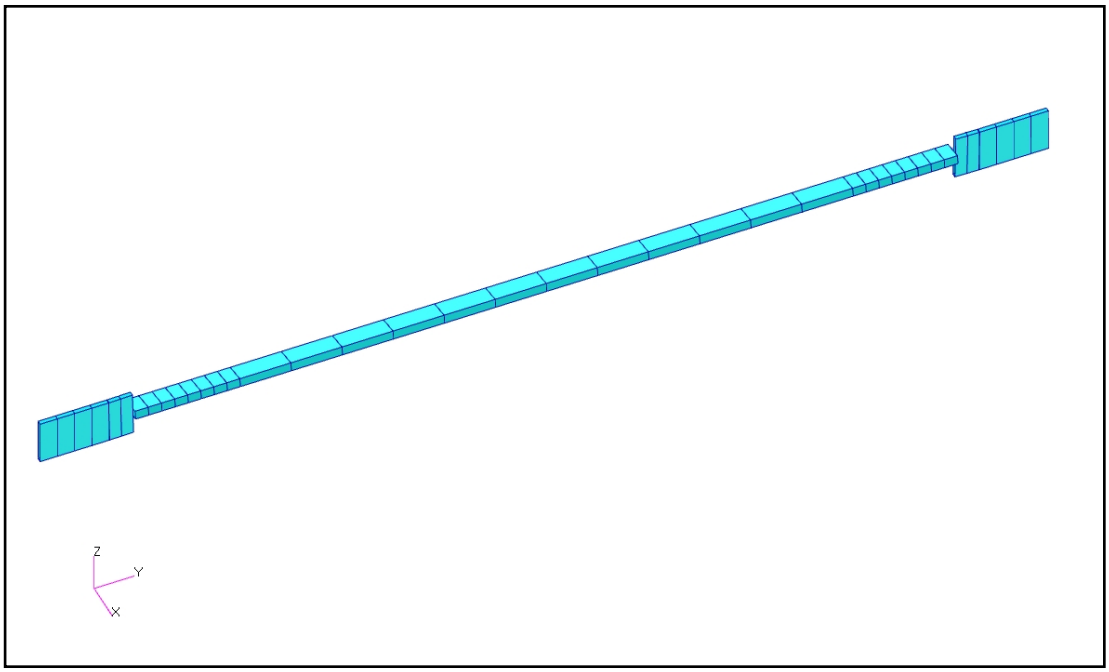

Figure 2.3.15: Detailed FEM of the rear tie bar

Assembly of the structures

The assembly of the parts is shown in Figure 2.3.16. For better visualization, half of the cockpit is shown. The other part is the symmetric of this part in X-Z plane. At the intersection locations, mesh density on the parts is arranged in such a way that the connectivity requirement of the global model is satisfied.

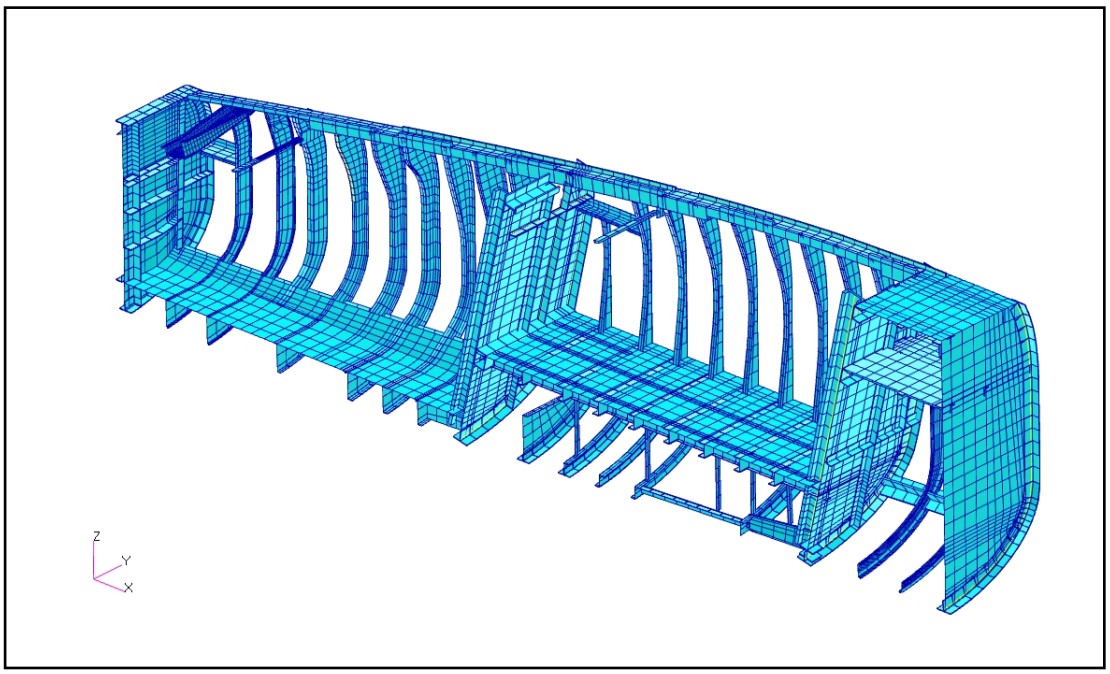

Figure 2.3.16: Assembly of the structures

Material Properties

In this study, structures are built up with isotropic materials. In the model, aluminium, steel and magnesium alloys are used to assign the mechanical properties of the structures. Mechanical properties of the materials according to their structural forms are given in Table 2.3.2. In Table 2.3.2, E, Ftu, Fty, Fsu, ρ and ν stand for elastic modulus, ultimate tensile strength, yield tensile strength, ultimate shear strength, density and Poisson's ratio.

Table 2.3.2: Mechanical properties of the materials

Part Name	Material	Form	E (ksi)	Ftu (ksi)	Fty (ksi)	Fsu (ksi)	ρ (lb/in^3)	ν
Frame, Skin, Floor, Deck, Bulkhead, Intercostals, Sheet Support	Al 7075 T6	Sheet	10300	78	70	47	0.101	0.33
Longeron, Stiffeners, Bulkhead caps, Seat Rail	Al 7075 T6	Extrusion	10400	78	70	41	0.101	0.33
Tie Bar	Al 2024 T351	Plate	10700	64	48	38	0.100	0.33
Horse Shoe	Al 356 T6	Aluminium Casting	10300	22	15	14	0.097	0.33
Windshield	AZ91C T6	Magnesium Casting	6500	17	12	-	0.065	0.35

Thickness Properties

In the model, web thickness is defined as a constant over the CQUAD4 and CTRIA3 elements. By assigning the thickness to these 2-D elements, real 3-D web form is obtained. The web thicknesses used in the model is given in Table 2.3.3.

Table 2.3.3: Web thicknesses used in the model

Webs	Thickness (inches)
Frame (Side)	0.050
Frame (Bottom)	0.040
Bulkhead	0.040
Skin	0.050
Front/Rear Floor	0.040
Upper/Lower Deck	0.063
Intercostal	0.050
Sheet Support	0.050

2.4 Checks for Finite Element Model

Before running the finite element analysis (FEA), in order to have clear load path, performance of the elements should be in desirable levels as the shape of the elements significantly affects the stress values calculated in FEA. In order to understand whether the model has mechanism or not, in other words, whether it has rigid body motion in it or not, also rigid body check should be done prior to the static analysis.

Element Quality Check

Due to the difficulties in structural geometries, inevitably, during the meshing process, some of the elements exceed the default element geometric limits of the NASTRAN®. These elements are generally located in transition areas. Although these elements exceed the limits, it does not prevent the solution of the other elements and NASTRAN® can reach a solution. However, in order to get clear load path for the future applications of the study, such as comparison of the test results with the FE analysis results, the element quality check become crucial especially for the testing points. As a result of these checks, mesh refinement is done for the regions where clear load path is necessary.

For quadrangle elements, aspect ratio, skew, taper and warping is the geometrical parameters which are to be verified with respect to NASTRAN® limits. For triangle elements only two of them which are namely aspect ratio and skew are considered. The descriptions of the element quality check parameters for the quadrangle elements are shown in Figure 2.4.1.

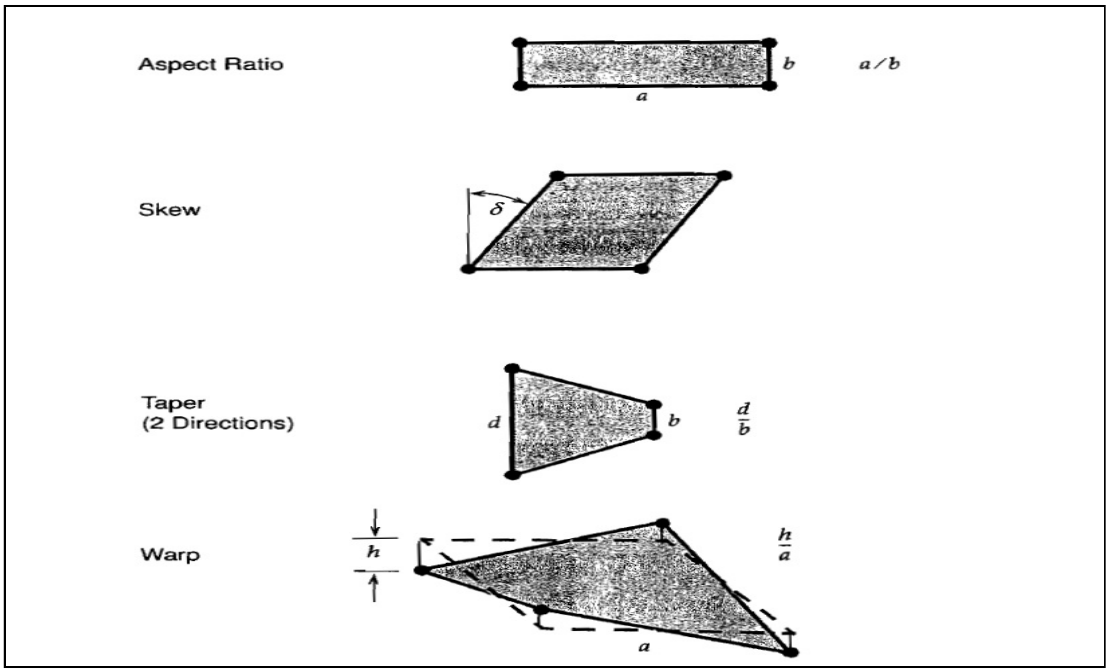

Figure 2.4.1: Quadrangle element quality check parameters [16]

The aspect ratio parameter is the width over the length ratio. Skew is an angle used to verify that the CQUAD4 elements are not too trapezoidal and the CTRIA3 elements not too slender. Taper is a surface area ratio which reflects whether CQUAD4 elements are tapered or not. Warping is defined as the angle which shows the deviation of the element from being planar. The element quality check parameters with their NASTRAN® limits are given in Table 2.4.1.

Table 2.4.1: Element Quality criteria

Quality Parameters	**NASTRAN® Limits**
Aspect Ratio	5
Max. Warping Factor	0.05
Max. Taper Ratio	0.5
Min. Quad Skew	30 deg
Max. Quad Angle	30 deg
Min. Quad Angle	150 deg
Max. Tri Angle	160 deg
Min. Tri Skew	10 deg

Rigid Body Check

In static analysis, in order to reach a solution, there should not be any mechanism or rigid body motion in the FEM. The complete structure can have at most six rigid body modes which are in three translational and three rotational directions. These six rigid body mode frequencies should be zero for the check purposes. Rigid body modes are calculated in NASTRAN® (SOL103) solution sequence. Normal modes analyses are done by assigning free/free boundary condition to the model. For medium and large scale models, the most effective eigenvalue extraction method which is Lanchoz Method [24] is used during the control. The mass distribution is obtained by assigning the density parameters to the materials involved in the model. Natural modes analysis results for the first six modes are given in Table 2.4.2.

Table 2.4.2: Natural modes analysis results

Rigid body motion (Directions)	**Mode**	**Frequency [Hz]**
Tx	1	0.000005
Ty	2	0.000009
Tz	3	0.000010
Rx	4	0.145680
Ry	5	0.252420
Rz	6	0.431200

Here, Tx, Ty, Tz and Rx, Ry, Rz represents for translational and rotational motions in x, y and z directions respectively.

Rigid body mode shapes for first six modes are shown from Figure 2.4.3 to Figure 2.4.5 respectively.

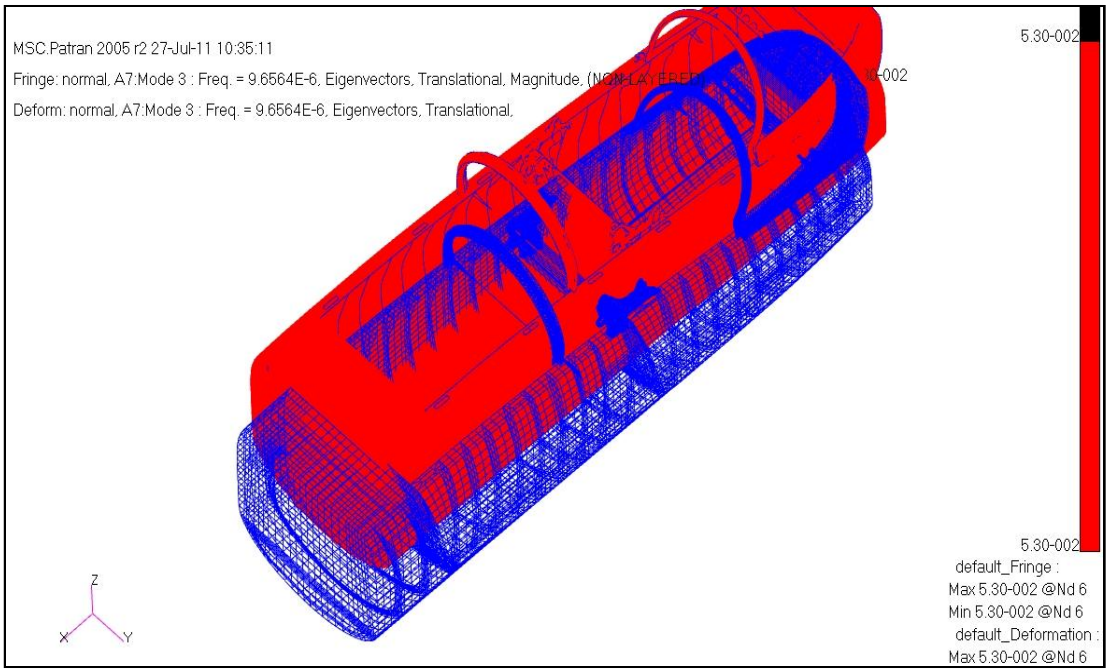

Figure 2.4.2: Mode shape-Tx

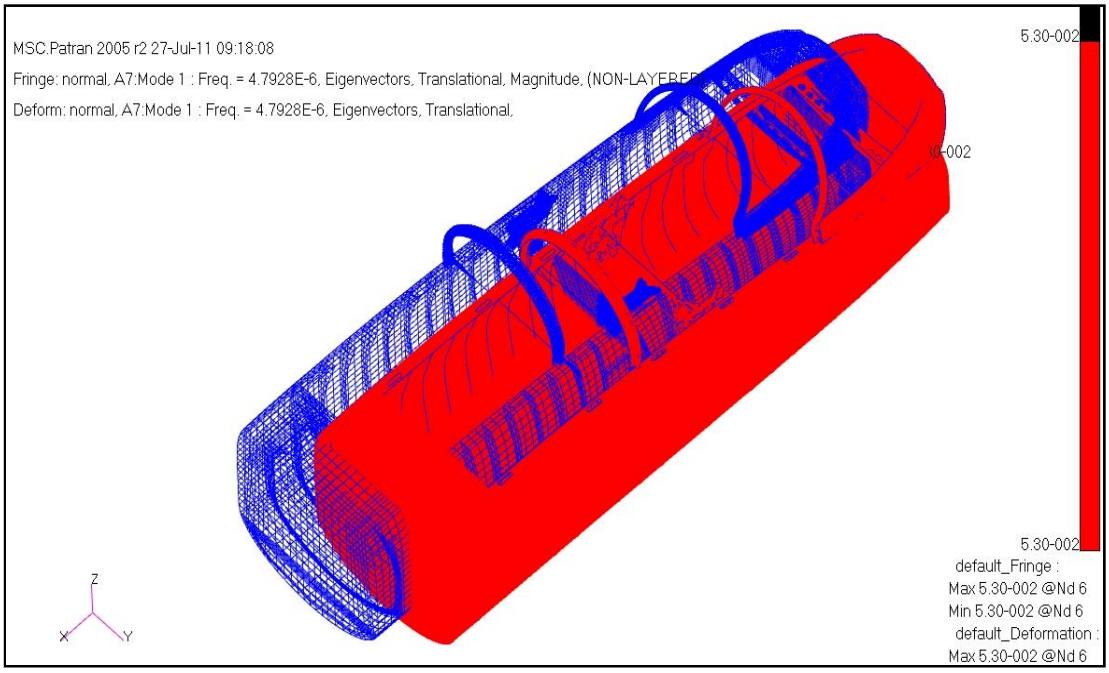

Figure 2.4.3: Mode shape-Ty

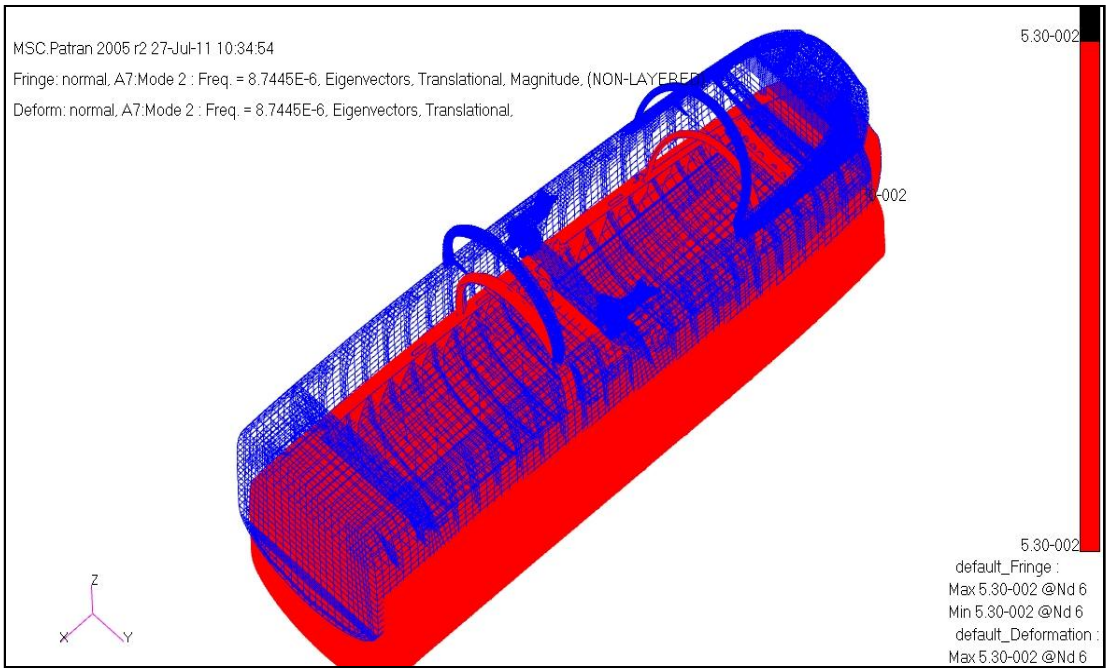

Figure 2.4.4: Mode shape-Tz

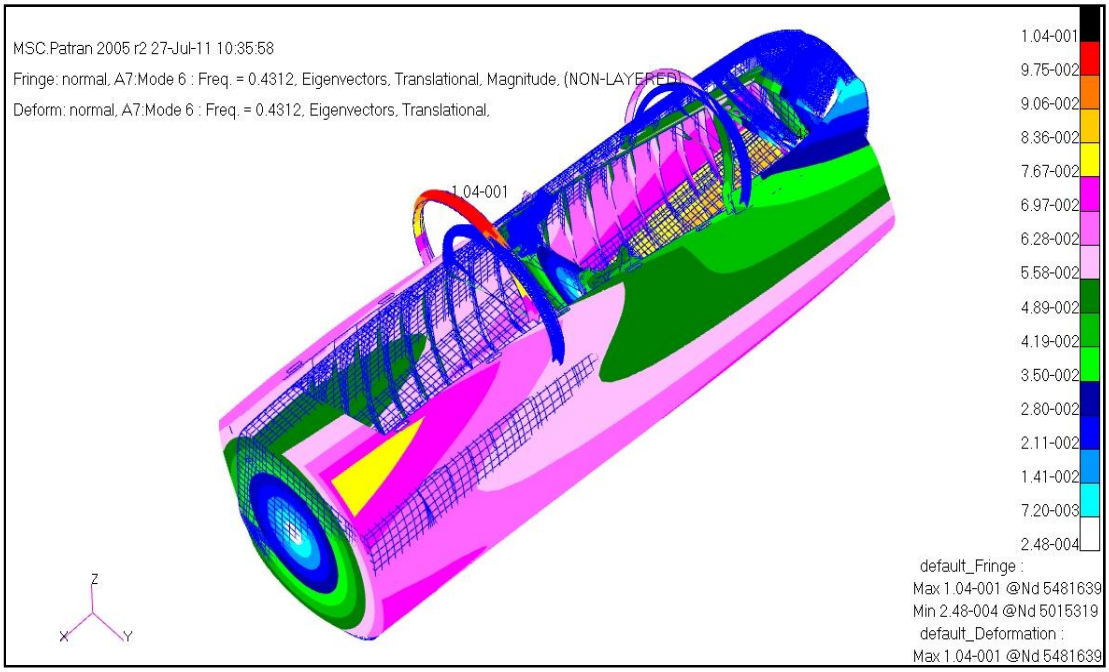

Figure 2.4.5: Mode shape-Rx

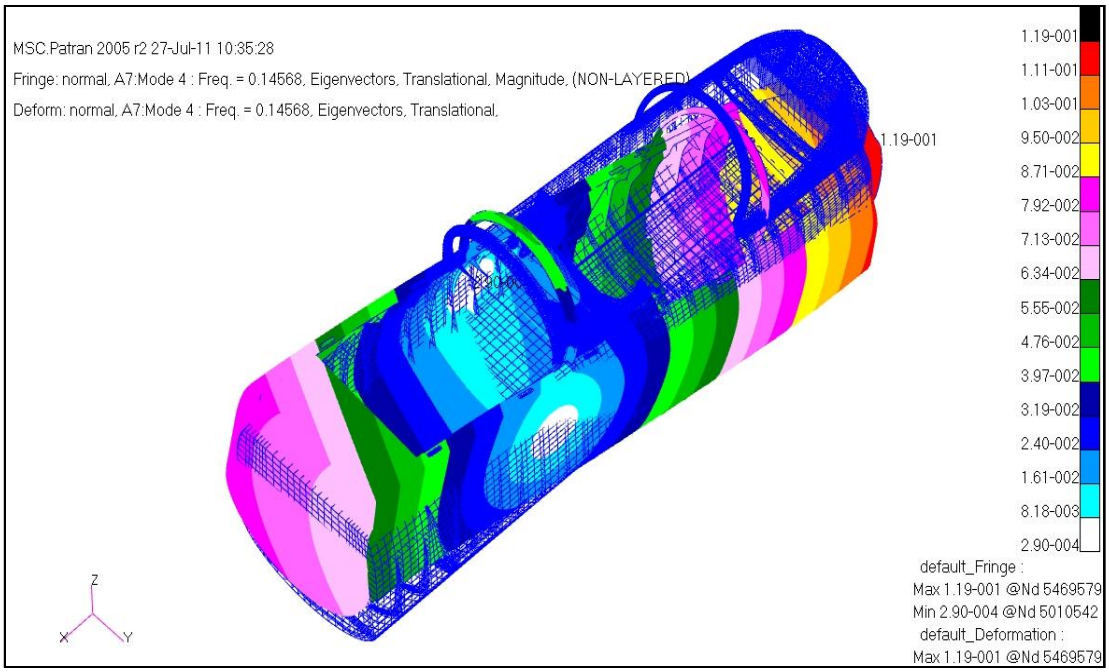

Figure 2.4.6: Mode shape-Ry

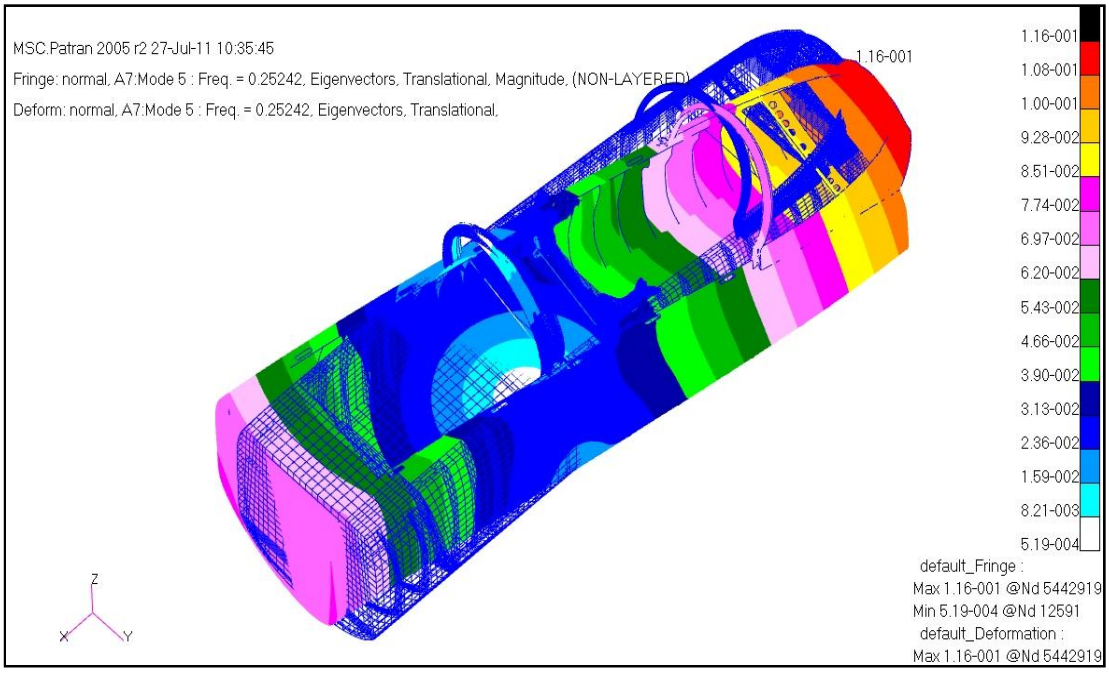

Figure 2.4.7: Mode shape-Rz

2.5 Finite Element Analysis

In this study, NASTRAN® (SOL101) solution sequence is used for the linear static analysis. A set of linear equations generated by the finite elements represents the differential equations and the solution of these equations depends on the load and displacement boundary conditions. Assumptions of the analysis are the following: displacements are small, stiffness matrix and boundary conditions do not change and displacements are directly proportional to the loads. Also, the material used in the study is homogenous and isotropic.

Applied Loads

In the study, cockpit is loaded with 5 [Psi] internal pressure loads, which is the limit load for the cockpit pressurisation system. Load is applied to the surfaces which are exposed to the internal pressure in the cockpit. At the front side; bulkhead-1, at the rear side; bulkhead-3 and upper deck, at the bottom side; front and rear floors, and at the right and the left side skin create the pressure surfaces of the cockpit. At the upper side, between bulkhead-1 and upper deck, there are canopies and windshield to complete the close shape of the cockpit. However, these structures are not taken into account as pressure surfaces for the reasons mentioned in section 1.4. Under 5 [Psi] cabin pressure, the loads exerted by the canopy on the longerons through the canopy hooks are gathered from the manufacturer company. On the other hand, the loads on the longerons exerted by the windshield pressure loads are neglected as mentioned in section 1.4. The shell elements which are located on the pressure surfaces are oriented in such a way that their normal axes are facing to the outdoors. Thus, loss of the pressure load is prevented by assigning the pressure force directions as the same. The pressure surfaces in the model and the shell element normals are shown in Figure 2.5.1 and Figure 2.5.2 respectively. Canopy hook loads for the left side of the cockpit are given in Table 2.5.1. Here, Py, Pz and Mx stand for force in lateral, force

in vertical and moment about forward direction respectively. Also loads are shown schematically in Figure 2.5.3.

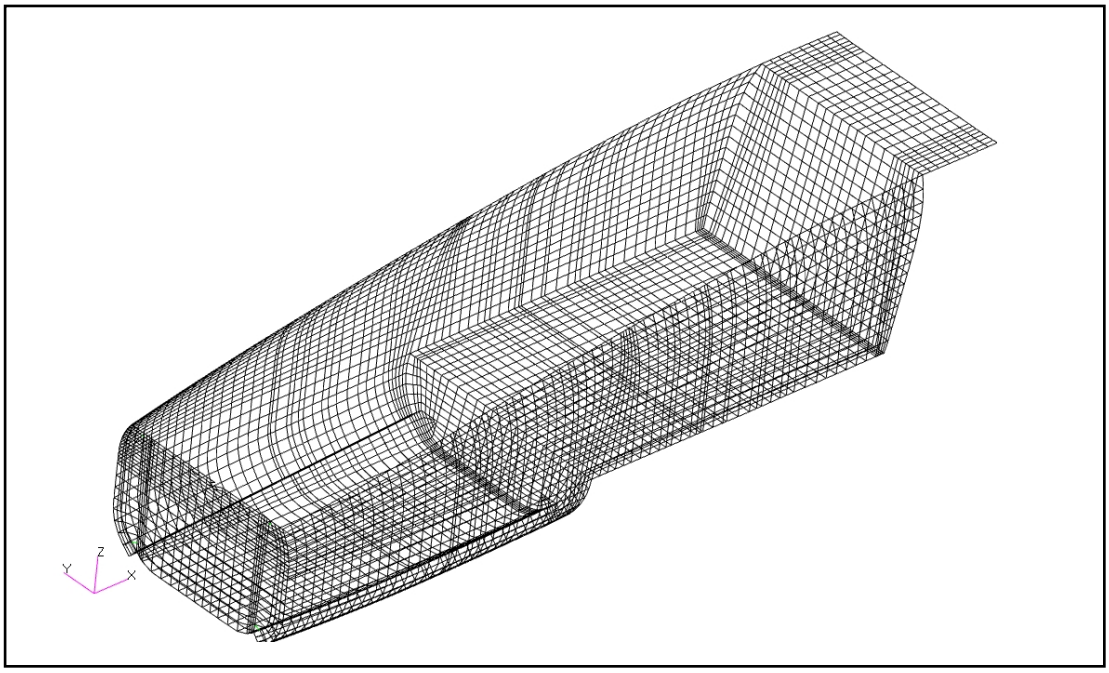

Figure 2.5.1: Pressure surfaces in the model

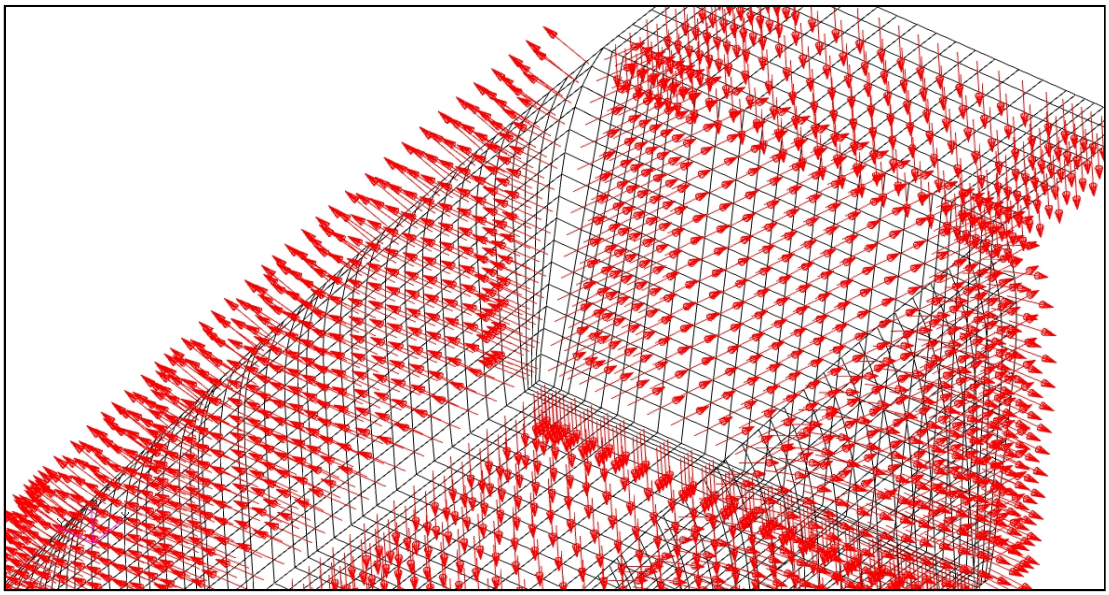

Figure 2.5.2: Shell element normals

Table 2.5.1: Canopy Hook Loads-Left Side

Location	Py (lb)	Pz (lb)	Mx (lb.in)
F6	635	1530	2140
F9	710	1650	1688
F12	433	1170	287
F15	550	1900	0
F19	235	2460	-559

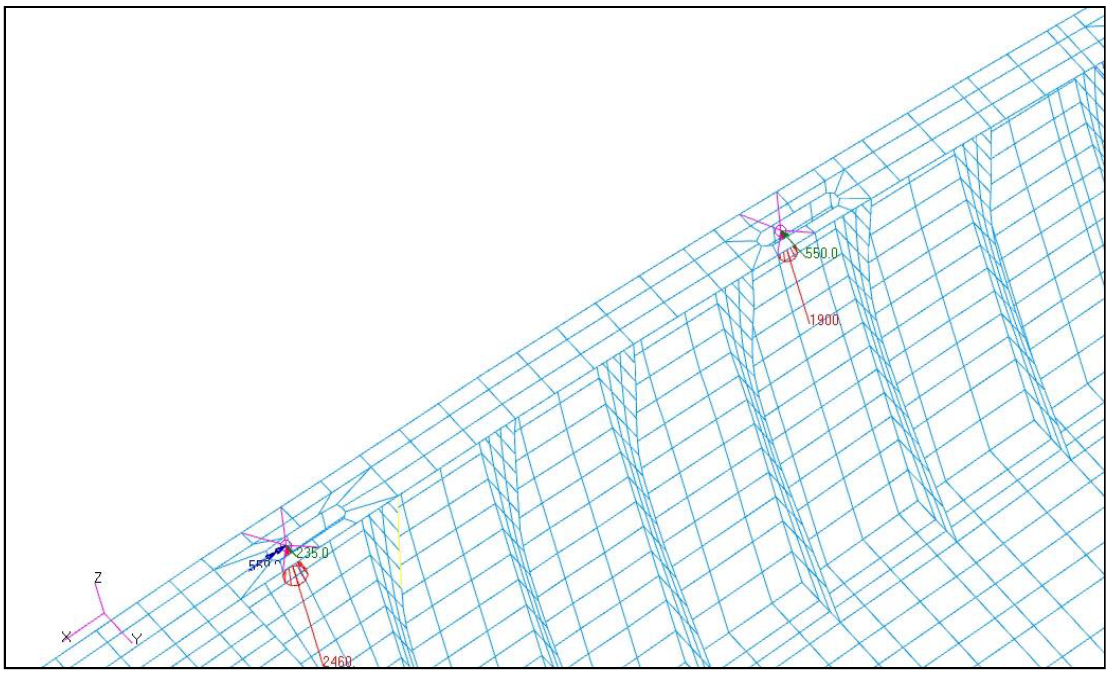

Figure 2.5.3: Schematic representation of canopy hook loads

Displacement Boundary Conditions

Under the static pressure load, for the solution of the FEM, model is only fixed at its bulkhead-4 (B4) as a simply supported way. On the real fuselage structure, actually, there is a nose section which is located at the front side of the cockpit. The nose section is cantilevered at bulkhead-1 (B1). At the ground condition, nose section does not support the cockpit effectively. Therefore, at B1, model is released as free. At the rear side, behind the cockpit, there is a rear fuselage which supports wing,

engine and empennage. The rear fuselage also supports the cockpit, especially when cockpit is loaded under cabin pressure. In the model, the displacement boundary conditions for the cockpit are assigned by considering these real life end conditions. The translational DOF's at the ends of the upper and lower longerons are constraint in vertical (Z-axis) and in longitudinal (X-axis) directions. However, the rotational DOF's at the constraint points are released as free in order to reduce the boundary effects at the connection points. The lateral (Y-axis) translations are constraint at the longerons due to this particular reason. On the other hand, in order to create static solution matrices in the mathematical model, translation is constraint in lateral (Y-axis) direction at the lower deck-bulkhead web intersection points (see Figure 2.3.16). These points have no impact on the results evaluated for the correlation study. The final configuration of the displacement boundary conditions assigned to the model is shown in Figure 2.5.4. In this figure, constraint translational DOF's in X, Y and Z directions are shown respectively with numbers 1, 2 and 3.

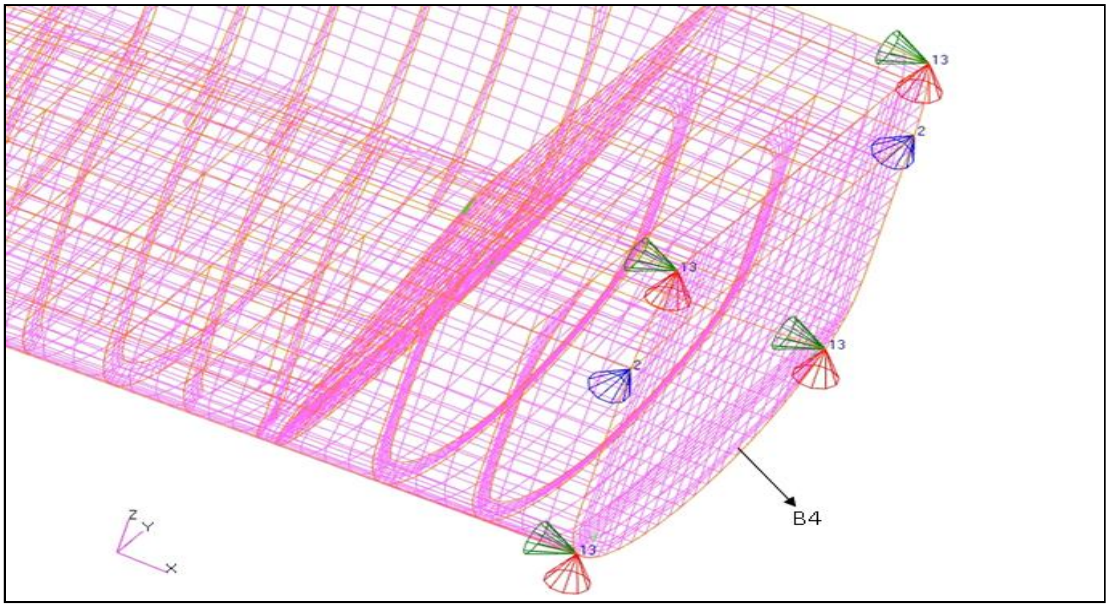

Figure 2.5.4: Displacement boundary conditions

2.6 Summary

In this section, finite element model (FEM) of the cockpit structure is constructed by considering the functions of the structures involved in the model. Assumptions made during the modelling are also described in detail. The model is checked in order to determine whether it is suitable for the static analysis or not. After these checks, cabin pressure load is applied to the model by assigning displacement boundary conditions to the specific locations. The finite element model (FEM) is solved by NASTRAN® (SOL101) solution sequence. The results are not evaluated in this section and they will be made according to the static test procedure which considers the locations where strain data is gathered from.

CHAPTER 3

GROUND PRESSURISATION TEST

3.1 Introduction

In order to have a reliable FEM, model must be validated with experimental testing methods. The types of tests and methods which are selected to perform these tests mainly depend on the type of load applied to the model. In this study, cockpit FEM is validated only under cabin pressure load. Cabin pressurisation is applied to the real cockpit structures in a static manner. In this section, ground pressurisation test procedure and the test results for the real cockpit structure are introduced. First, test configuration is described. Secondly, type, criteria for the selection, instrumentation and location of the sensors used in the test are explained. And after having mentioned about test steps, finally, the obtained test results are also interpreted.

3.2 Test Configuration

The ground pressurisation test is performed on the aircraft itself. The cockpit of the aircraft is pressurised on the ground by pressure supplier unit. Pressure supplier unit provides air to the cockpit through a hose pipe which is mounted on the aircraft cabin pressure system. The obtained signals from the sensors which are installed in the cockpit are recorded by data acquisition system. Collected data in the data

acquisition system is then transferred to the mobile PC. The general configuration of the ground pressurisation test is shown in Figure 3.2.1 schematically.

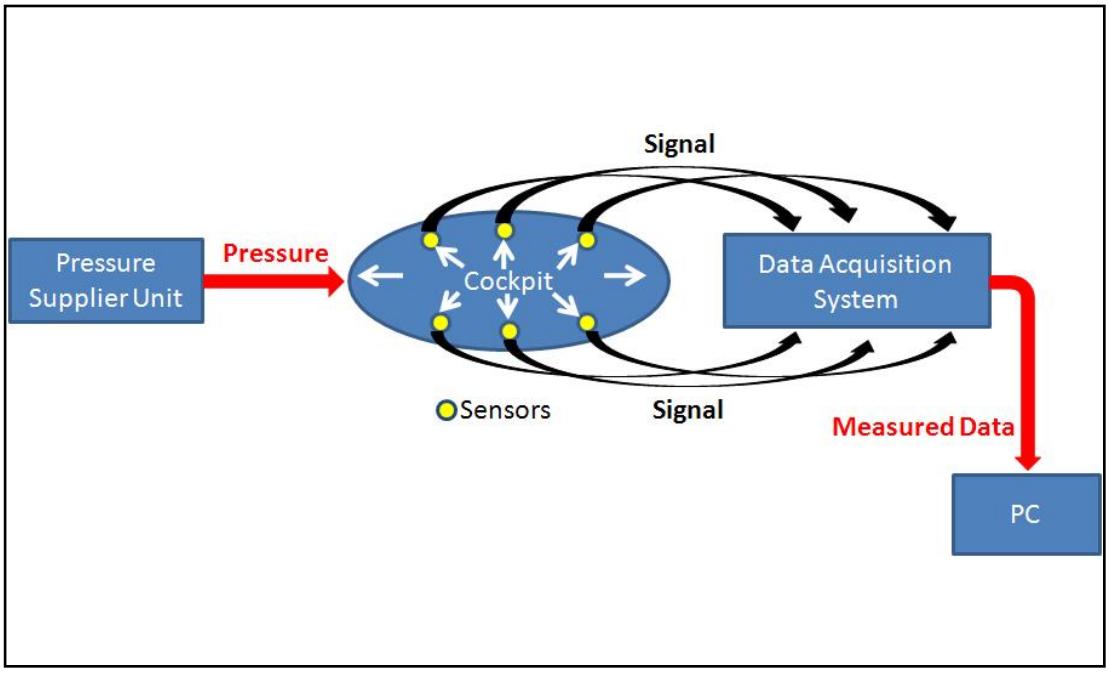

Figure 3.2.1: General Test Configuration

3.3 Sensor Types

Under the cabin pressure, in order to examine the strain changes occurring on the cockpit structures, two types of sensors, namely strain gauges and the pressure transducers, are installed inside the cockpit in order for measuring strain and cabin pressure respectively.

In this study, two types of strain gauges, VISHAY® CEA-13-250UN-350 [29] linear type and VISHAY® CEA-13-125UR-350 [30] rectangular 45^0 single-plane rosette type strain gauges are used. The strain gauge specifications are given in Table 3.3.1.

Table 3.3.1: Strain Gauge Specifications [29], [30]

Gauge Designation	Type	Resistance (Ohms)	Dimensions (inch)	Strain Range (%)	Temperature Range (^{o}C)
CEA-13-250UN-350	Linear	350 ± % 0.3	0.52 × 0.22	±5	-75^{o} to+175
CEA-13-125UR-350	Rosette	350 ± % 0.4	0.42 × 0.62	±5	-75^{o} to+175

While linear type strain gauge has a single data output channel, rosette type strain gauge has three. The strain gauges used in the study are shown in Figure 3.3.1 with their corresponding output channel numbers.

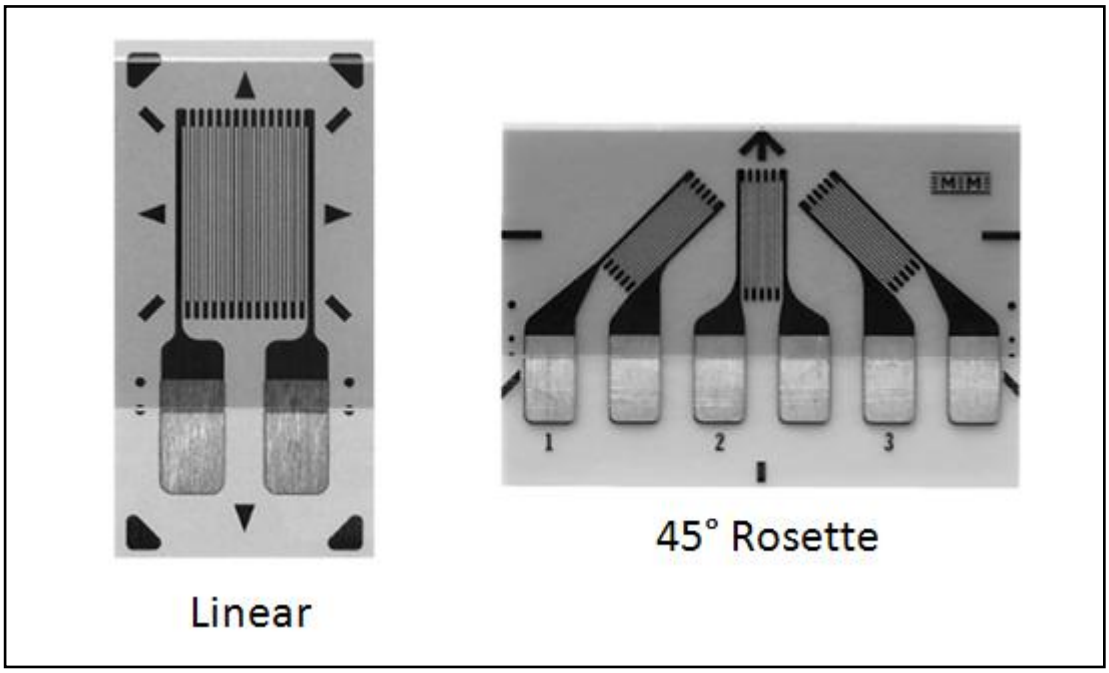

Figure 3.3.1: Linear and Rosette Gauges with their channel numbers [29], [30]

ENDEVCO® Model 8540 [31] Piezoresistive pressure transducer is chosen for its high sensitivity, high stability during temperature transients and having broad measurement ranges from 5 [Psi] to 500 [Psi] pressure. The transducer has a 0.15 [in] face diameter. Pressure transducer used in the study is shown in Figure 3.3.2.

Figure 3.3.2: Pressure transducer used in the study [31]

3.4 Criteria for the Selection of the Sensors

Linear type strain gauges are used in the places where stain changes are mainly varying in one direction. These types of gauges are generally selected on the caps and flanges. If the strain values are expected to change on the structure more than in one direction, rosette type strain gauges are preferred to be installed in those places. Therefore, these types of strain gauges are installed mainly on the webs and panels. In other words, if the structure mainly resists the axial loads and the principal strain directions are known, linear type strain gauges, if the structure mainly resists the shear loads and the principal strain directions are not known, rosette type strain gauges are used. The 45^0 single-plane rosette type gauge has three gauge grids (i.e. arms). Three grids, with the second and the third grids angularly displaced from the first grid by 45^0 and 90^0, respectively. The principal strains are calculated easier in 45^0 single-plane rosette and, in this study, it is selected for its computational advantage. Strain gauges are manufactured from different combinations of grid alloy in order to meet various application requirements. In this study, gauges are selected to be suitable for the aluminium alloy materials they are attached. They are also

offered in a number of different lengths. The sizes of the gauges are selected by considering the installation space limitations.

3.5 Installations of the Sensors

Strain gauge installations are bounded on the aircraft by the limitations of the minimum space required for the installation. The reason is that, structure to be modified is already assembled and the environmental condition for the labour is not the same with the condition during the production phase. For the manufacturer company, it is easier to install the strain gauges on the desired parts before the assembly. Hence, in the study, sensors are installed on the accessible and/or suitable areas found in the cockpit.

Strain Gauge Installation

Linear strain gauges are installed on the upper longeron inner and outer flanges, frame inner caps, bulkhead upper caps, upper longeron web, sheet support and on the tie bars. On these structures, principal strain exists mainly in one direction. Rosette strain gauges are installed on the skin panels. On the skin, principal strain directions are unknown and exist in more than one direction.

Steps in strain gauge installation can be summarised as follows:

- Dirty and greasy surface is cleaned with isopropyl alcohol.
- Marking is done for positioning the strain gauge.
- Paint on the surface is removed with sandpaper.
- Wet sanding is done to the surface by using a proper conditioner.
- Surface is cleaned chemically with neutraliser.
- Surface is dried from centre to the edges.
- Strain gauge is pasted to the surface with the help of bond adhesives.

- Soldering process is carried out to the gauge from its solder tab area.
- Wiring process is completed with marking the cables of the strain gauges.

Rosette arms are named as A, B and C. The arms B and C angularly displaced from the arm A by 45^0 and 90^0, respectively. Arm A is attempted to lie in parallel with aircraft forward direction while arm C is attempted to lie in parallel with vertical axis of the aircraft. Strain gauge installations on some of the cockpit structures are shown from Figure 3.5.1 to Figure 3.5.10.

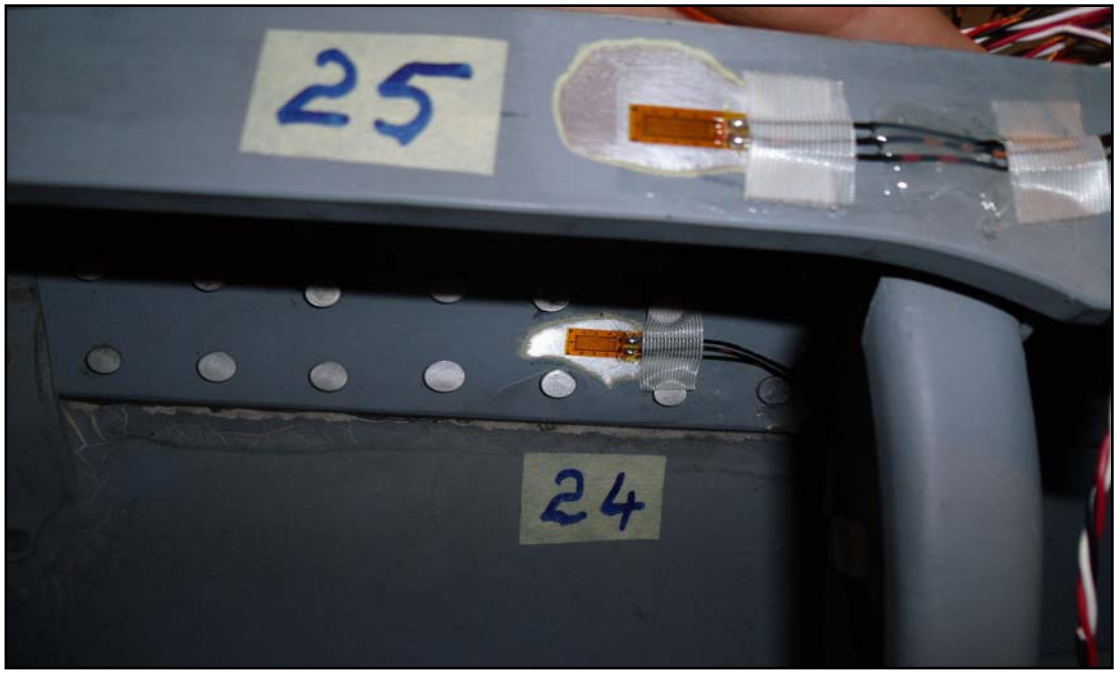

Figure 3.5.1: Linear strain gauges on longeron inner and outer flanges

Figure 3.5.2: Linear strain gauge on longeron inner flange at the near of its cut-out

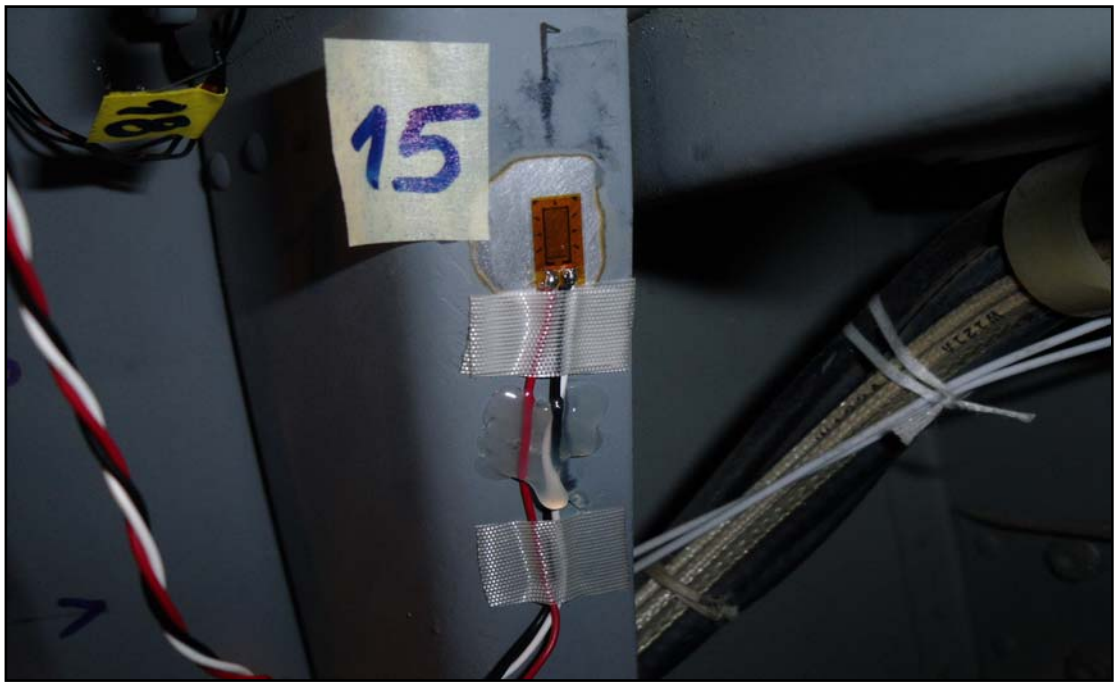

Figure 3.5.3: Linear strain gauge on frame inner cap

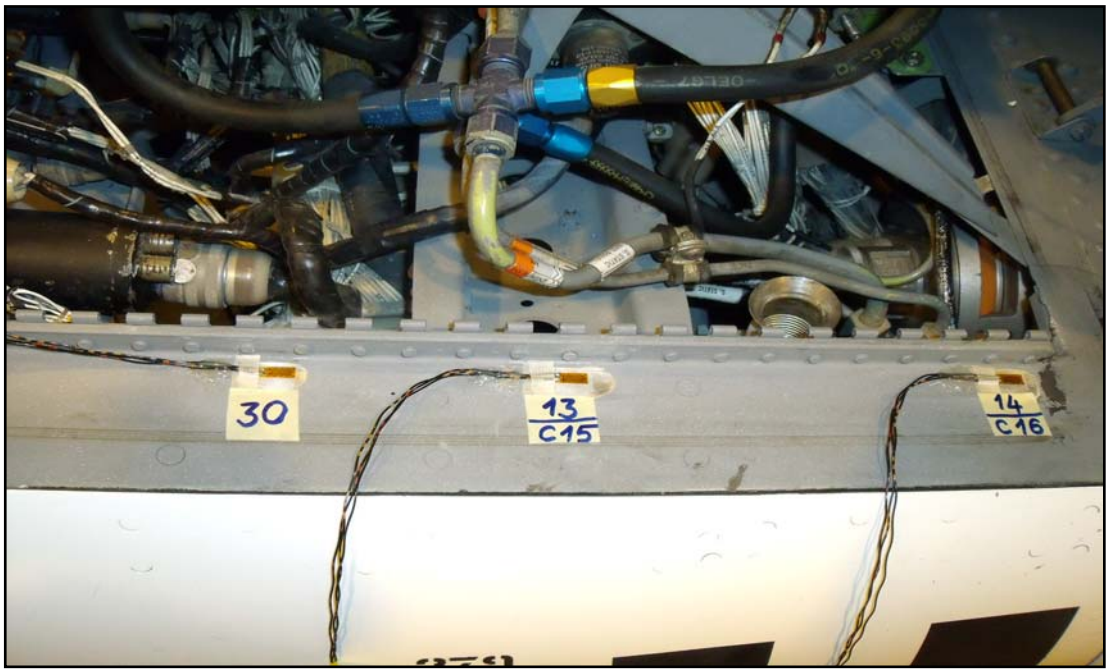

Figure 3.5.4: Linear strain gauges on longeron web

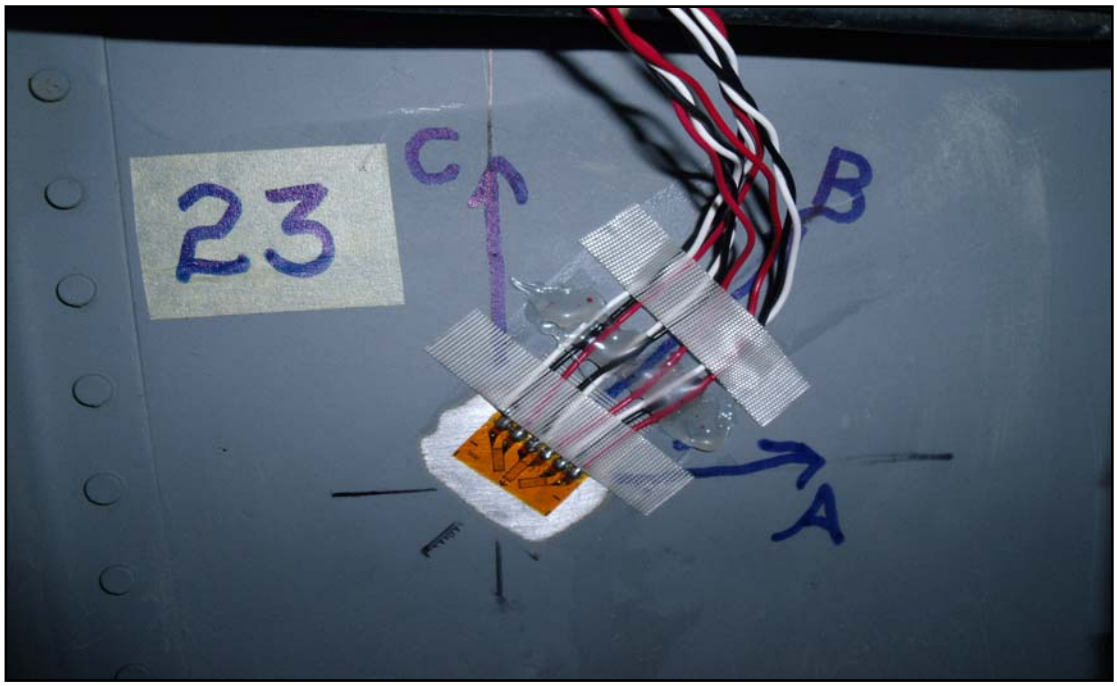

Figure 3.5.5: Rosette strain gauge on skin panel

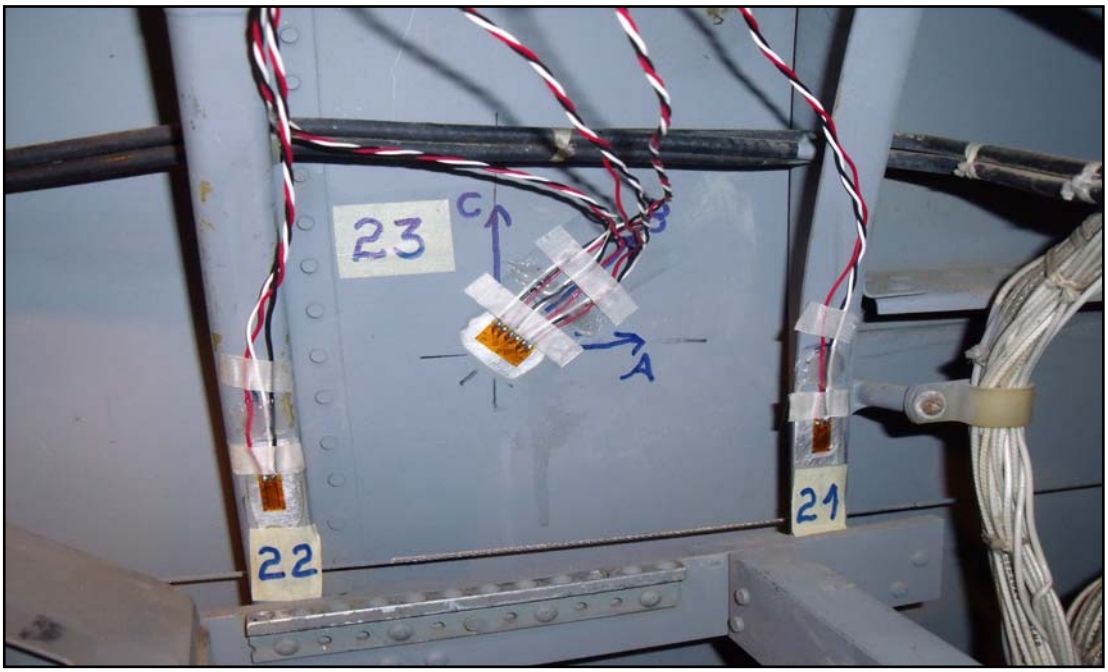

Figure 3.5.6: Strain gauges on frames and skin panel

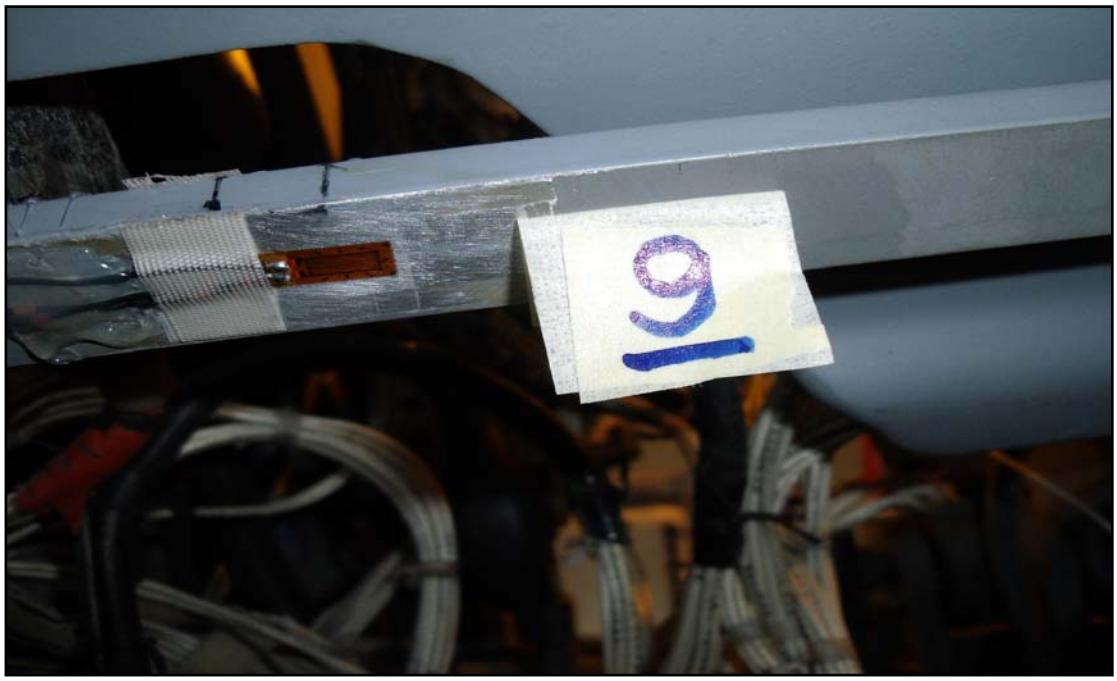

Figure 3.5.7: Linear strain gauge on the tie-bar

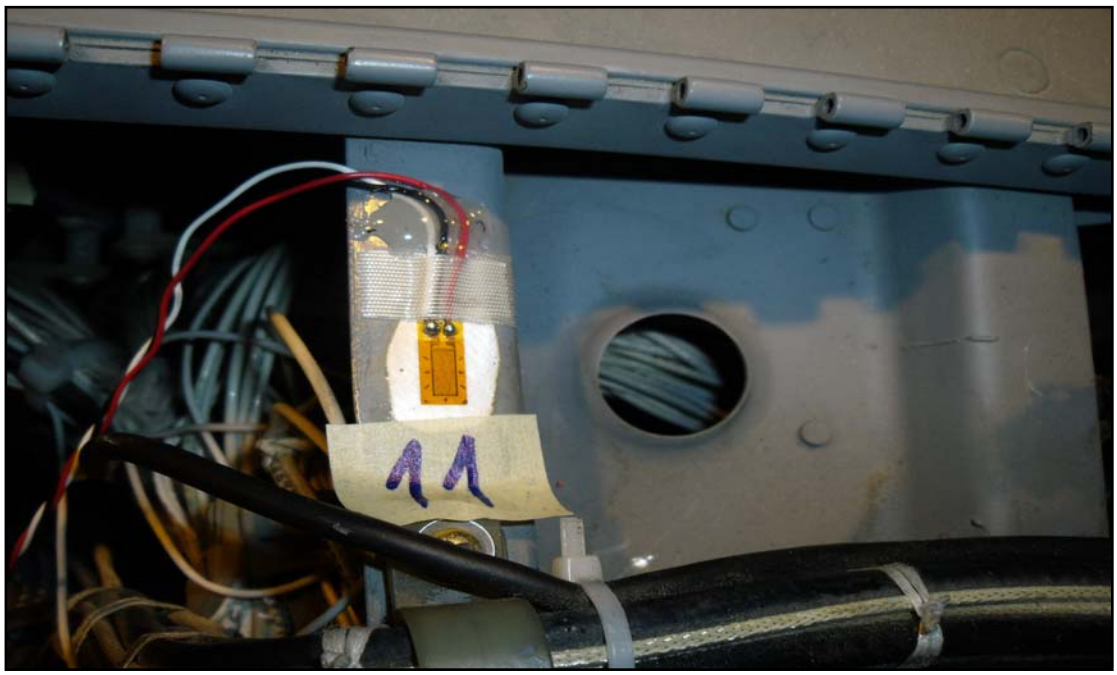

Figure 3.5.8: Linear strain gauge on the sheet support

Figure 3.5.9: Linear strain gauge on the bulkhead upper cap

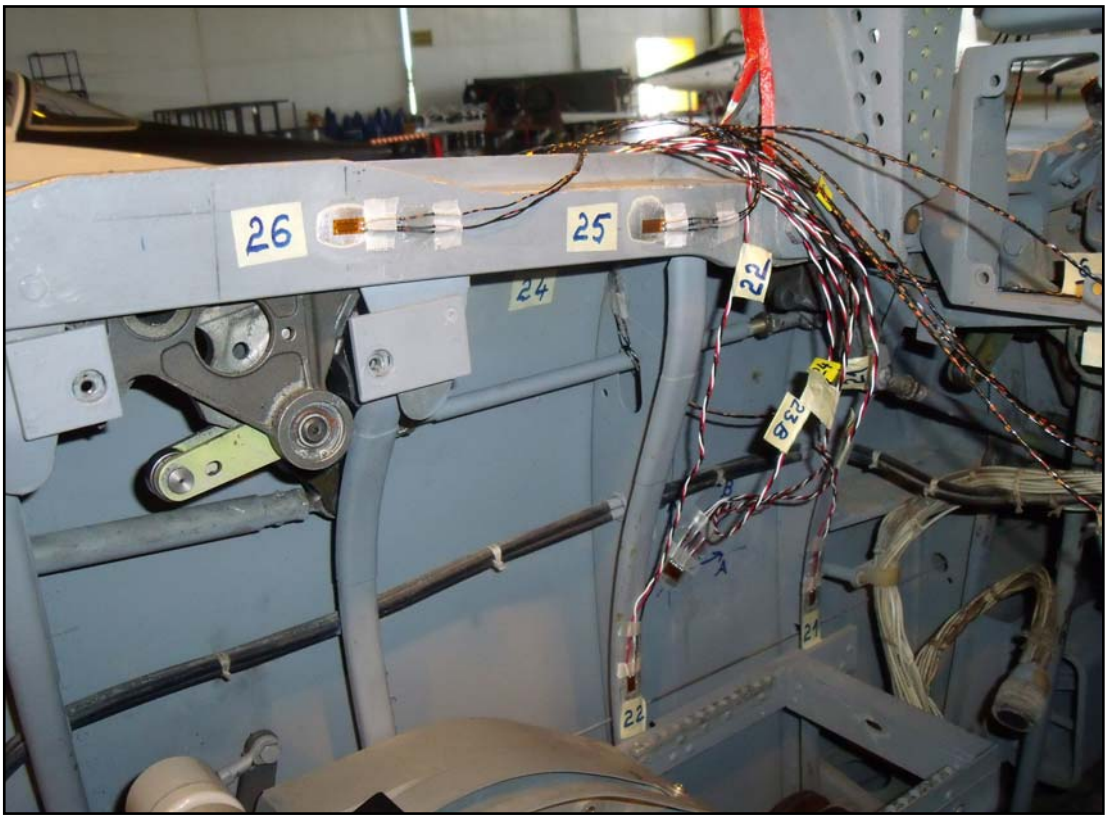

Figure 3.5.10: General view of the strain gauge installation on the cockpit

The number and the locations of the strain gauges installed in to the cockpit are given in Table 3.5.1.

Table 3.5.1: The number and the locations of the strain gauges

Longeron Web (Linear)		Longeron Inner Flange (Linear)		Longeron Outer Flange (Linear)		Skin (Rosette)	
Location	**Number**	**Location**	**Number**	**Location**	**Number**	**Location**	**Number**
B1	1	F4	1	F4	1	F4	1
F1	1	F6	1	F9	1	F13	1
F2	1	F14	1	F12	1	F16	1
F20	1	F15	1	F13	1		
		F18	1				
Frame Inner Cap (Linear)		**Bulkhead Upper Cap (Linear)**		**Tie Bars (Linear)**		**Sheet Support (Linear)**	
Location	**Number**	**Location**	**Number**	**Location**	**Number**	**Location**	**Number**
F2	2	B2	1	F3	1	F1	1
F3	2	B3	1	F12	1		
F4	2						
F5	2						
F6	2						
F12	2						
F13	2						
F14	1						
F17	1						

Total Linear Strain Gauges = 34
Total Rosette Strain Gauges = 3

As there is a structural symmetry in the cockpit, except bulkhead upper caps, strain gauges are installed only on one side of the cockpit. In Table 3.5.1, location information on the longeron, skin and frame is given for only their left hand side parts. The number of the gauges on these structures indicates the number on left hand side longeron, skin and frame. For example, at F2 station, there are actually two frames which are placed at each side of the cockpit symmetrically. However, at F2, two of the strain gauges are installed only on the left hand side frame. Because tie bars and the sheet support lie between the each side of the cockpit, strain gauges are installed on their regions close to the left side. On the bulkhead upper caps, strain gauges are installed on the locations where the installation space is possible.

The numbers of the strain gauges on the structures are determined according to the expected strain distributions on the area of interest. On the upper longeron, strain gauges are distributed by considering the longeron size. It lies over the whole cockpit and because of the supporting structures that are attached to it; there are strain discontinuities over its whole length. Although the skin is located on the whole of the cockpit as the longeron, there are few numbers of strain gauge installed on it. The reason is from the fact that the discontinuities in the strain values are not expected over the skin. Under the cabin pressure, frame deformation highly depends on the deformation of the longerons and the skin. While the canopy hook loads pull the frames upward, lateral cabin pressure forces bend the frames in the radial direction. In order to have a decision for the frame response under cabin pressure, the strain gradients on the frames are investigated by using two strain gauges. The load path on the tie bars, bulkhead upper caps and the sheet support exist mainly in one direction which is actually in a lateral direction. The strain gradient does not vary much over their length and therefore a single strain gauge provides accurate measurement results for the strain levels of these structures.

Pressure Transducer Installation

There are two pressure transducers in the cockpit which are located in front and in rear cockpit. Transducers are attached to the cockpit structures by using tapes. The purpose of locating two pressure transducers is to determine whether there is a pressure gradient or not through the cockpit.

3.6 Data Acquisition System

In this study, data acquisition system consists of NI® CompactRIO-9022 [32] real-time controller and NI® 9205 [33] industrial I/O modules. NI® CompactRIO is programmed with NI ® LabVIEW [34] graphical programming software which collects and analyze the signals and convert them into the physical measurements.

Sensors in the cockpit are connected to the module channels with cables. There are two kinds of modules in the system which are for measuring strain and pressure. Data acquisition system is placed into the cockpit floor during the test. The controller has USB data storage unit and the measured data is stored in the flash memory stick during the test.

3.7 Test Steps

In the study, test steps are carried out as follows:

1) Sensors are connected to the data acquisition system.
2) Data acquisition system is operated and the initial data is started to be taken.
3) The canopies are closed.
4) Pressure supplier unit is operated.
5) The pressure inside the cockpit is increased more than 5 [Psi] step by step during a period of 30 seconds. Additional pressure is given to the cockpit due to the difficulty of controlling the manual control unit located on the supplier and not to miss the data around 5 [Psi].
6) When pressure reach its maximum level, waited at least 10 seconds for the stabilization of the data.
7) Waited minimum 3 seconds for gathering the data.
8) Cabin is depressurised step by step over a period of 30 seconds.
9) When the pressure drops closer to zero, in order to prove the test repeatability, test steps are repeated once more following the steps starting from (5). In other words, two pressure cycles are applied to the cockpit during the test.
10) The canopies are opened when the pressure drops to zero.
11) Data acquisition unit is closed and the data is transferred to a computer by USB memory stick.

3.8 Test Results

In this section, at first, the strain gauge results are given as strain-pressure plots. Secondly, the maximum strain values at 5 [Psi] pressure load are tabulated with their corresponding calculated stress values. For the rosette type strain gauges, the maximum principal stress values are also calculated. Throughout the study, strain and pressure values are given in [με] and in [Psi] units respectively.

Under linearly increasing cabin pressure, all of the strain gauges on the longeron web show linear behaviours. Between the pressurisation and the depressurisation, some of the strain data follows a different path. This situation is known as 'hysteresis'. If a strain gauge is loaded to a high value of strain, resistance value of the gauge has acquired some settled value and during the unloading, all resistance values will have higher values than that of in the loading. Thus, between the loading and unloading, hysteresis loop occurs [35]. For the strain gauges located at the longeron web, these loops are so narrow that do not affect the reliability of the results. Also at maximum pressure, strain gauges read the same strain values in two pressure cycles. The stain-pressure plot shown in Figure 3.8.1 is for the longeron web.

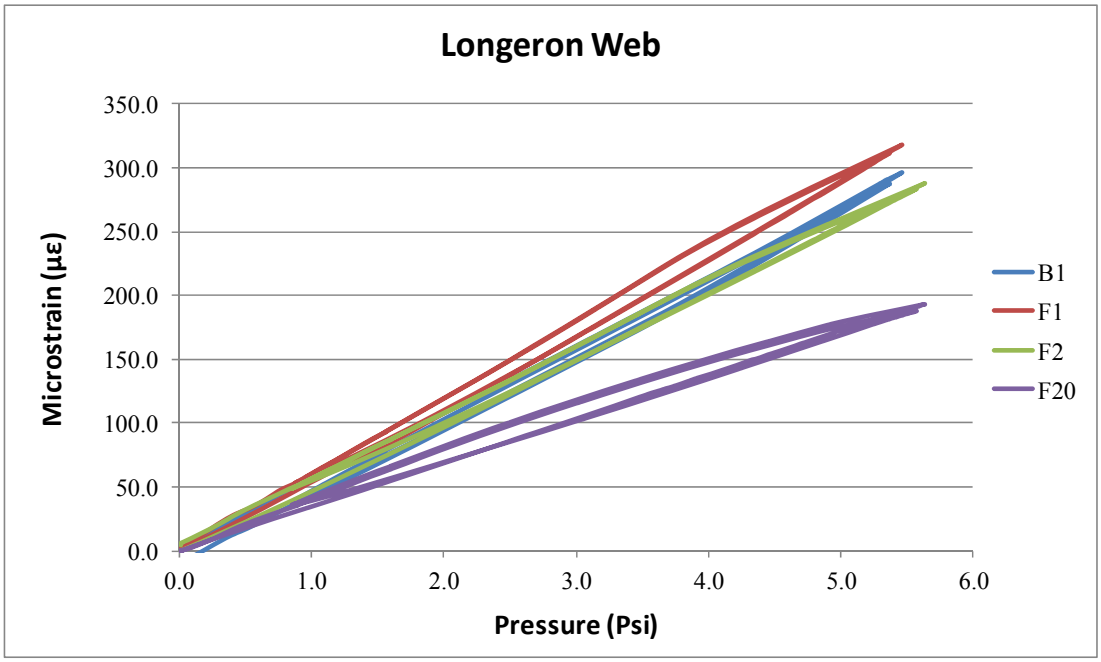

Figure 3.8.1: Longeron web strain-pressure plot

The strain gauges on the longeron inner flanges show linear and non-linear behaviours. At first glance, it seemed that the strain gauges which have non-linear behaviour also have some bonding problems with their bonding surfaces. However, when load is applied by hand in the vicinity of the gauge, strain gauges show linear behaviour. Thus, it is decided that there is not any problem for the installations. The common point for the gauges which show non-linear behaviour is that, their strain values are too low when compared to the gauges which have linear responses. It is thought that, the strain gauges could not response properly for the low strain values where the strains are below the resolution of the gauge. The detailed discussions about the non-linearity of these gauges are made in Chapter 4. For the longeron inner flange, the strain-pressure plot is shown in Figure 3.8.2 and non-linear gauges are shown in Figure 3.8.3.

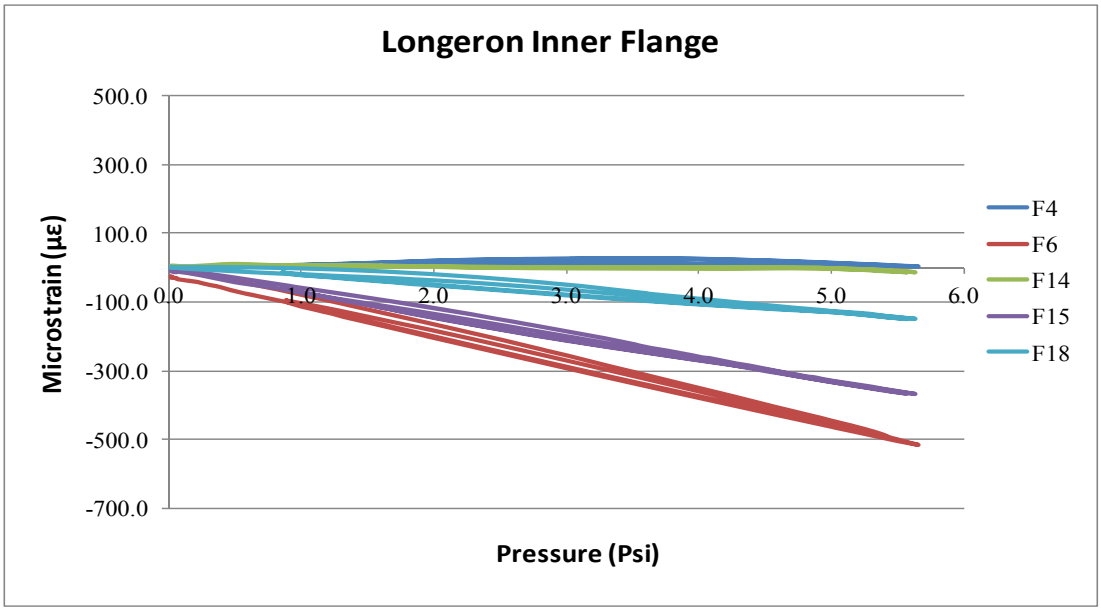

Figure 3.8.2: Longeron inner flange strain-pressure plot

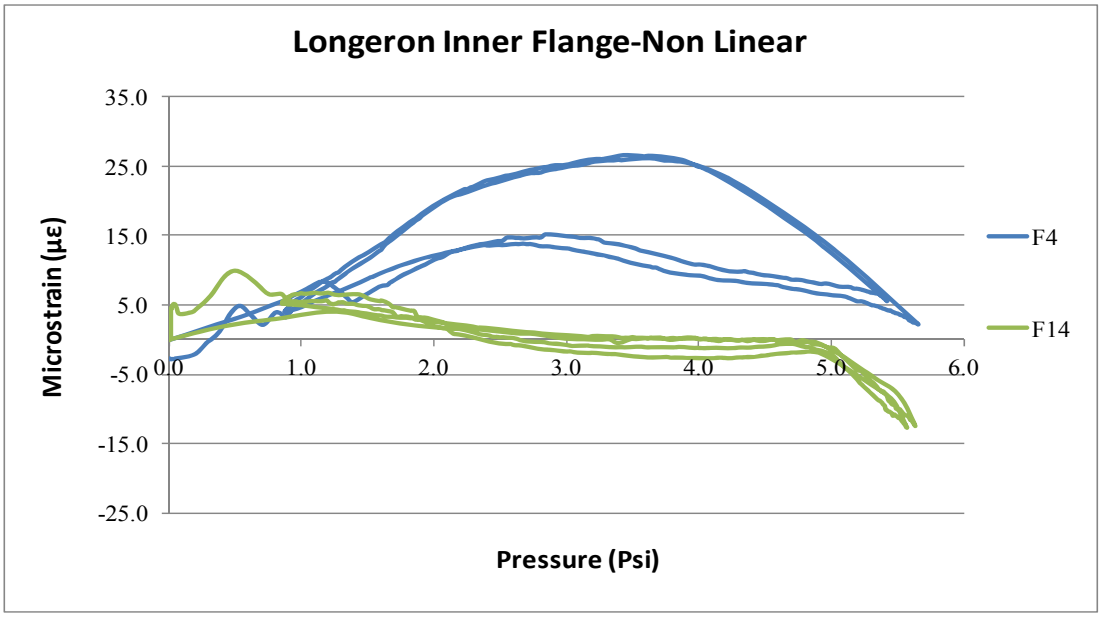

Figure 3.8.3: Longeron inner flange non-linear strain behaviours

The strain gauges on the outer flange of the longeron and the skin show linearity under cabin pressure. The hysteresis loops are also involved and their affects on the results are considered as negligible. While for the longeron outer flange, the strain-

pressure plot is shown in Figure 3.8.4, for the skin, the strain-pressure plot of the three armed rosettes is shown in Figure 3.8.5.

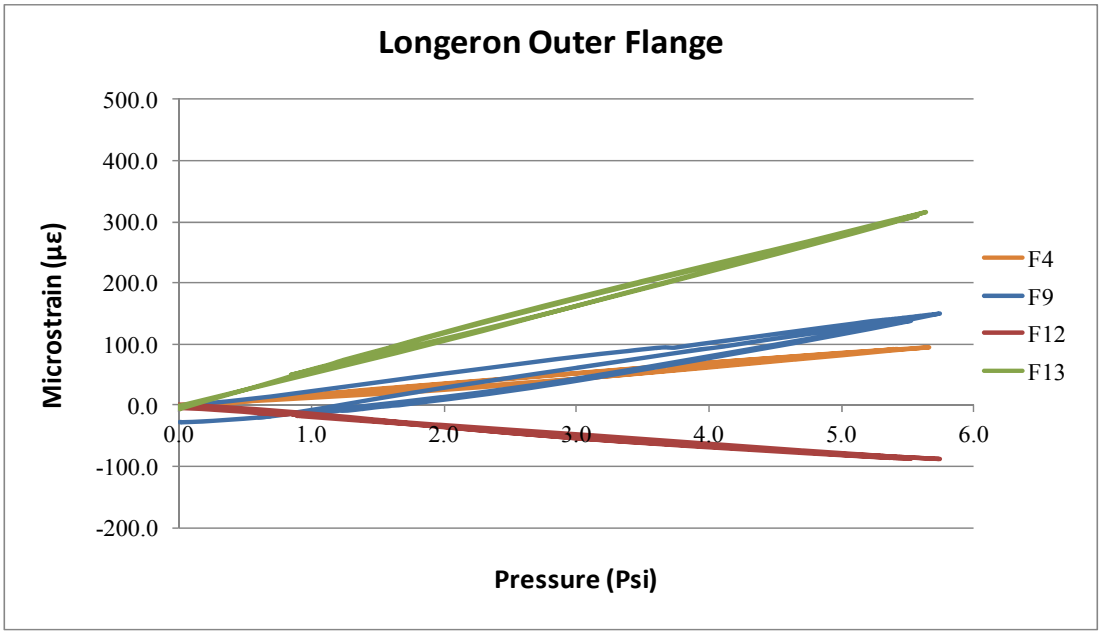

Figure 3.8.4: Longeron outer flange strain-pressure plot

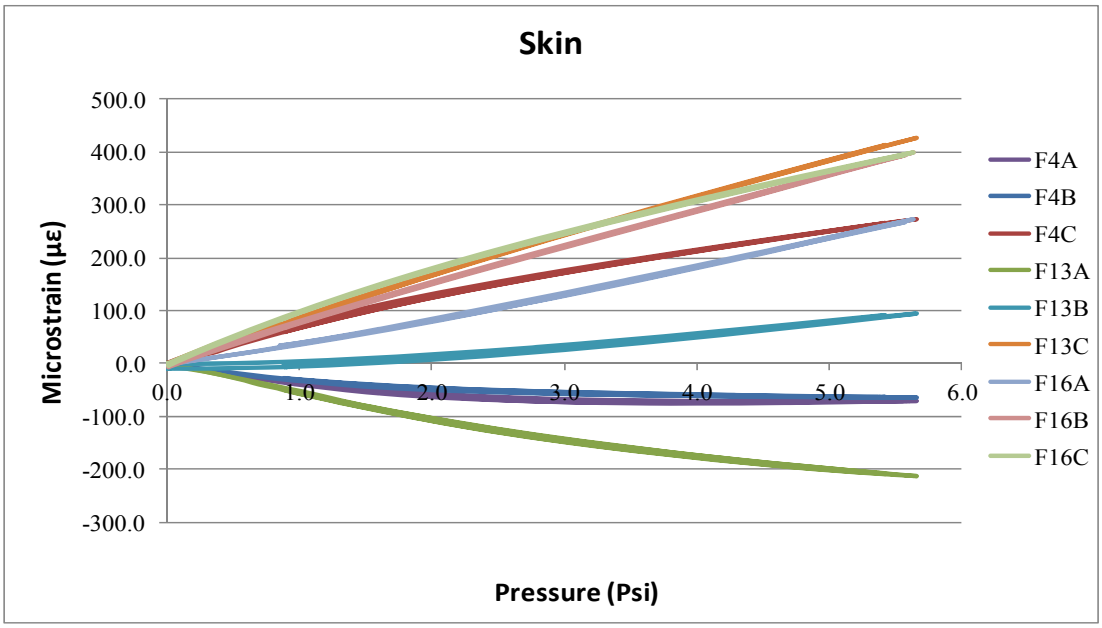

Figure 3.8.5: Skin strain-pressure plot

The strain gauges on the frame inner caps show linear and non-linear behaviours as gauges located at longeron inner flange. The installation checks are made and understood that there is not any problems for the installation. As longeron inner flange, the common point for the gauges which show non-linear behaviour is that, their strain values are too low when compared to the gauges which have linear responses. At the frames where these gauges are located, there are also other gauges and they show linear behaviour under cabin pressure. It is again thought that, the strain gauges could not response properly for the low strain values. The detailed discussions about the non-linearity of these gauges are also made in Chapter 4. For the frame inner cap, the strain-pressure plot is shown in Figure 3.8.6 and non-linear gauges are shown in Figure 3.8.7.

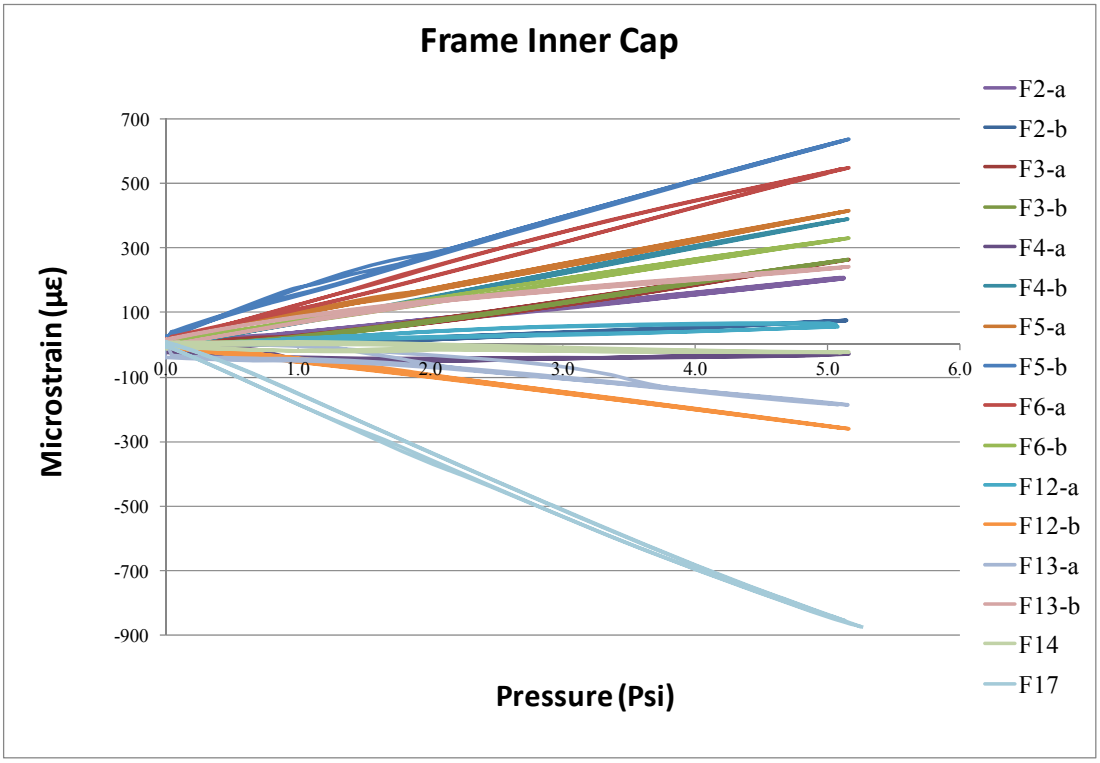

Figure 3.8.6: Frame inner cap strain-pressure plot

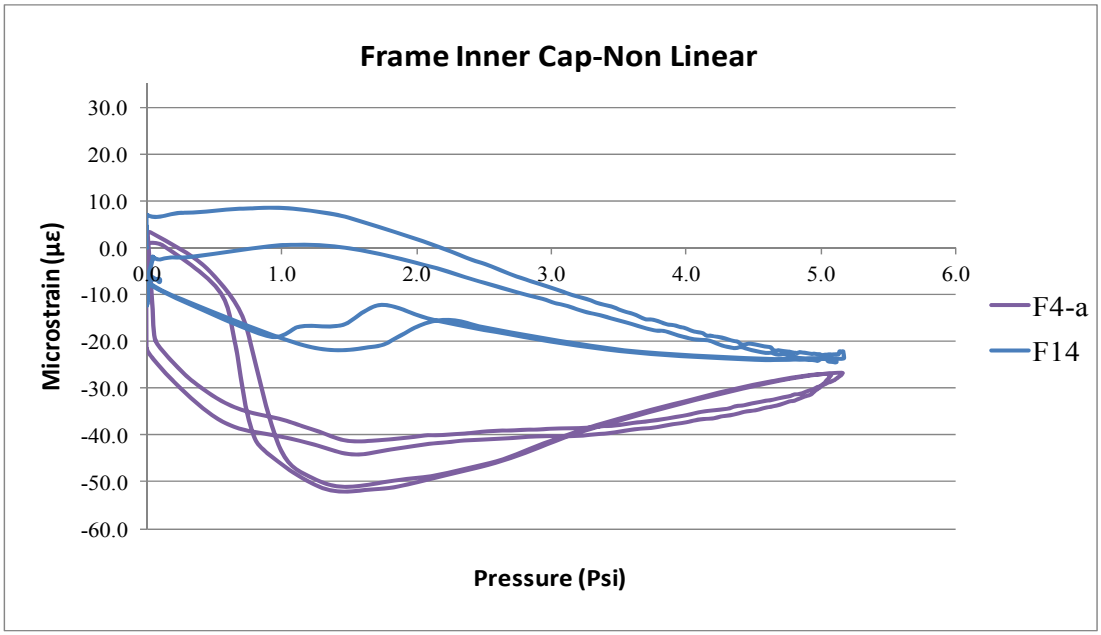

Figure 3.8.7: Frame inner cap non-linear strain behaviours

The linear strain variations under cabin pressure for the strain gauges located at the bulkhead upper cap, ties bars and at the sheet support are shown in the plots from Figure 3.8.8 to Figure 3.8.10.

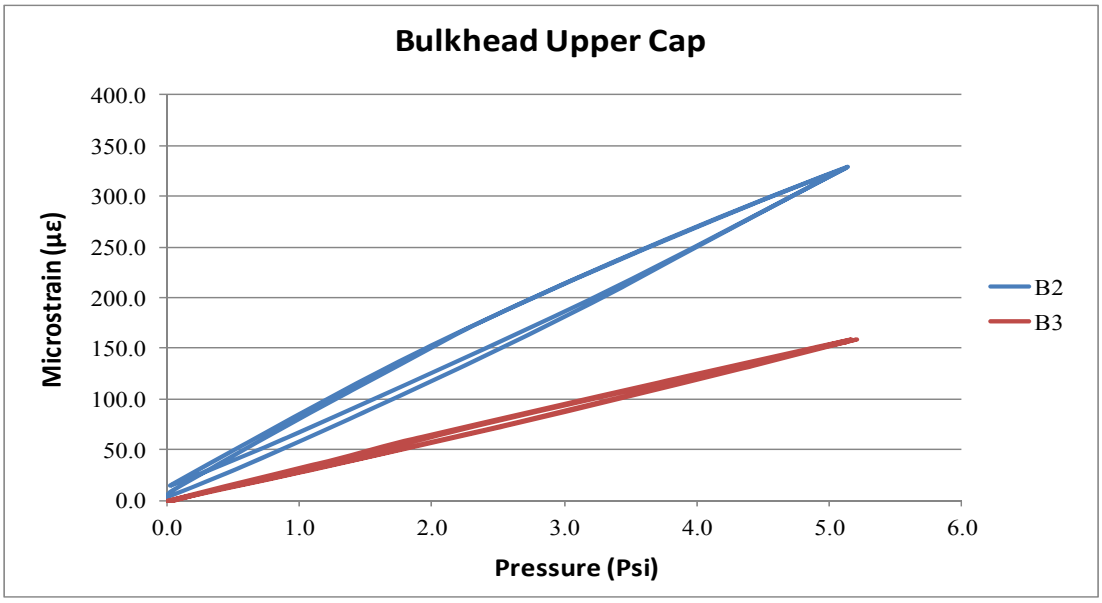

Figure 3.8.8: Bulkhead upper cap strain-pressure plot

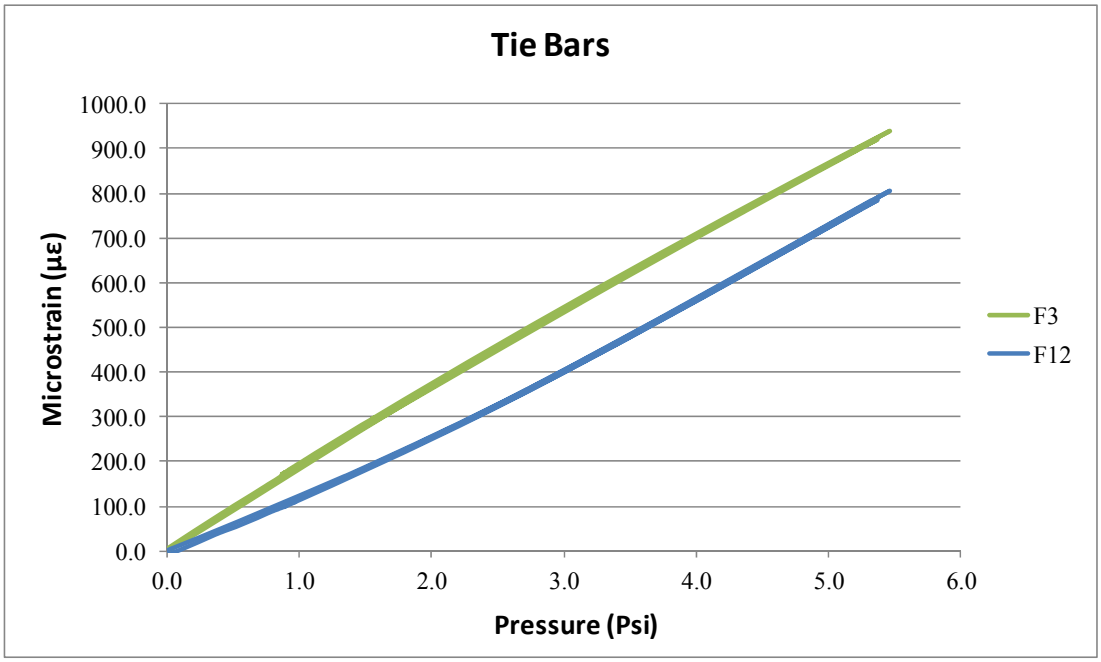

Figure 3.8.9: Tie bars strain-pressure plot

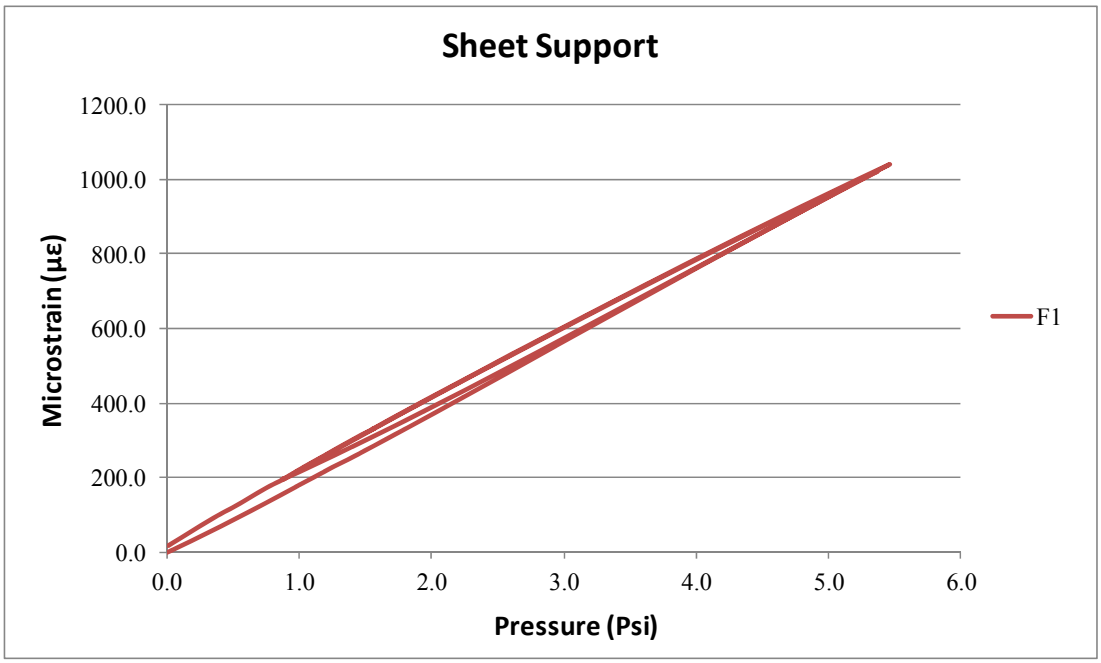

Figure 3.8.10: Sheet support strain-pressure plot

The maximum strain values obtained at 5 [Psi] cabin pressure for the gauges which show linear behaviour under linearly increasing cabin pressure are converted to the stress values by using the Hooke's Law. If the test material is homogeneous and isotropic and if the stress/strain relationship is linear, then the uni-axial and biaxial forms of Hooke's law can be used to convert the principal strains into principal stresses for both linear and rosette types strain gauges.

The Hooke's Law in uni-axial form which is used for calculating the axial stress values from the strain measurements of linear type strain gauges is given in Equation 3.1.

$$\sigma = E \times \varepsilon \qquad \text{(Eqn. 3.1)}$$

where, σ , ε and E are the axial stress, axial strain and modulus of elasticity of the material respectively.

The principal strain calculations for the rosette type strain gauges are derived from the strain transformation graph, which is known as Mohr's circle. According to the Mohr's circle, the normal strain at any angle θ from the principal axis is calculated by Equation 3.2.

$$\varepsilon_\theta = \frac{\varepsilon_P + \varepsilon_Q}{2} + \frac{\varepsilon_P - \varepsilon_Q}{2}\cos(2\theta) \qquad \text{(Eqn. 3.2)}$$

In Equation 3.2, ε_P and ε_Q stand for maximum and minimum principal strains respectively. A rectangular 45^o single-plane rosette type strain gauge which is oriented at θ degrees from the maximum principal direction is shown in Figure 3.8.11. The reflection of this orientation to the Mohr's circle is shown in Figure 3.8.12.

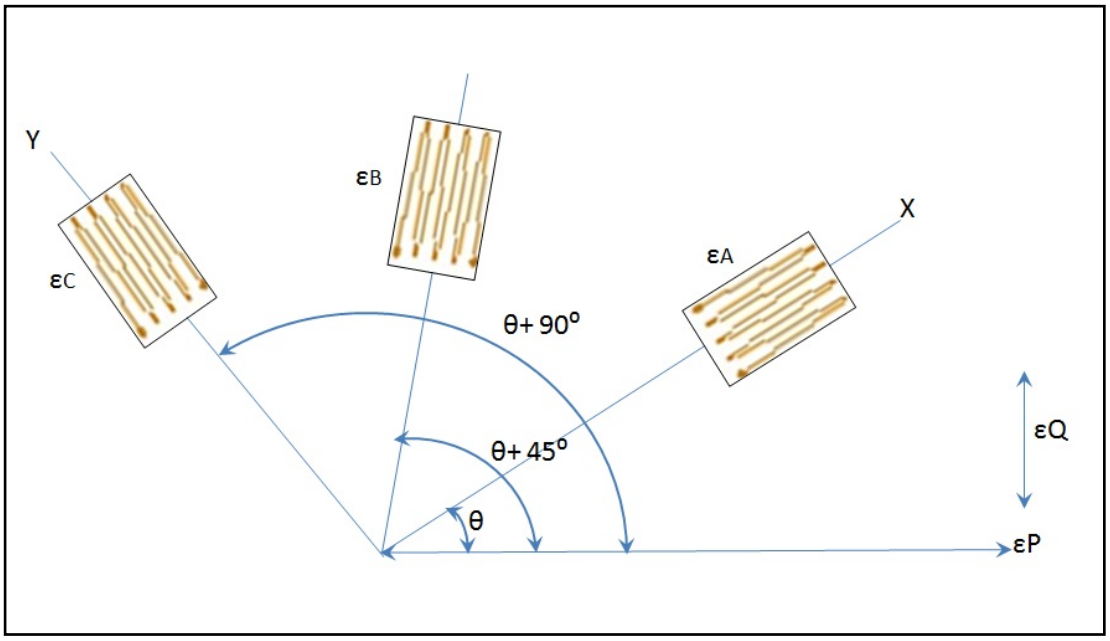

Figure 3.8.11: Orientation of the rectangular rosette

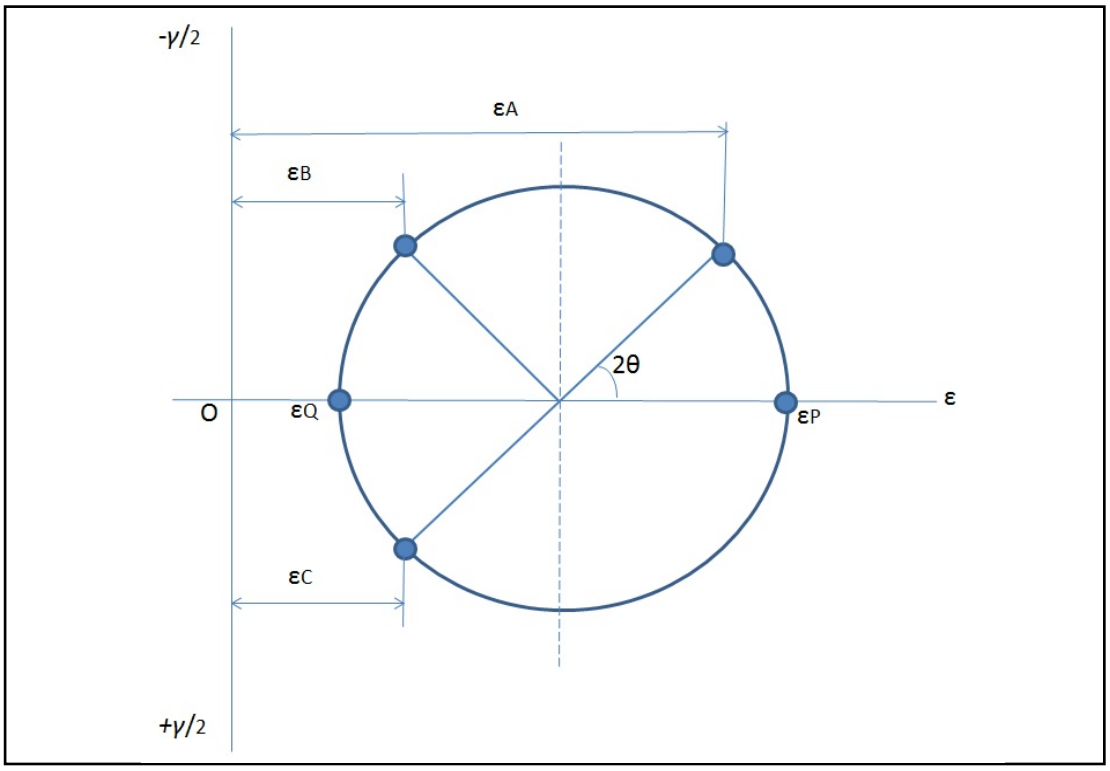

Figure 3.8.12: Mohr's circle for the rectangular rosette

The arms of the rosette gauge with their orientation angles from the maximum principal direction read the strain values according to the equations derived from the Equation 3.2.

$$\varepsilon_A = \frac{\varepsilon_P + \varepsilon_Q}{2} + \frac{\varepsilon_P - \varepsilon_Q}{2}\cos(2\theta) \qquad \text{(Eqn. 3.3)}$$

$$\varepsilon_B = \frac{\varepsilon_P + \varepsilon_Q}{2} + \frac{\varepsilon_P - \varepsilon_Q}{2}\cos 2(\theta + 45^o) \qquad \text{(Eqn. 3.4)}$$

$$\varepsilon_C = \frac{\varepsilon_P + \varepsilon_Q}{2} + \frac{\varepsilon_P - \varepsilon_Q}{2}\cos 2(\theta + 90^o) \qquad \text{(Eqn. 3.5)}$$

Rosette type strain gauge measures the left hand side parameters in the above equations. The unknowns at the right hand sides are found by solving these three equations simultaneously. Thus, principal strain values for the 45^o rosette type strain gauge are calculated according to the Equation 3.6 given below.

$$\varepsilon_{P,Q} = \frac{\varepsilon_A + \varepsilon_C}{2} \pm \frac{1}{\sqrt{2}}\sqrt{(\varepsilon_A - \varepsilon_B)^2 + (\varepsilon_B - \varepsilon_C)^2} \qquad \text{(Eqn. 3.6)}$$

The Hooke's Law in biaxial form is given in Equation 3.7 and Equation 3.8.

$$\sigma_P = \frac{E}{1 - \nu^2}(\varepsilon_P + \nu\varepsilon_Q) \qquad \text{(Eqn. 3.7)}$$

$$\sigma_Q = \frac{E}{1 - \nu^2}(\varepsilon_Q + \nu\varepsilon_P) \qquad \text{(Eqn. 3.8)}$$

where ν is the Poisson's ratio of the material.

The maximum (σ_P) and the minimum (σ_Q) principal stresses are calculated by substituting Equation 3.6 into Equation 3.7 and Equation 3.8. The final form of the equation is given in Equation 3.9 below.

$$\sigma_{P,Q} = \frac{E}{2}\left[\frac{\varepsilon_A + \varepsilon_C}{1-\nu} \pm \frac{\sqrt{2}}{1+\nu}\sqrt{(\varepsilon_A - \varepsilon_B)^2 + (\varepsilon_B - \varepsilon_C)^2}\right] \qquad \text{(Eqn. 3.9)}$$

The maximum strain values at 5 [Psi] pressure load are tabulated with their calculated stress values in Table 3.8.1. In the calculations, elastic modulus (E) and Poisson's ratios (ν) are taken from Table 2.3.2. The gauges which are below the gauge resolution are coloured in yellow. Although Hooke's law is not valid for these gauges, the stress levels are calculated by using this law only to interpret the physical meaning of the data. In this study, these data are evaluated only qualitatively not quantitatively.

Table 3.8.1: The maximum strain and stress values for the strain gauges

Longeron Web	Strain (με)	Stress (ksi)	Longeron inner flange	Strain (με)	Stress (ksi)	Longeron outer flange	Strain (με)	Stress (ksi)
Location			Location			Location		
B1	269	2.8	F4	8	0.1	F4	84	0.9
F1	288	3.0	F6	-448	-4.7	F9	128	1.3
F2	253	2.6	F14	-2	0.0	F12	-81	-0.8
F20	170	1.8	F15	-330	-3.4	F13	279	2.9
			F18	-130	-1.4			

Frame Inner Cap	Strain (με)	Stress (ksi)	Skin	Strain Max/Min. Principal (με)	Stress Max. Principal (ksi)	Bulkhead Upper Cap	Strain (με)	Stress (ksi)
Location			Location			Location		
F2-a	199	2.0	F4	314 / -134	3.1	B2	320	3.3
F2-b	74	0.8	F13	385 / -198	3.7	B3	154	1.6
F3-a	255	2.6	F16	386 / 215	5.4			
F3-b	254	2.6						
F4-a	-27	-0.3	Tie Bars	Strain (με)	Stress (ksi)	Sheet Support	Strain (με)	Stress (ksi)
F4-b	380	3.9	Location			Location		
F5-a	403	4.2	F3	863	9.2	F1	952	9.8
F5-b	618	6.4	F12	725	7.8			
F6-a	531	5.5						
F6-b	321	3.3						
F12-a	55	0.6						
F12-b	-251	-2.6						
F13-a	-182	-1.9						
F13-b	239	2.5						
F14	-23	-0.2						
F17	-834	-8.6						

At it can be seen from the Table 3.8.1 that the maximum stress value calculated for the strain gauge locations is 9.8 [ksi] at the sheet support. This level of stress is too low when compared with the material yield stress limit, which is 70 [ksi] as shown in Table 2.3.2.

3.9 Summary

In this section, ground pressurisation test procedure, sensor types, criteria for selection and installations of the sensors, test steps and the test results are presented. The test results for the real cockpit structures are shown with graphs and maximum values are tabulated in tables. The majority of the strain gauges show linear behaviour under linearly increasing cabin pressure. However, some of the gauges show non-linear behaviours. The reasons for this situation are also mentioned briefly in this section. The more detailed discussion about the physical definition of the non-linear strain gauges is also made in the forthcoming chapter. The strain data obtained from the strain gauges at 5 [Psi] cabin pressure is also converted to the stress values which is used for the correlation study in Chapter 4.

CHAPTER 4

CORRELATION STUDIES BETWEEN FINITE ELEMENT ANALYSIS AND TEST RESULTS

4.1 Introduction

In this part of the study, FEA results for the measured points at ground pressurisation test is compared with the test results and FEM is improved by the examination of the ground pressurisation test data. FEM is also finalised after achieving a good correlation between the FEA and the test results. Firstly, the response of the structures under cabin pressure is checked. The satisfactory FEA is examined by the evaluation of the deformed shapes of the structures. Secondly, for the specific strain gauge (SG) locations, methodologies so as to gather the stress results from the FEM are explained. Thirdly, FEA results and test results are then compared and checks for the correlation are made in detail. Following those, in order to get a better correlation, some actions for updating the FEM are performed and updated results are also presented and discussed. Finally, experimentally validated FEM is obtained and arguments about the validation are concluded.

4.2 Deformation Checks

In FE environment, the satisfactory FEA not only depends on the software but mainly depends on the engineer who is responsible for interpreting the results. Firstly, the boundary conditions of the real structure and structural deformations should reflect to the FEM correctly. In other words, the expectations for the deformed body under specific load have to be meaningful at the first glance. At this stage, generally, interpretation of the results is made by the engineer qualitatively. And if one has some predictions about the response of the structure calculated before using the analytical solution techniques, quantitative examination could also be made by the engineer during the interpretation of the results. In this study, however, the prediction of the response of the complex integrated cockpit structure under complex type cabin pressure load is extremely challenging subject and for this reason, the deformed shapes of the structure are examined only qualitatively. The deformation result for the upper longerons under 5 [Psi] cabin pressure load is shown in Figure 4.2.1 and they are exaggerated for the illustration purposes.

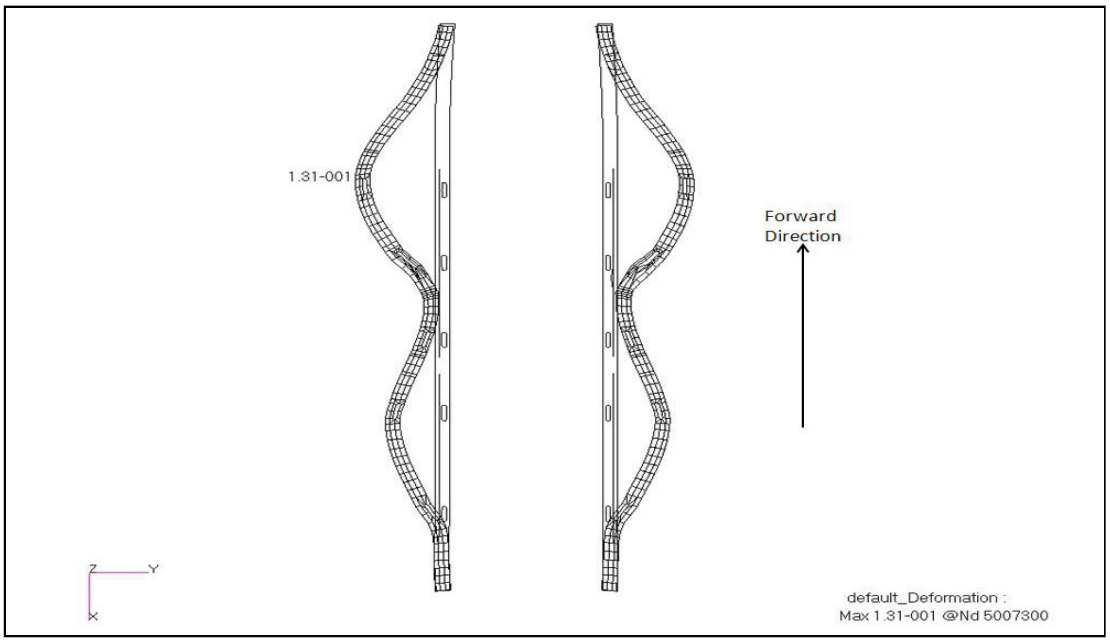

Figure 4.2.1: Deformation of the upper longerons under cabin pressure-Top view

Under cabin pressure, the upper longerons deform symmetrically as expected. The boundary conditions assigned at the rear side prevent the translational motions while rotational motions are free in the model. At the front side, both the sheet support and front tie bar support the longerons laterally and at bulkhead-2, longerons do not deform much. At this location, cross tie bar and bulkhead-2 support the longerons as expected. The maximum obtained deflection is 0.131 [in].

Under cabin pressure, generally, frames carry the tangential stresses from the skin and normal stresses from the cabin pressure. In this case however, they also carry canopy hook and floor loads. Floor pressure loads push the bottom frames down and canopy hook loads bend and pull the side frames to the upward direction. This combined loading cause frames to stretch, bend and twist. The deformation result of the frames under 5 [Psi] cabin pressure load is shown in Figure 4.2.2. The deformations are exaggerated again for illustration purposes and the maximum deflection is 0.122 [in].

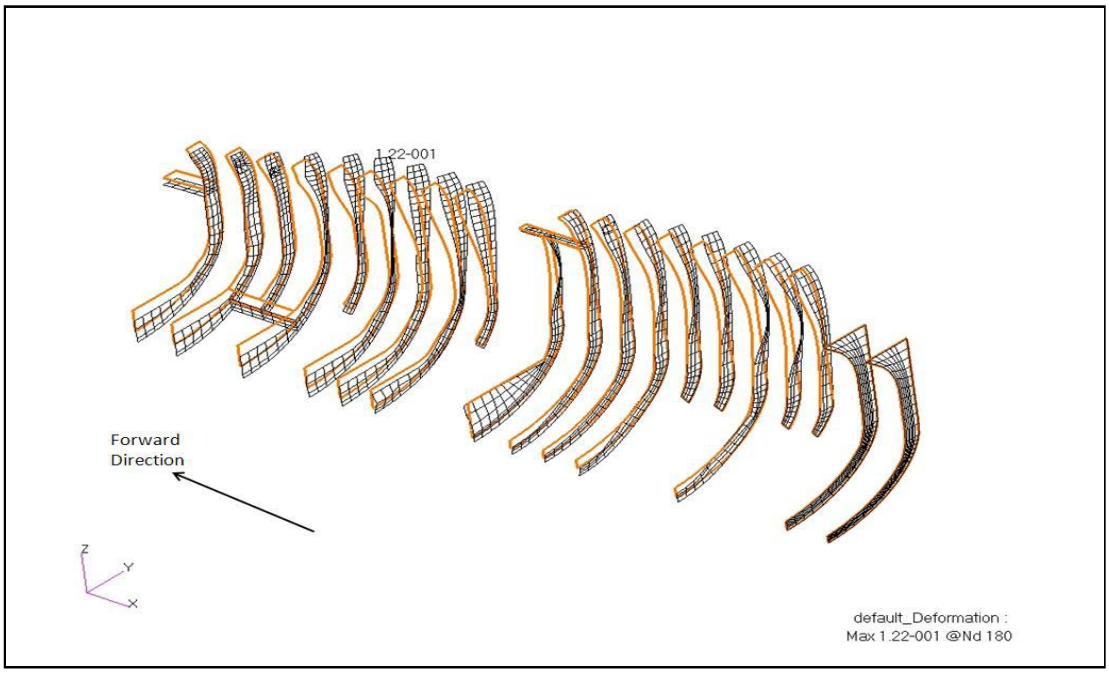

Figure 4.2.2: Deformation of the frames under cabin pressure

Figure 4.2.3 shows combined deformations on some of the frames in a close-up view. On the frames, there are inflection points which reflect the regions where compression-tension stress transition occurs suddenly.

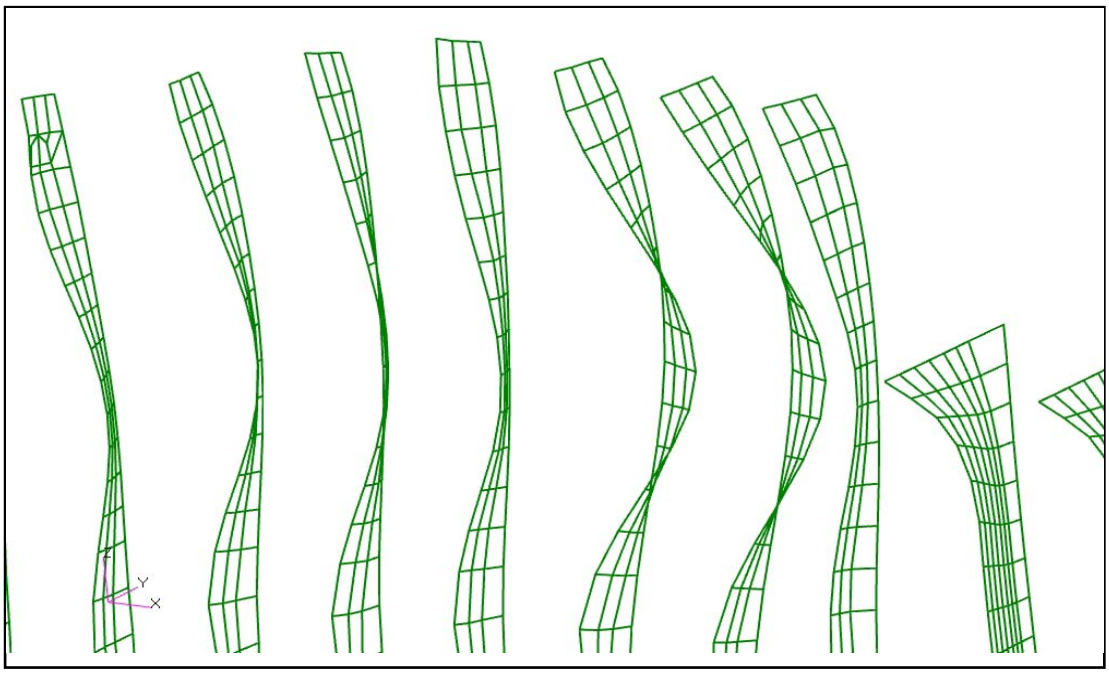

Figure 4.2.3: Deformation of the frames under cabin pressure (close-up view)

The deformations of the longerons and frames are taken as reference to check whether the FEA is providing meaningful results or not. Because the performance of the secondary structures which support longerons and frames, namely; sheet support, tie-bars, horse-shoe and windshield can be decided by examining the deformations of the longerons and the frames. Skin response is also expected to be reliable when longeron and frame response are satisfactory. The reason is that skin covers all of the longerons and the frames in the cockpit. By using these deformation results, the boundary conditions can also be checked whether they reflect the real physical constraints or not. At the first glance, longeron model seems to be validated. For the unpredictable frame deformations, decisions for the validation of frame structures will be made after comparing the FEA results with the test results.

4.3 Methodology to Interpret the Results

After the construction of the FEM in PATRAN®, the interpolating functions/shape functions are automatically selected by the software. These shape functions for each element represent the field variable in terms of degrees of freedom (DOF). In the structural analysis, these DOF's, in other words, nodal variables are the node displacements solved by the NASTRAN® in its system of equations. When these nodal displacements are found, by defining stress/strain relations and strain displacement relations, strains, stresses and forces can be calculated easily. By using these shape functions, the known nodal displacements can be interpolated through the assemblage of the elements and at any points in the domain, field variable can be found. Therefore, the displacement at any point inside the element is the function of the displacements at the corners of that particular element.

In this study, the shape functions defined within the CQUAD4 and CBEAM elements are linear functions. The strain gauges are placed on these types of elements in FE environment. According to the SG dimensions, element refinements are made on the CBEAM elements to match the element size with the SG size. The mesh refinements on 1-D elements are made easily by breaking the coarse ones into desired finer dimensions. Therefore, FEA result for the region where strain gauge is installed in CBEAM elements is gathered directly from these refined 1-D elements. Because the model is created by using coarse mesh methodology, for the strain gauges where installed on CQUAD4 elements on the FEM, the dimension of the SG does not suit always with the 2-D element size. In those situations, the refinement or breaking the CQUAD4 element affects its neighbouring elements too much. The reason for this is that nodal connectivity should be provided for the new elements after each breaking operation. Therefore, FEA results in 2-D element for the region where strain gauge is installed is gathered by using shape functions.

2-D Element Results

In PATRAN®, there is a default averaging domain to average all elements nodal results at each node. However in this study, because the SG measurements in the test are done for specific points, the results for these points in FEA have to be gathered from the specific 2-D element results. Therefore, averaging is not performed during the post processing of the 2D element results. As it is also mentioned before, shape function is used for the SG results in FEA. In PATRAN®, the surfaces of the plate are named as the Z1/Z2 layers which locate at the distances from the mid-surface of the plate as half of the thickness symmetrically. Because SG is placed on one of the faces of the actual 3-D structure in the test, the FEA results are gathered according to that surface and Z1 and Z2 results are examined according to this requirement.

The stress results of the elements are gathered according to the element local coordinate system. In order to compare with the test results, maximum principal stress values from the FEA are obtained by considering these element coordinate systems. Element coordinate system for 2-D elements is shown in Figure 4.3.1.

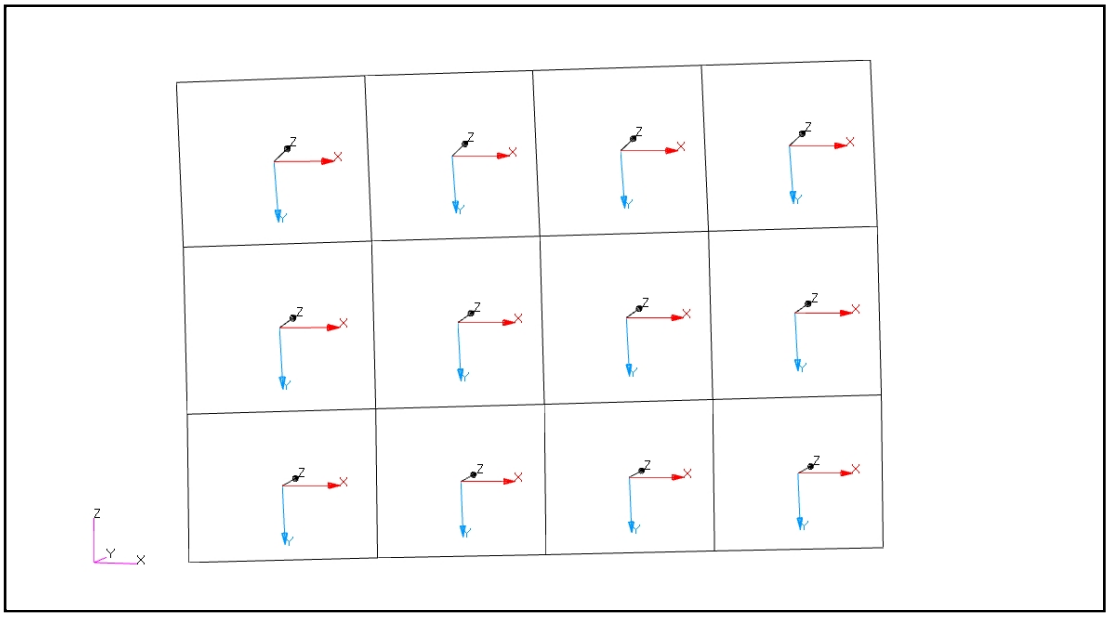

Figure 4.3.1: Element coordinate systems on 2-D elements

In Figure 4.3.2, the discontinuities on stress variations between the groups of CQUAD4 elements modelled for the skin can be seen by none-averaging the nodal values. Here, the stress variation on the elements is obtained under 5 [Psi] cabin pressure. The layer selection (Z1/Z2) for the other groups of CQUAD4 elements on the skin is shown in Figure 4.3.3. Here, the stress results are obtained from the Z1 (inner) side of the elements.

Figure 4.3.2: Stress plot that has no element to element averaging at the nodes.

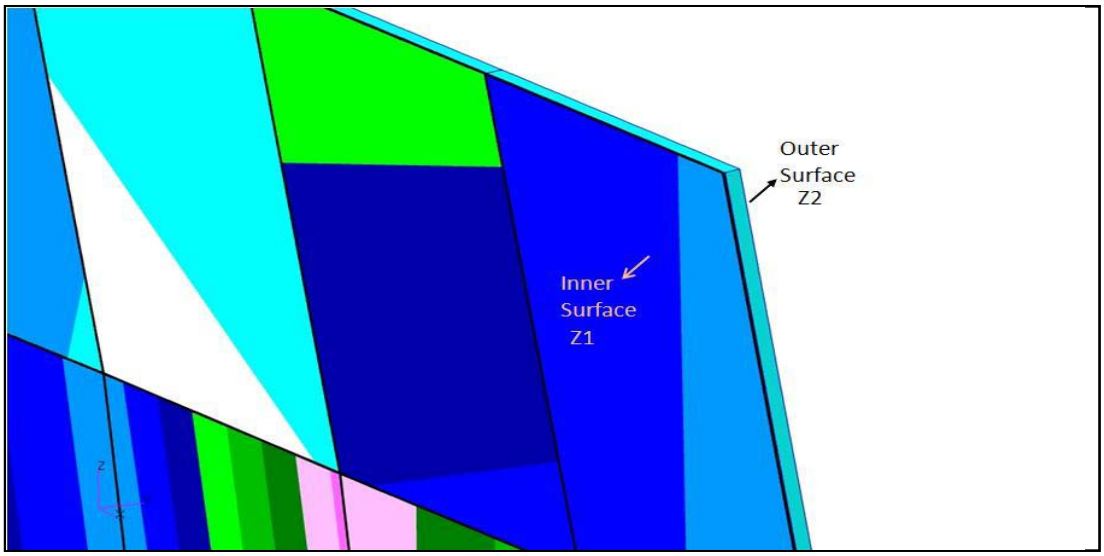

Figure 4.3.3: The layer selection (Z1/Z2) for 2-D skin elements

1-D Element Results

As mentioned before, FEA result for the region where SG is installed in 1-D element is gathered directly from the refined elements which suit with the dimension of the SG. During the modelling of 1-D element that has standard cross-section type, the stress recovery points are defined automatically by the NASTRAN®. With these predefined points, cross section of the beam element is also defined and by considering the element coordinate system, section properties and moments of inertia values are then calculated. In beam elements, the stress recovery points (C, D, E and F) in the element coordinate system are located at each end of the beam element and specified relative to the shear centre of the beam cross-section. The stress recovery points created by the NASTRAN® on a standard rectangular beam cross section are shown in Figure 4.3.4.

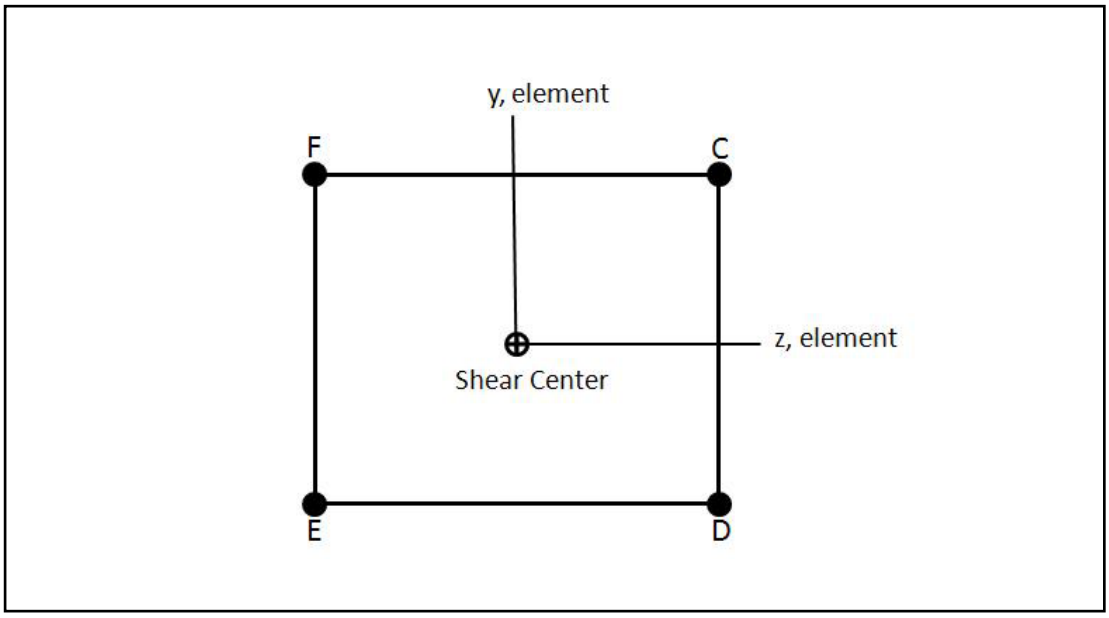

Figure 4.3.4: The stress recovery points on beam cross section

The SG installation face considered for the stress result in FEA is shown on beam element in Figure 4.3.5. Here, both SG dimension and beam element size are nearly the same between two nodes.

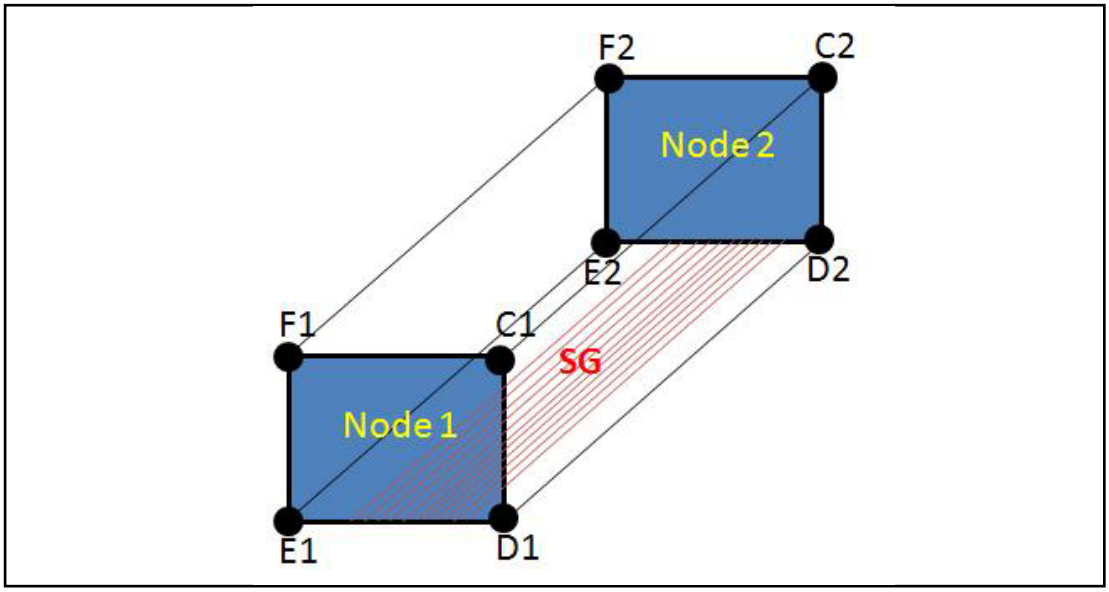

Figure 4.3.5: SG installation on beam element

The stress values on the stress recovery points are calculated for each cross section. Therefore, C, D, E and F values across a beam can be obtained. After this stage, the decision should be made for the face selection in order to get results from true SG location. In Figure 4.3.5, the SG face of the beam element is $D_1D_2E_2E_1$ plane. In order to get the stress results for this SG, D and E stress values are considered across an element. The gathered stress values are a type of combination of axial and bending stresses acting on each of these stress recovery points. At the final stage, the combined stress variations on two edges of the SG plane are averaged to gather the final beam stress value for the SG.

4.4 Checks for FEA and Test Results Correlation

In this part of the study, the stress results gathered from ground pressurisation test are compared with FEA stress results obtained in 5 [Psi] cockpit pressure load and checks are made for FEA and Test results correlation. The comparison of the stress results are tabulated in Table 4.4.1.

Table 4.4.1: The comparison between test and FEA results

Longeron Web	Stress (ksi)	Stress (ksi)	Longeron inner flange	Stress (ksi)	Stress (ksi)	Longeron outer flange	Stress (ksi)	Stress (ksi)
Location	TEST	FEA	**Location**	TEST	FEA	**Location**	TEST	FEA
B1	2.8	2.7	F4	0.1	-2.3	F4	0.9	1.8
F1	3.0	2.6	F6	-4.7	-6.4	F9	1.3	-0.5
F2	2.6	2.8	F14	0.0	-1.8	F12	-0.8	2.3
F20	1.8	1.5	F15	-3.4	-3.7	F13	2.9	4.9
			F18	-1.4	0.6			

Frame Inner Cap	Stress (ksi)	Stress (ksi)	Skin	Stress Max. Principal (ksi)	Stress Max. Principal (ksi)	Bulkhead Upper Cap	Stress (ksi)	Stress (ksi)
Location	TEST	FEA	**Location**	TEST	FEA	**Location**	TEST	FEA
F2-a	2.0	2.9	F4	3.1	3.4	B2	3.3	2.8
F2-b	0.8	1.5	F13	3.7	4.1	B3	1.6	1.4
F3-a	2.6	3.4	F16	5.4	5.0			
F3-b	2.6	2.3						
F4-a	-0.3	4.7	**Tie Bars**	**Stress (ksi)**	**Stress (ksi)**	**Sheet Support**	**Stress (ksi)**	**Stress (ksi)**
F4-b	3.9	3.9	**Location**	TEST	FEA	**Location**	TEST	FEA
F5-a	4.2	4.7	F3	9.2	9.6	F1	9.8	10.2
F5-b	6.4	6.0	F12	7.8	8.4			
F6-a	5.5	5.4						
F6-b	3.3	3.0						
F12-a	0.6	0.3						
F12-b	-2.6	-1.7						
F13-a	-1.9	-1.2						
F13-b	2.5	1.5						
F14	-0.2	0.2						
F17	-8.6	-8.5						

When magnitudes of the stress levels are inspected in Table 4.4.1, at first glance, FEA stress results have approximately same order of magnitude with test results for the most of the SG locations. For the gauges, which has strains that are below the gauge resolution in the test (coloured in yellow), results do not match in magnitude and also in sign. Also there are sign and magnitude differences in FEA and test stress results for longeron outer flange locations at F9 and F12, and longeron inner flange location at F18. The percentages of difference between test and updated FEM and results are given in Table 4.4.2.

Table 4.4.2: The percentage of difference between test and FEM results

Longeron Web	Difference (%)	Longeron inner flange	Difference (%)	Longeron outer flange	Difference (%)
Location	TEST-FEA	Location	TEST-FEA	Location	TEST-FEA
B1	-3	F4	-2864	F4	106
F1	-13	F6	37	F9	-138
F2	6	F14	8554	F12	-373
F20	-15	F15	8	F13	69
		F18	-144		

Frame Inner Cap	Difference (%)	Skin	Difference (%)	Bulkhead Upper Cap	Difference (%)
Location	TEST-FEA	Location	TEST-FEA	Location	TEST-FEA
F2-a	41	F4	9	B2	-16
F2-b	97	F13	11	B3	-13
F3-a	29	F16	-8		
F3-b	-12				
F4-a	-1667	Tie Bars	Difference (%)	Sheet Support	Difference (%)
F4-b	0	Location	TEST-FEA	Location	TEST-FEA
F5-a	13	F3	4	F1	4
F5-b	-6	F12	8		
F6-a	-1				
F6-b	-9				
F12-a	-47				
F12-b	-34				
F13-a	-36				
F13-b	-39				
F14	-184				
F17	-1				

In the literature, there is not any defined percentage of difference to check the correlation between FEA and test results for the static analyses. In some applications while 20% is acceptable, in others even 1% is unacceptable. However, limitation mainly depends on the order of magnitude of the inspected stress levels. As a general practice, if the stress levels are too high, even in small percentage of difference, the magnitude of the errors will be also too high and these high errors lead engineer to get misleading results during his checks for the structural failure modes such as material failure. Also, such high stress errors affect the fatigue life and crack initiation calculations of the structures. In this study however, maximum stress value calculated from the test is 9.8 [ksi]. This level of stress is too low when compared

with the material yield stress limit, which is 70 [ksi] (Table 2.3.2). The percentage errors between the results given in Table 4.4.2 are unrealistic due to these low stress levels. In the study, test and FEA correlation is checked by considering the stress differences with their order of magnitude not the percentage errors.

As it is seen from the Table 4.4.1, for the longeron web, a considerable correlation is satisfied between the test and the FEA stress results. The difference in stress values at the F20 location is due to the simply supported boundary condition assigned at B4. The real elastic effects are not included at the end of the cockpit FEM due to the assumed fix condition in that region. Although simulating the real deformation slope of the upper longerons at this location in the FEM is very difficult, the displacement boundary condition provides a sufficient approximation for the longeron web regarding the obtained result. At the front side of the cockpit, the differences between results are due to the elastic end effect at B1 and sheet support connection at F1. However, the stress values are at most 0.4 [ksi] lower in FEA than stress values measured in test. This value is acceptable when considering the material yield stress limit of the longeron which is 70 [ksi] as shown in Table 2.3.2. This means that, such low order error does not give rise to big deviations during the structural analyses which are to be re-performed on the FEM.

When longeron inner flange results are inspected, satisfactory correlation can be seen on the F15 location. At the rear side of the cockpit, the results for the longeron inner flange are affected as the longeron web from the fix condition assigned at this particular region. However this time, the stress value between test results and FEA at F18 station differs not only in magnitude but also in its sign. The stress is measured as compressive in the test while gathered as tension in FEA. However, the compression-tension band is so narrow and very close to the zero stress line. The stress variation of the longeron at F18 station is shown in Figure 4.4.1. The curvature from fix point to the F18 station determines the sign of the stress.

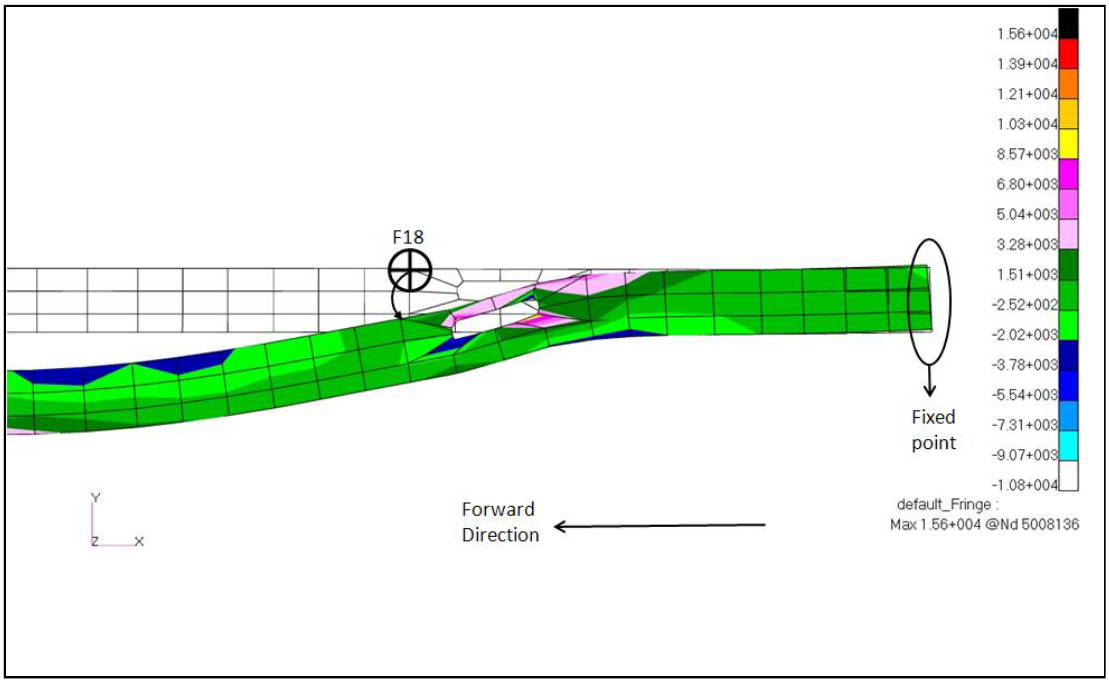

Figure 4.4.1: Longeron stress variation at F18 station-Top view

The test results for the strain gauges located at F4 and F14 stations on longeron inner flange is already given in Chapter 3. These gauges have strains that are below the gauge resolution and their strain values are too low when compared to the gauges which have linear responses. After the checks and confirmations for the installations, the reasons of such behaviour are discussed in this section. The FEA results for these gauges are not as low as expected. Upper longerons deform in lateral and vertical directions under the cabin pressure. The combination of canopy hook loads and side pressure loads deform the longerons and final deformed body takes its shape according to the support points of the longerons such as frames, bulkheads, sheet support, tie bars and horse shoe. The translational and rotational deformation cause stress transition points occurring locally on the structure. The sign of the stresses begin to change through these points and at the very vicinity of these points, stresses become nearly zero as in the case of neutral points on the structures. Thus, support conditions highly affect the stress values of the longerons, especially at its connection regions with the supports.

At the F3 and F12 stations, there are front and rear tie bars located respectively. Also there is a horse shoe located between the F12 and F13. These lateral support structures for the upper longerons affect the stresses that exist on the inner flanges of the longerons at F4 and F14 stations. Because of the combined loading at these locations, stress transition points do exist. The results for the F4 and F14 stations have to be refined by considering the lateral supports in detail. Also for station F6, longeron inner flange stress result has to be refined as well. It can be concluded that, longeron deforms more in FEA than they behave in the tests. The FEA longeron inner flange stress distribution through the longitudinal direction (X-direction) of the cockpit is shown with longeron inner flange test results in Figure 4.4.2.

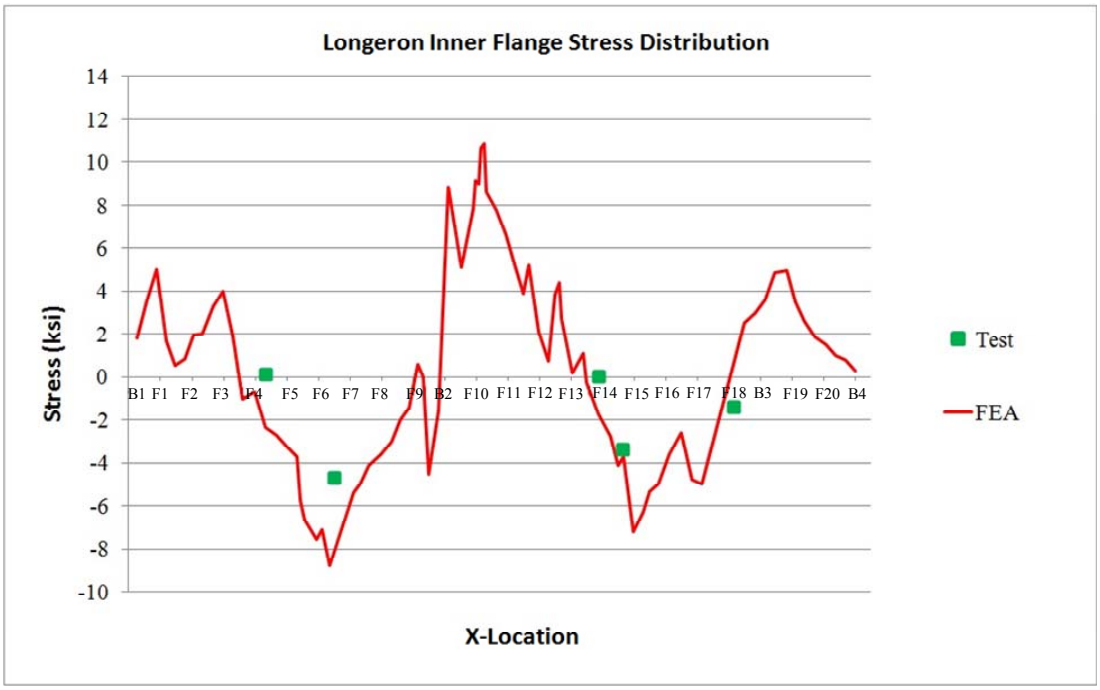

Figure 4.4.2: Longeron inner flange stress distribution with test results

As the inner flange, the longeron outer flange stresses are also affected from the support conditions. The only parameter which is different in the deformation variation for outer flange is its extra support; namely the skin. The U-shape form of

the upper longeron has three sections which are for outer flange, web and inner flange. The inner flange is free except its lateral supports. However, in addition to the lateral supports, outer flange is continuously supported by the skin. Therefore outer flange is less sensitive to deformations than the inner one. This situation is clearly seen from the station F4 results of the inner and the outer flanges. It can be seen from Table 4.4.1 that the test and the FEA results for the outer flange are not compatible with each other. The differences in results are due to the lateral supports as in the case of inner flange. The FEA longeron outer flange stress distribution through the longitudinal direction of the cockpit is shown with longeron outer flange test results in Figure 4.4.3.

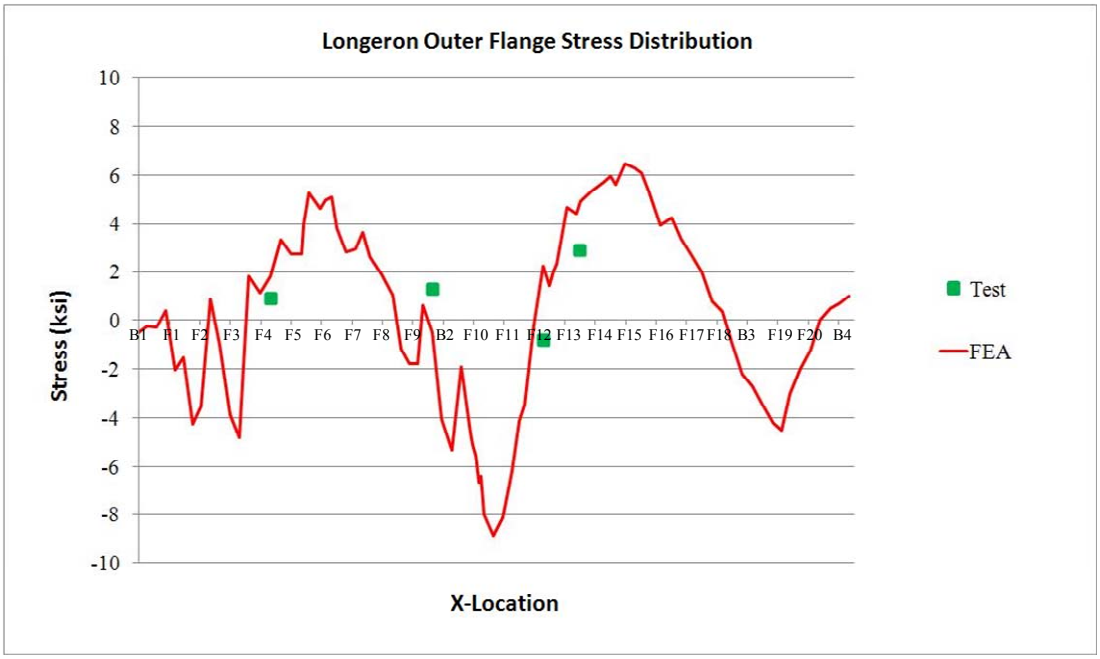

Figure 4.4.3: Longeron outer flange stress distribution with test results

As it is mentioned already, the combination of the side cabin pressure, canopy hook and floor loads cause frames to stretch, bend and twist. As a result of these deformations, stress distributions on the frames show extreme variations. Frame

inner cap stress variations through the height of the frames in FEA are plotted with frame inner cap test results from Figure 4.4.4 to Figure 4.4.12.

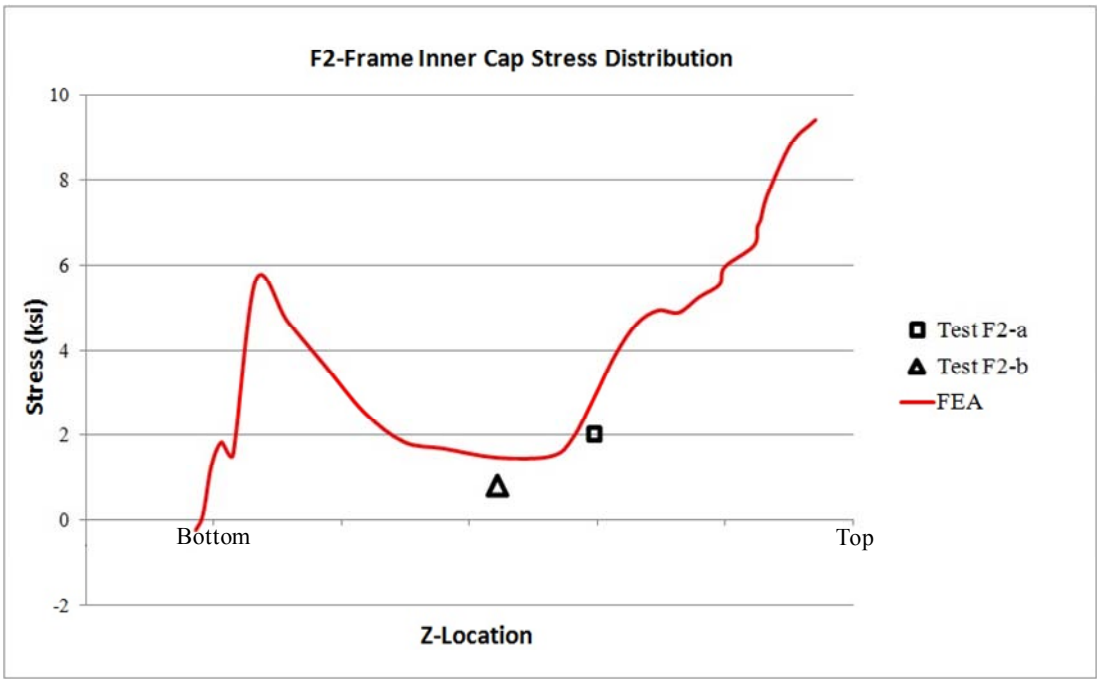

Figure 4.4.4: F2-Frame inner cap stress distribution with test results

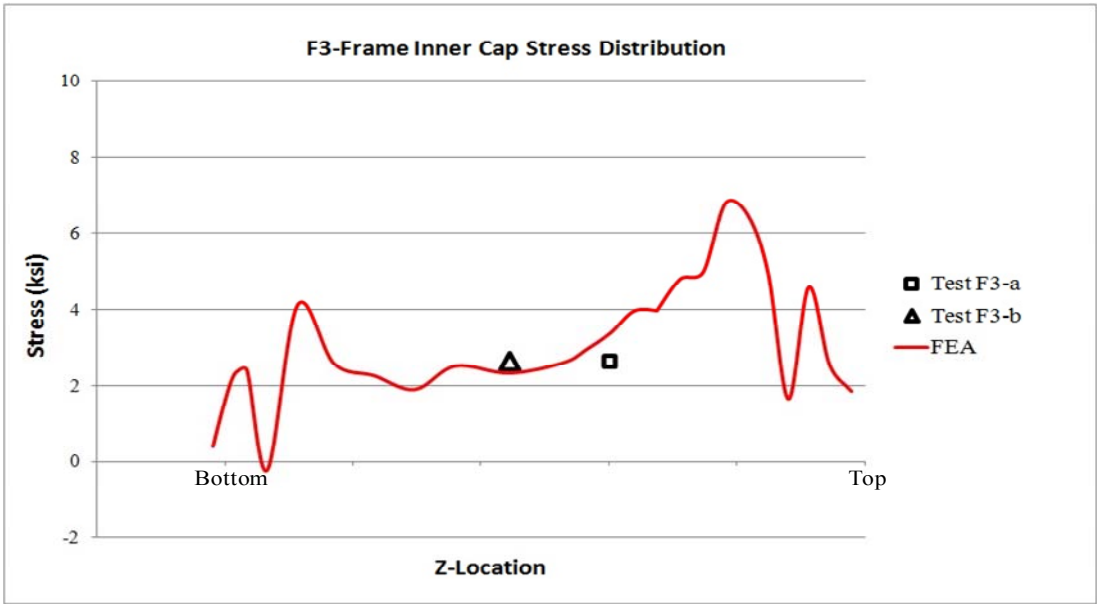

Figure 4.4.5: F-3 Frame inner cap stress distribution with test results

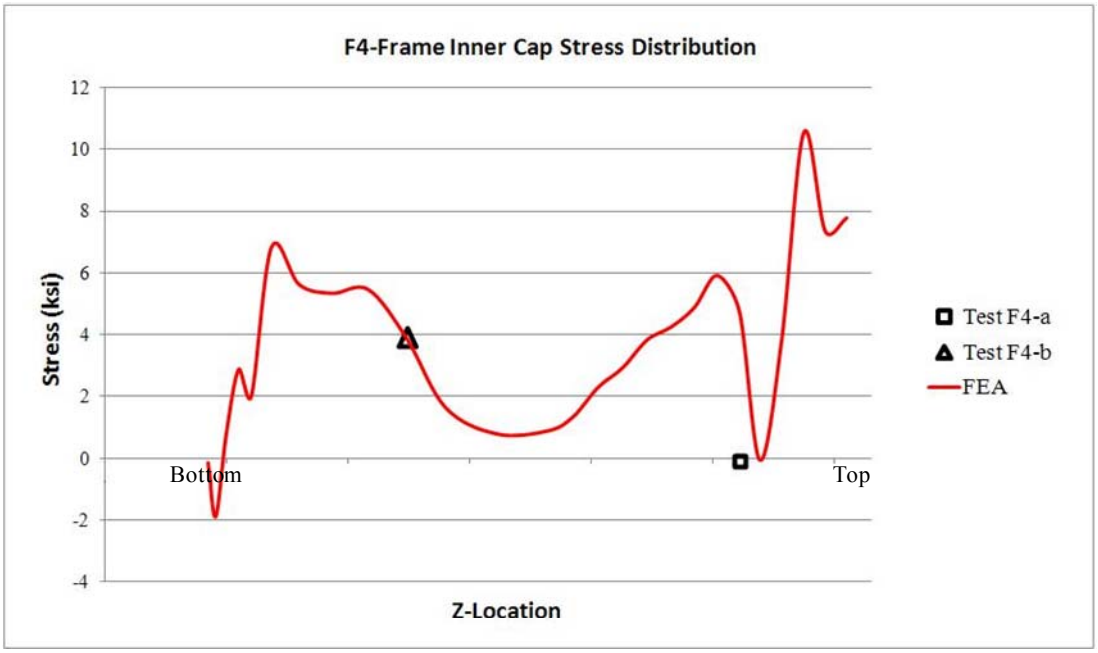

Figure 4.4.6: F4-Frame inner cap stress distribution with test results

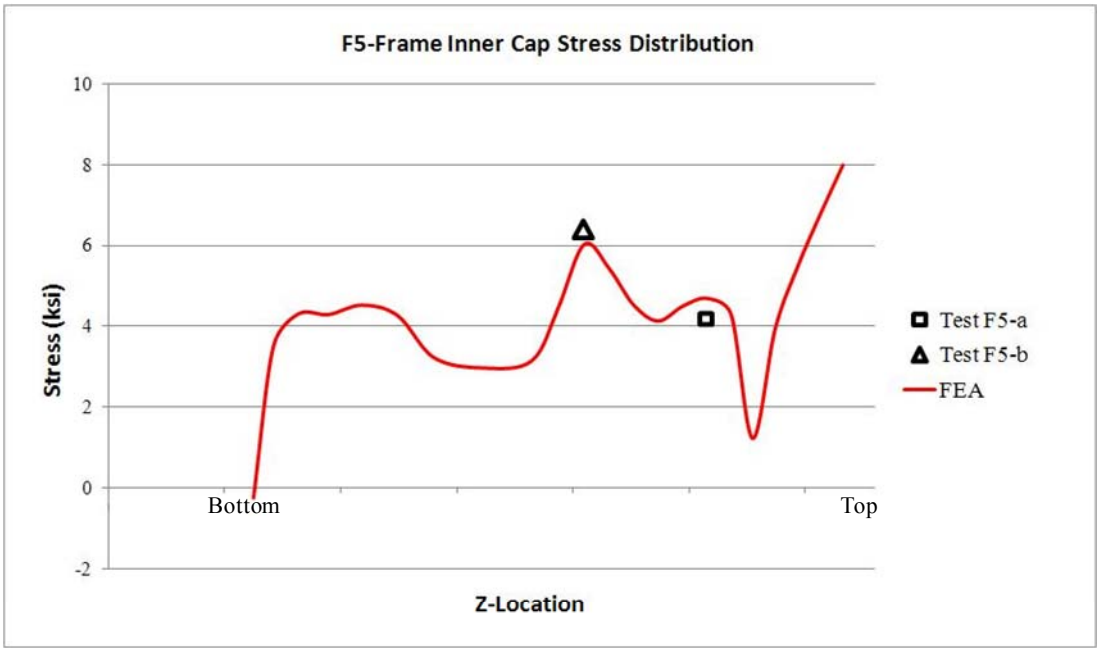

Figure 4.4.7: F5-Frame inner cap stress distribution with test results

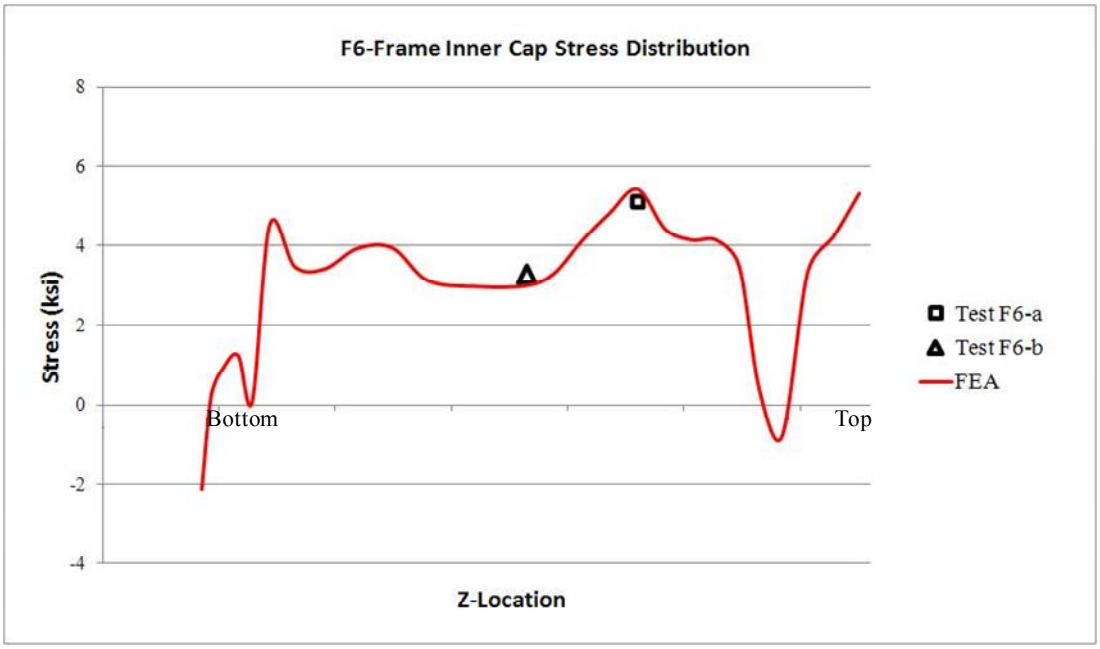

Figure 4.4.8: F6-Frame inner cap stress distribution with test results

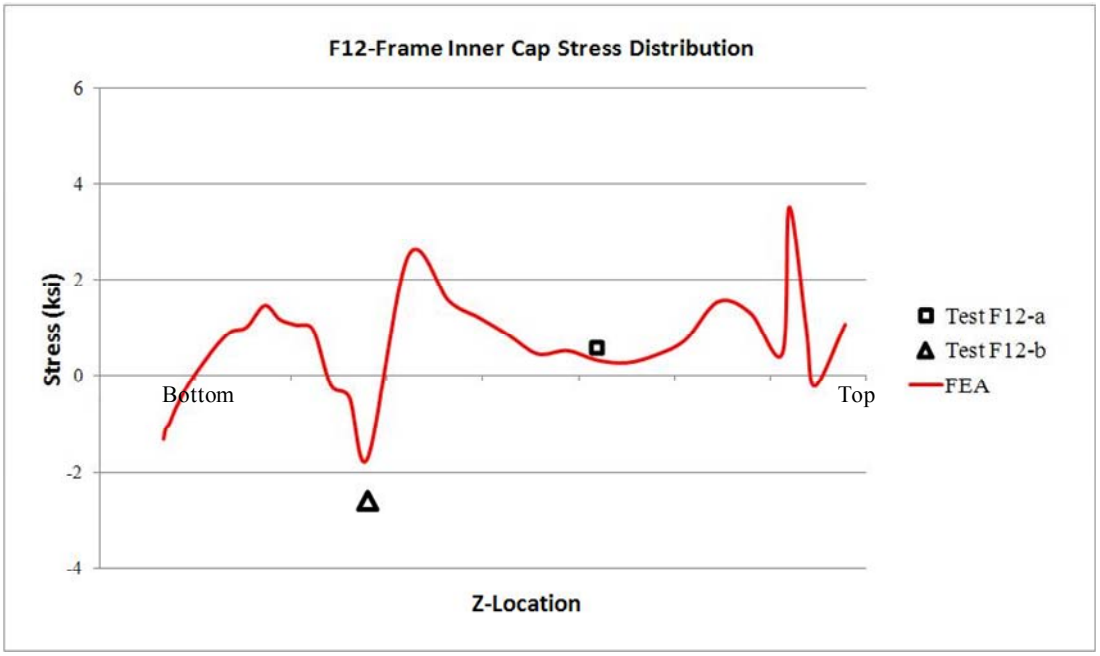

Figure 4.4.9: F12-Frame inner cap stress distribution with test results

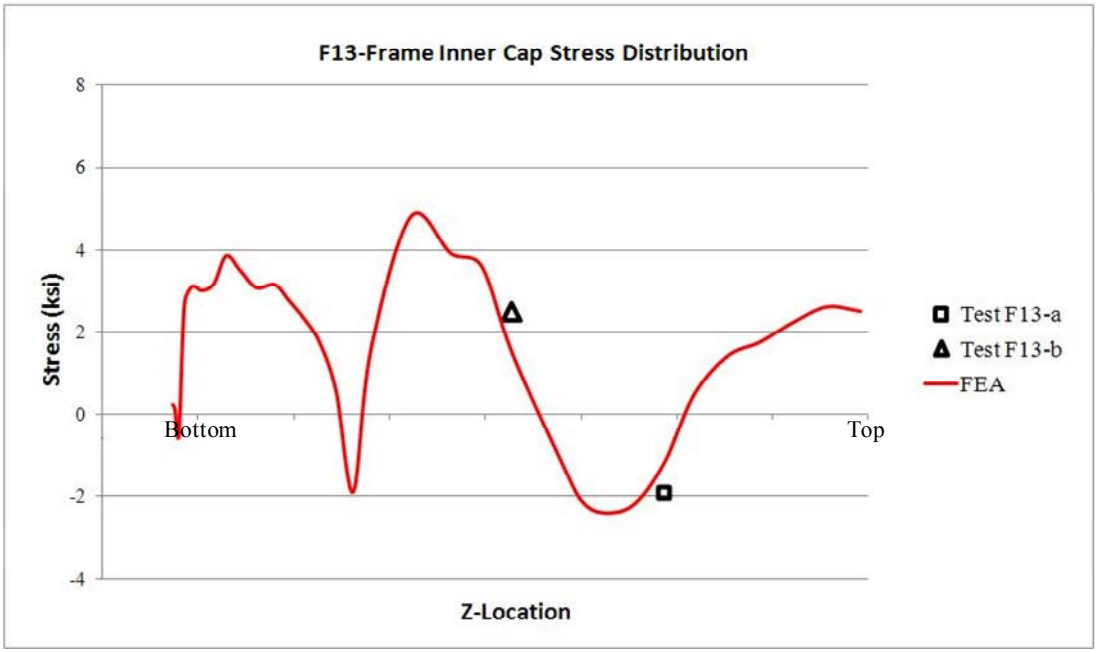

Figure 4.4.10: F13-Frame inner cap stress distribution with test results

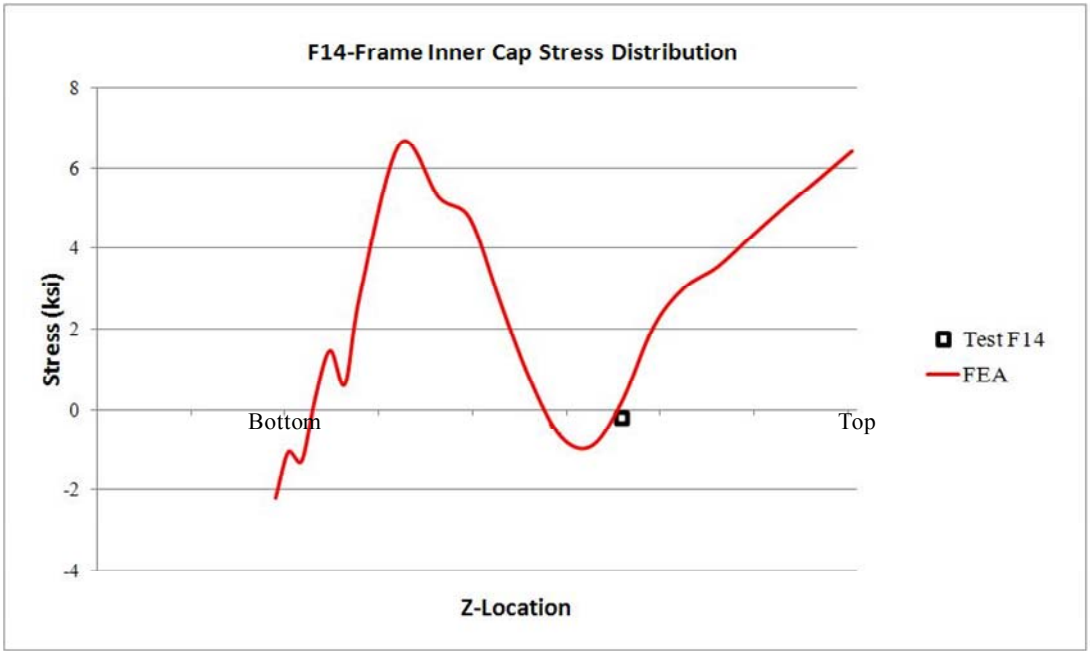

Figure 4.4.11: F14-Frame inner cap stress distribution with test results

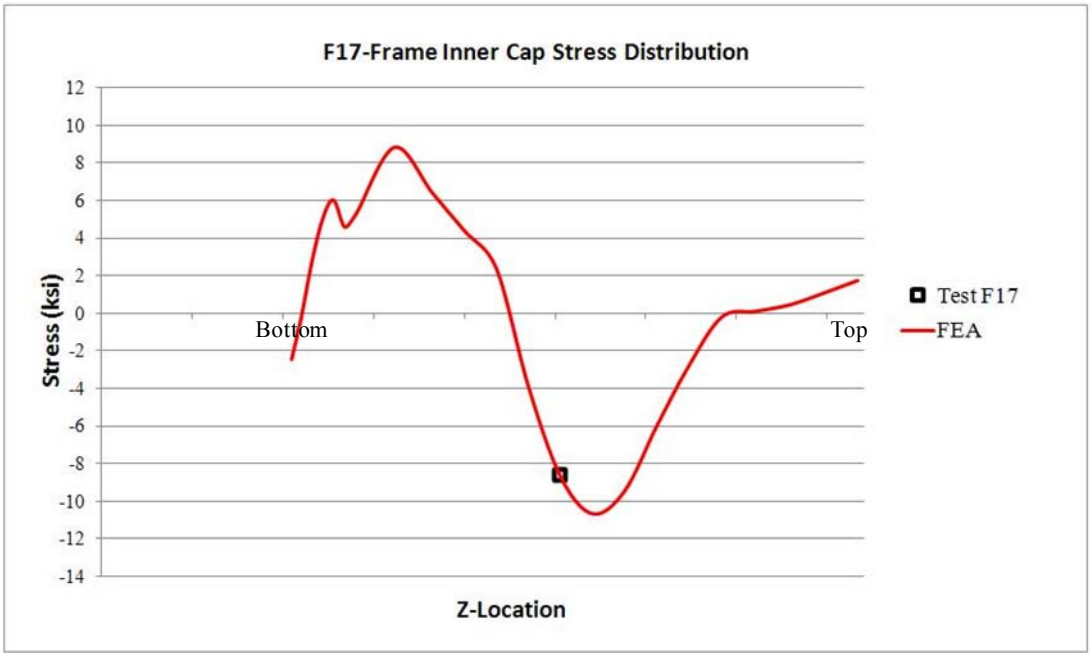

Figure 4.4.12: F17-Frame inner cap stress distribution with test results

When frame inner cap stress results are inspected, at the first glance, satisfactory correlation between FEA and test results can be observed for the F2, F3, F5, F6, F12, F13 and F17 frame stations. For the frame F4, gauge at station F4-a is below the gauge resolution level in the test and gauge at station F4-b result shows linear variation under increasing cabin pressure. In FEA, the stress level for the gauge at station F4-a is higher than that of in the tests as in the case of the longeron inner flange gauges that have strains below the gauge resolution. On the other hand, station F4-b result shows a good correlation with test result on the same frame. As gauge at station F4-b does, the gauge on the F14 frame also has strains that are below the gauge resolution in the test. The FEA result for this gauge shows very low stress level as expected and mentioned in Chapter 3. From Figure 4.4.4 to Figure 4.4.12, it can be concluded that all of the tested points located at the frame inner caps capture the stress trends obtained from the FEA except gauge located at station F4-a.

As it is observed from the Table 4.4.1, the correlation is satisfied between the test and the FEA stress results of the SG points at the skin, bulkhead upper caps, tie bars and the sheet support.

4.5 Actions taken to Update the FEM

According to the checks for the correlation, it is concluded that, the differences between the FEA and test results are mainly due to the lateral support structures. The deformations of the longerons and the frames are highly affected from these supports. When the FEA results for the longerons are inspected, it can be said that, longerons deform more in FEA more than they deform during the tests. In order to achieve a better correlation, actions are taken to update the lateral support structures of the cockpit.

Updating of the Sheet Support

The sheet support is modelled without its cut-outs in the FEM due to the simplification reasons. The update for the structure is done by modelling these cut-outs as well. The reason to take this action is such that the amount of material reduced from the support is at serious levels when compared to the existing size of the structure. Also, the stress level on the sheet support is higher in FEA than the ones in test results and it may possibly affect the results of the F2 frame. Therefore, when lateral stiffness is taken into account, modelling the cut-outs becomes worthy. The detailed FEM of the original and updated sheet supports are shown in Figure 4.5.2 and Figure 4.5.2 respectively.

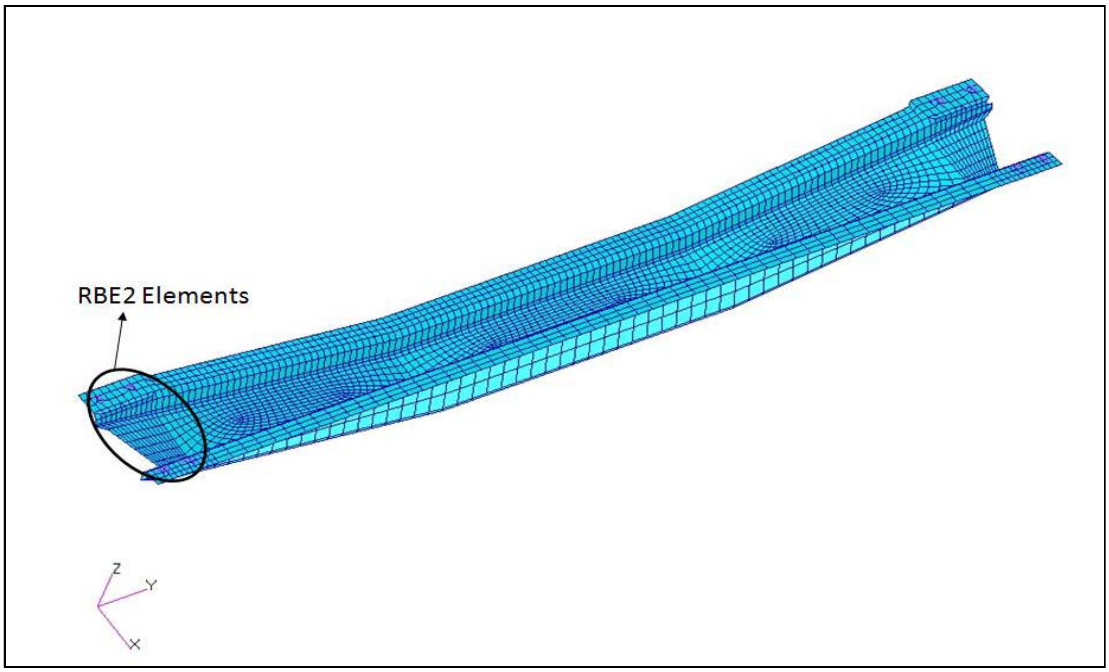

Figure 4.5.1: Detailed FEM of the original sheet support-a

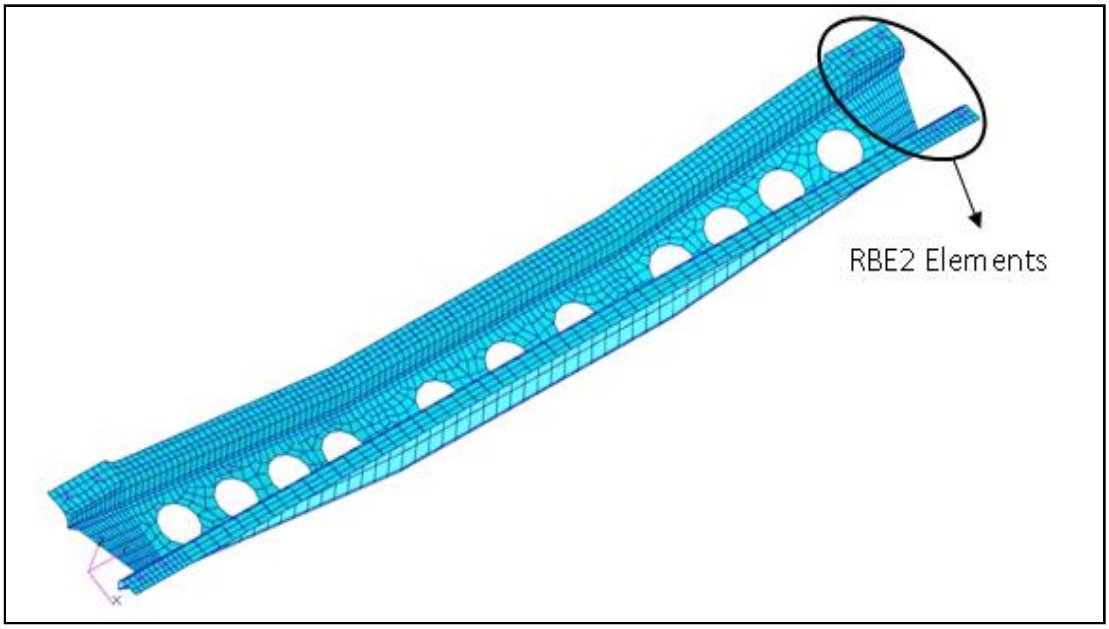

Figure 4.5.2: Detailed FEM of the updated sheet support-b

Updating of the Tie Bars

Tie bars are fully modelled with CBEAM elements and at the connection locations to the frames and therefore rigid type elements are not used. Although the correlation checks show that this type of simplification gives reasonable results, side sections of the tie bars are updated due to its connection region with frames. The actual plate form of the side sections is simulated with CQUAD4 elements and connection to the frames are satisfied with RBE2 elements by setting three rotational DOF as free. The aim is to expand the area of the connection and to get better stress results from the frames F3 and F12. It is thought that, expanding the connection area and assigning free rotational DOF for the connections, results are provided better in bending deformation variation for the frames. At the intersection point of the main bar section with the side section, RBE2 type element is used. All the six translational and rotational DOF's are constrained at the connection points. In real structure, at the transition region, there is a radius and this radius transmits bending loads between the main and the side sections. In FEM of the tie bar, simulation of this effect with lonely common grid point of the bar and the plate element is impossible. In order to provide the rigidity of the model for the static analysis, RBE2 type elements are used in these regions. The detailed FEM of the original front and rear tie bars and their updated versions are shown from Figure 4.5.3 to Figure 4.5.6.

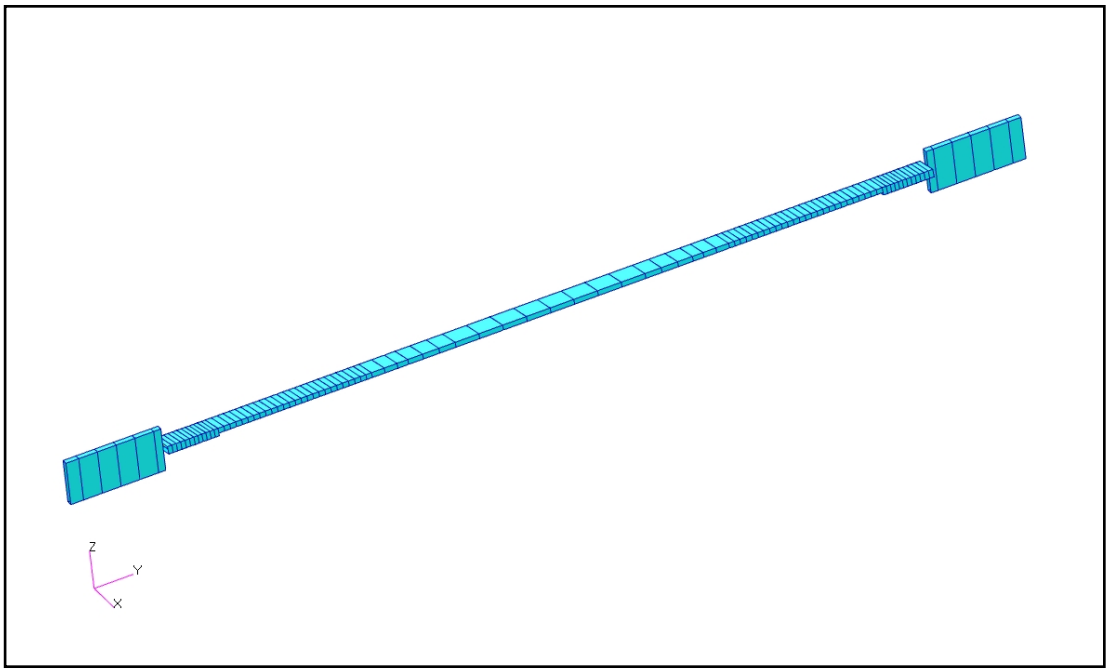

Figure 4.5.3: Detailed FEM of the front tie bar-a

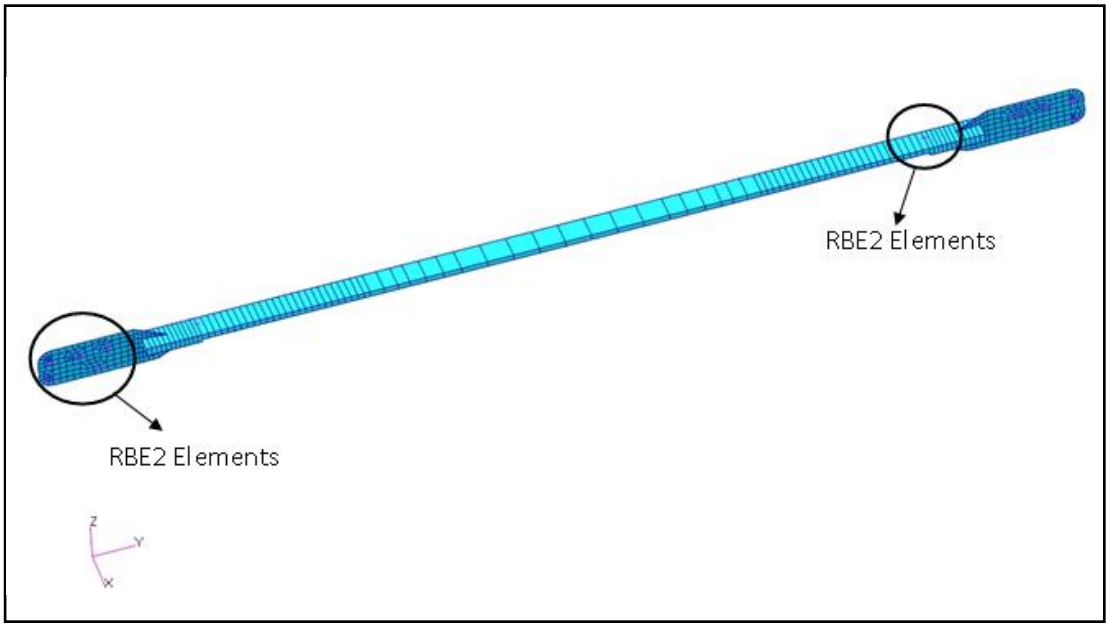

Figure 4.5.4: Detailed FEM of the updated front tie bar-b

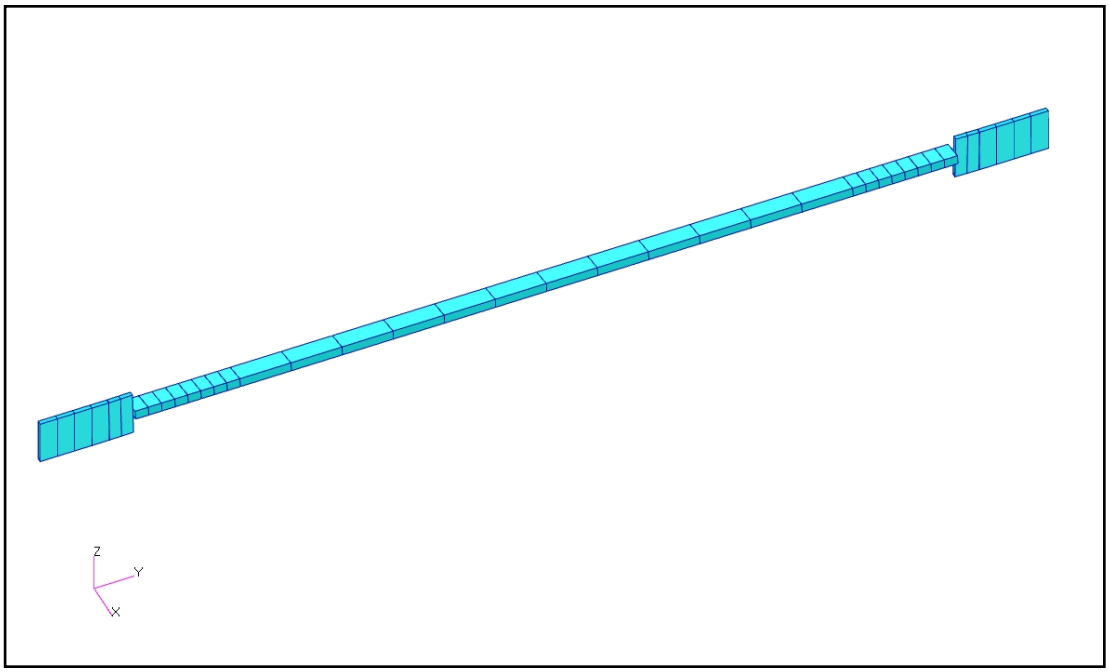

Figure 4.5.5: Detailed FEM of the rear tie bar-a

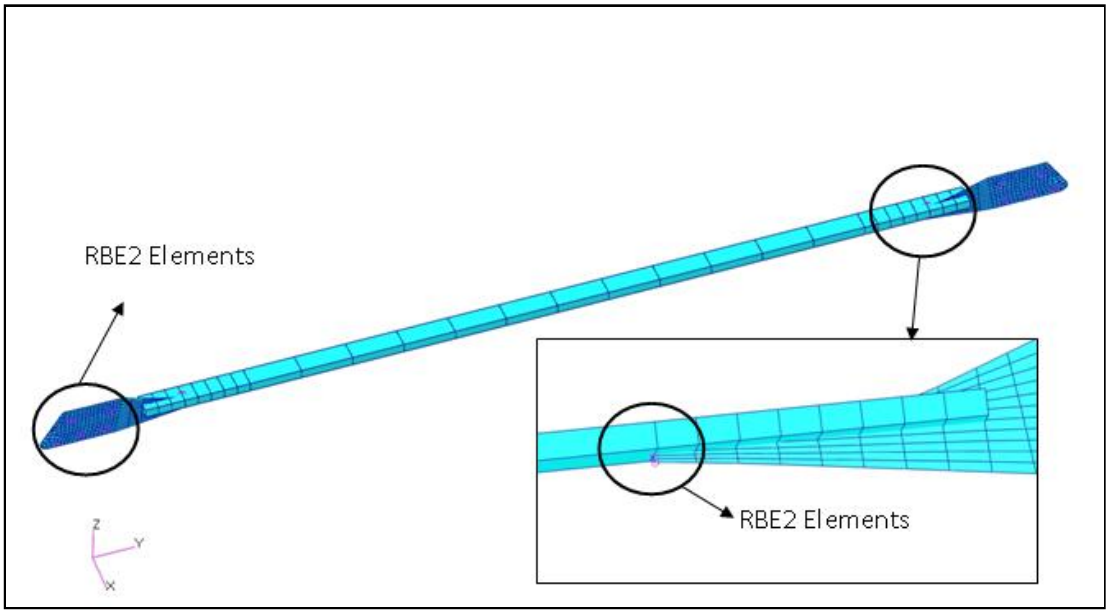

Figure 4.5.6: Detailed FEM of the updated rear tie bar-b

Canopy Support Fittings & Canopy Drive Shaft

Canopy support fittings and canopy drive shaft are not modelled at the beginning of the study. It was thought that modelling these structures does not have a very large impact on the load path of the cockpit under cabin pressure. The modelling of the fittings also brings an additional run time to the FEM during the analysis stage. However, during the checks performed for the correlation, it is understood that, deformations of the longerons are not in expected levels. In order to get less longeron deformation results from the FEA, these structures are also modelled.

Canopy support fitting is a complex-shaped structure which supports mainly the drive shaft mechanism of the canopy. It also carries portion of upper longeron side loads under cabin pressure. It locates between frames F9 and F10 in the cockpit. This fitting is connected to the upper longeron inner flange, bulkhead web and bulkhead upper cap. Thus, it works all in lateral, longitudinal and vertical directions. Such a complex geometry has lots of fillets, flanges and radiuses. Therefore, canopy support fittings are modelled with CTETRA type solid elements. At the connection points, only three translational DOF is constrained with the help of RBE2 type elements. The rotational constraints are released for all of the connections, especially for bulkhead upper cap connection. At this location there is only one fastener and in real life, the fastener can rotate around its axis. Between the canopy support fittings, there is a canopy drive shaft. Shaft is connected to the bushings of the fittings. Between the drive shaft and the bushings, there is a relative motion, and this connection should be modelled with contact type elements for the static analysis. However, contact-type element having non-linear feature is a computationally expensive one. Therefore, instead of using contact type elements, shaft-fitting connection is provided by using RBE2 type elements. The rotational and translational DOF's of the shaft in its axis are assigned as free. Thus, shaft is allowed to rotate around its axis and lateral stiffness of the shaft is not added into the model. The detailed FEM of the canopy support fittings and the canopy drive shaft are shown in Figure 4.5.7 and Figure 4.5.8 respectively.

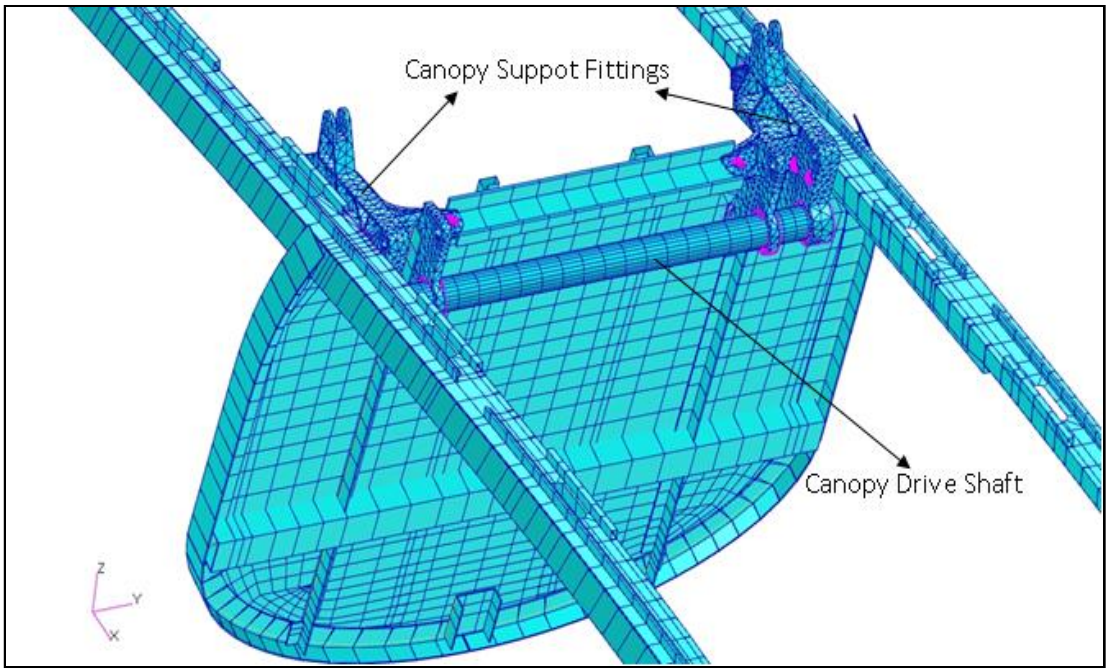

Figure 4.5.7: Detailed FEM of the canopy support fittings and the drive shaft

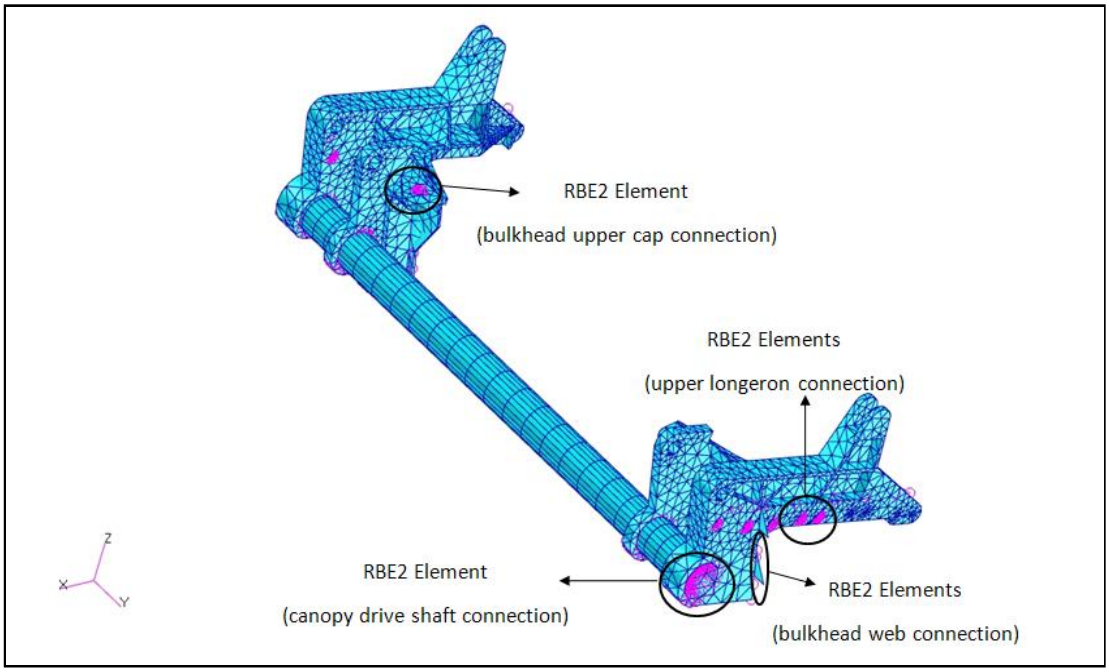

Figure 4.5.8: Connections of the canopy support fittings and the drive shaft

4.6 Updated Results

The comparison between the updated FEM (U_FEM) stress results with test results are tabulated in Table 4.6.3.

Table 4.6.1: The comparison between test and updated FEM results

Longeron Web	Stress (ksi)	Stress (ksi)	Longeron inner flange	Stress (ksi)	Stress (ksi)	Longeron outer flange	Stress (ksi)	Stress (ksi)
Location	TEST	U_FEM	Location	TEST	U_FEM	Location	TEST	U_FEM
B1	2.8	2.6	F4	0.1	-0.2	F4	0.9	0.5
F1	3.0	2.5	F6	-4.7	-5.1	F9	1.3	0.9
F2	2.6	2.7	F14	0.0	-0.6	F12	-0.8	-0.1
F20	1.8	1.5	F15	-3.4	-3.5	F13	2.9	3.0
			F18	-1.4	0.7			
Frame Inner Cap	Stress (ksi)	Stress (ksi)	Skin	Stress Max. Principal (ksi)	Stress Max. Principal (ksi)	Bulkhead Upper Cap	Stress (ksi)	Stress (ksi)
Location	TEST	U_FEM	Location	TEST	U_FEM	Location	TEST	U_FEM
F2-a	2.0	2.5	F4	3.1	3.3	B2	3.3	3.0
F2-b	0.8	1.1	F13	3.7	4.0	B3	1.6	1.4
F3-a	2.6	3.0	F16	5.4	5.0			
F3-b	2.6	2.4						
F4-a	-0.3	0.5	Tie Bars	Stress (ksi)	Stress (ksi)	Sheet Support	Stress (ksi)	Stress (ksi)
F4-b	3.9	4.0	Location	TEST	U_FEM	Location	TEST	U_FEM
F5-a	4.2	4.5	F3	9.2	9.1	F1	9.8	9.6
F5-b	6.4	6.0	F12	7.8	7.9			
F6-a	5.5	5.6						
F6-b	3.3	2.9						
F12-a	0.6	0.4						
F12-b	-2.6	-2.2						
F13-a	-1.9	-1.4						
F13-b	2.5	1.9						
F14	-0.2	0.2						
F17	-8.6	-8.5						

U_FEM : Updated FEM

As it is observed from Table 4.6.1 that, the gauges which are below the gauge resolution in the test (coloured in yellow), updated FEA results are closer to the test results than the results obtained from original FEA. Although still there are sign differences for these gauges, stress levels are very close to the zero stress level. Also updated results for longeron outer flange locations at F9 and F12 are better in sign

and in magnitude when compared with the results in original results. It is also observed that, the stress level for longeron inner flange location at F18 does not change much after updates. The percentages of difference between test and updated FEM results are given in Table 4.6.2.

Table 4.6.2: The percentage of difference between test and updated FEM results

Longeron Web	Difference (%)	Longeron inner flange	Difference (%)	Longeron outer flange	Difference (%)
Location	TEST-U_FEM	Location	TEST-U_FEM	Location	TEST-U_FEM
B1	-6	F4	-319	F4	-43
F1	-18	F6	9	F9	-32
F2	4	F14	2831	F12	-88
F20	-13	F15	3	F13	3
		F18	-152		
Frame Inner Cap	Difference (%)	Skin	Difference (%)	Bulkhead Upper Cap	Difference (%)
Location	TEST-U_FEM	Location	TEST-U_FEM	Location	TEST-U_FEM
F2-a	22	F4	6	B2	-10
F2-b	48	F13	9	B3	-13
F3-a	14	F16	-8		
F3-b	-8				
F4-a	-267	Tie Bars	Difference (%)	Sheet Support	Difference (%)
F4-b	1	Location	TEST-U_FEM	Location	TEST-U_FEM
F5-a	8	F3	-1	F1	-2
F5-b	-6	F12	2		
F6-a	2				
F6-b	-13				
F12-a	-29				
F12-b	-15				
F13-a	-25				
F13-b	-23				
F14	-184				
F17	-1				

As stated before in section 4.4, the percentage errors between the results given in Table 4.6.2 are also unrealistic due to the low stress levels. The comparison of the updated FEM (U_FEM) stress results with original FEM (O_FEM) and test results are tabulated in Table 4.6.3.

Table 4.6.3: The comparison between updated FEM, original FEM and test results

Longeron Web	Stress (ksi)	Stress (ksi)	Stress (ksi)
Location	TEST	O_FEM	U_FEM
B1	2.8	2.7	2.6
F1	3.0	2.6	2.5
F2	2.6	2.8	2.7
F20	1.8	1.5	1.5

Longeron inner flange	Stress (ksi)	Stress (ksi)	Stress (ksi)
Location	TEST	O_FEM	U_FEM
F4	0.1	-2.3	-0.2
F6	-4.7	-6.4	-5.1
F14	0.0	-1.8	-0.6
F15	-3.4	-3.7	-3.5
F18	-1.4	0.6	0.7

Longeron outer flange	Stress (ksi)	Stress (ksi)	Stress (ksi)
Location	TEST	O_FEM	U_FEM
F4	0.9	1.8	0.5
F9	1.3	-0.5	0.9
F12	-0.8	2.3	-0.1
F13	2.9	4.9	3.0

Skin	Stress Max. Principal (ksi)	Stress Max. Principal (ksi)	Stress Max. Principal (ksi)
Location	TEST	O_FEM	U_FEM
F4	3.1	3.4	3.3
F13	3.7	4.1	4.0
F16	5.4	5.0	5.0

Frame Inner Cap	Stress (ksi)	Stress (ksi)	Stress (ksi)
Location	TEST	O_FEM	U_FEM
F2-a	2.0	2.9	2.5
F2-b	0.8	1.5	1.1
F3-a	2.6	3.4	3.0
F3-b	2.6	2.3	2.4
F4-a	-0.3	4.7	0.5
F4-b	3.9	3.9	4.0
F5-a	4.2	4.7	4.5
F5-b	6.4	6.0	6.0
F6-a	5.5	5.4	5.6
F6-b	3.3	3.0	2.9
F12-a	0.6	0.3	0.4
F12-b	-2.6	-1.7	-2.2
F13-a	-1.9	-1.2	-1.4
F13-b	2.5	1.5	1.9
F14	-0.2	0.2	0.2
F17	-8.6	-8.5	-8.5

Bulkhead Upper Cap	Stress (ksi)	Stress (ksi)	Stress (ksi)
Location	TEST	O_FEM	U_FEM
B2	3.3	2.8	3.0
B3	1.6	1.4	1.4

Sheet Support	Stress (ksi)	Stress (ksi)	Stress (ksi)
Location	TEST	O_FEM	U_FEM
F1	9.8	10.2	9.6

Tie Bars	Stress (ksi)	Stress (ksi)	Stress (ksi)
Location	TEST	O_FEM	U_FEM
F3	9.2	9.6	9.1
F12	7.8	8.4	7.9

O_FEM : Original FEM
U_FEM : Updated FEM

When Table 4.6.3 is inspected, it is seen that longeron web results are not affected too much from the updates. The only expected effect that may come from the sheet support update does not even affect the results much. It is interpreted that sheet support stiffness does not change load distribution of the longeron web, which is actually supported by longeron inner and outer flanges. It can be concluded from these results obtained for the longeron web that a considerable correlation is satisfied between the test and the updated FEM stress results.

The updated FEM results for the longeron inner flange show a better correlation with test when compared with the original FEM results. For the stations F4 and F14 which has lower strain values than the gauge resolution during the tests, stress results are too low as expected but it is not the case in original FEM. Additionally, stress result of station F6 shows a better correlation. The results at the stations F15 and F18 on the longeron inner flange are not affected from the updates. It is because of the update locations which are mainly at the stations F1, F3, F9, F10 and F12 stations in the cockpit. After station F15, results do not change much due to this particular reason. The updated longeron inner flange stress distribution through the longitudinal direction of the cockpit (X-direction) is shown with the test and original FEM results in Figure 4.6.1.

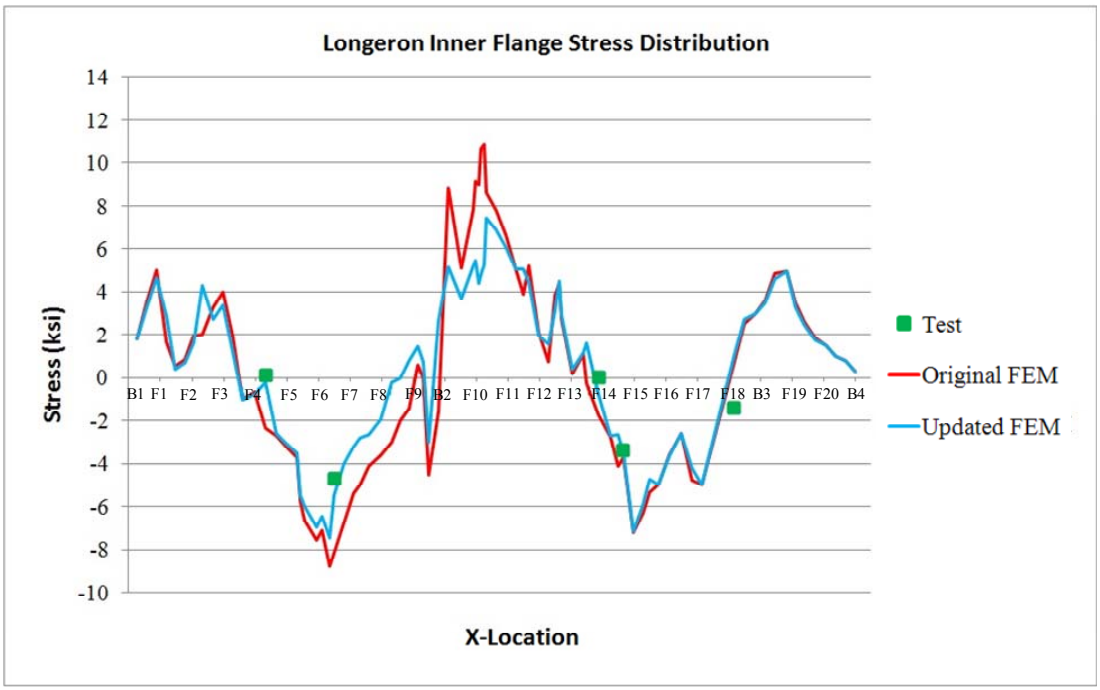

Figure 4.6.1: Updated longeron inner flange stress distribution

It can easily be seen from the Table 4.6.3 that the updated FEM results for the longeron outer flange is much better than results obtained from the original FEM. The stress results at the locations of F4, F9, F12 and F13 on the longeron outer flange are affected in considerable levels from the updates at the locations of F3, F9, F10 and F12. It can be concluded for the longeron outer flange that a considerable correlation is satisfied between the test and the updated FEM stress results. The updated longeron outer flange stress distribution through the longitudinal direction of the cockpit (X-direction) is shown with the test and original FEM results in Figure 4.6.2.

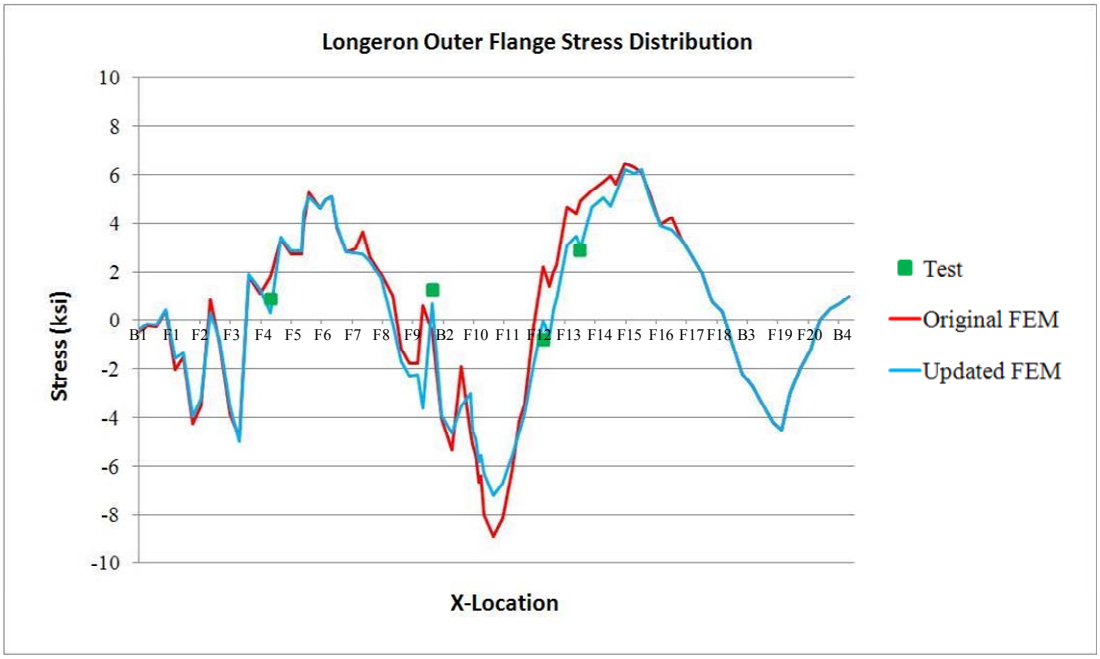

Figure 4.6.2: Updated longeron outer flange stress distribution

When Table 4.6.3 is inspected for the frame inner cap updated results, it can be said that updated sheet support provides better correlation for the frame F2. Updated frame F-2 inner cap stress variation through the height of the frame is also plotted in Figure 4.6.3 with the test and original FEM results for comparison purposes.

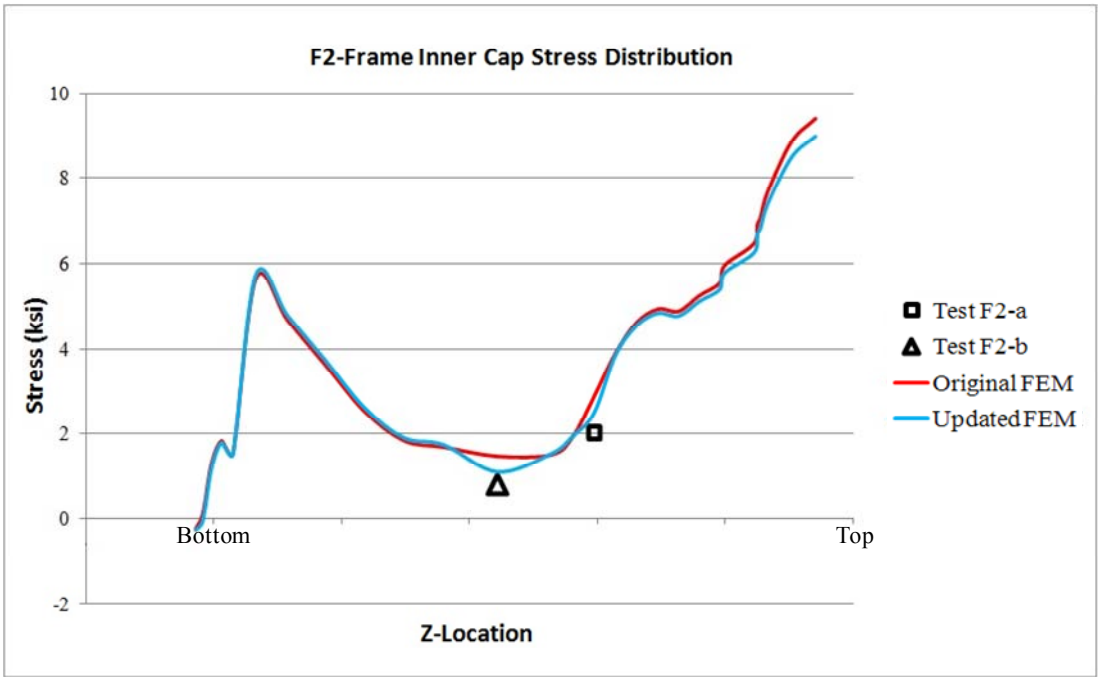

Figure 4.6.3: Updated F2-Frame inner cap stress distribution

As it is observed in Table 4.6.3, updated front tie bar located at frame F3 provides better correlation for the frame F3. Updating the front tie bar also changes the bending deformation at the top of the frame F3 where it is located near the upper longeron. Updated frame F-3 inner cap stress variation through the height of the frame is also plotted with the test and original FEM results in Figure 4.6.4.

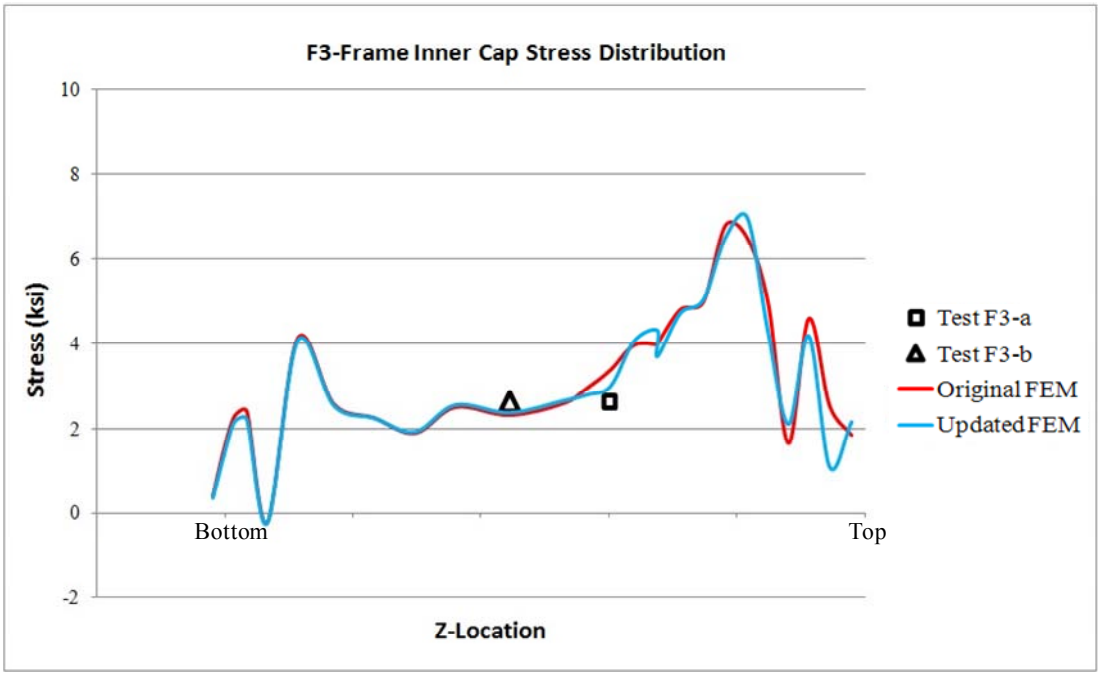

Figure 4.6.4: Updated F3-Frame inner cap stress distribution

The stress result for the point at station F4-a, which shows lower strain value than the gauge resolution during the tests, turns out to be too low after the updates as expected. It can be seen from Table 4.6.3 regarding the frames F5 and F6 that updates do not affect the original results much. Updated frames F4, F5 and F6 inner cap stress variations through the height of the frames are plotted with the test and original FEM results from Figure 4.6.5 to Figure 4.6.7 respectively.

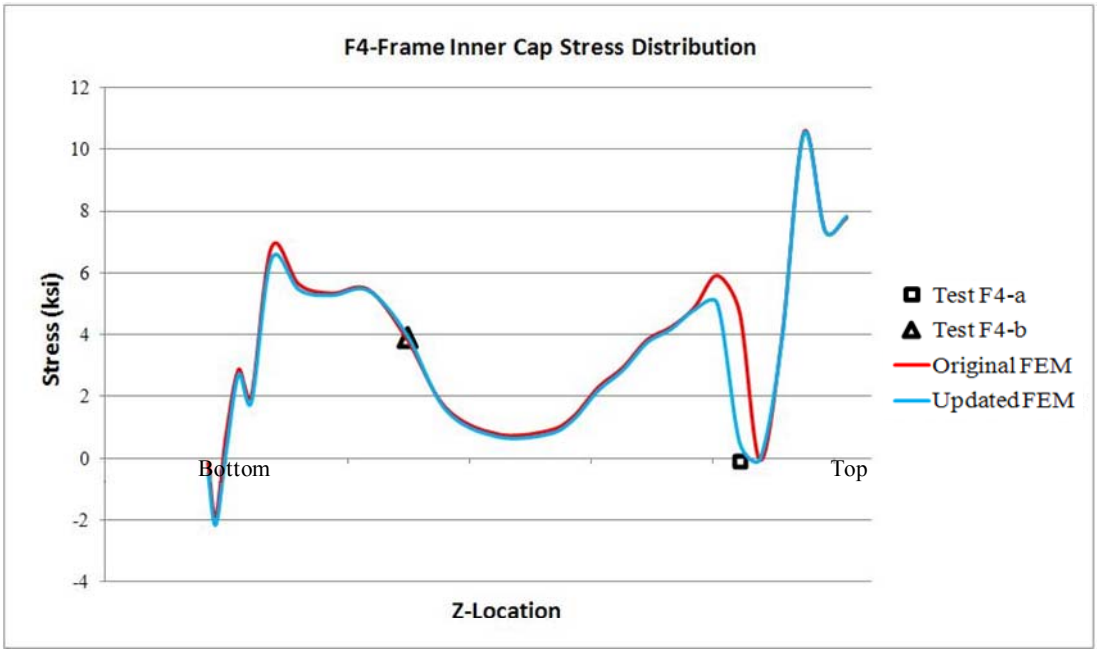

Figure 4.6.5: Updated F4-Frame inner cap stress distribution

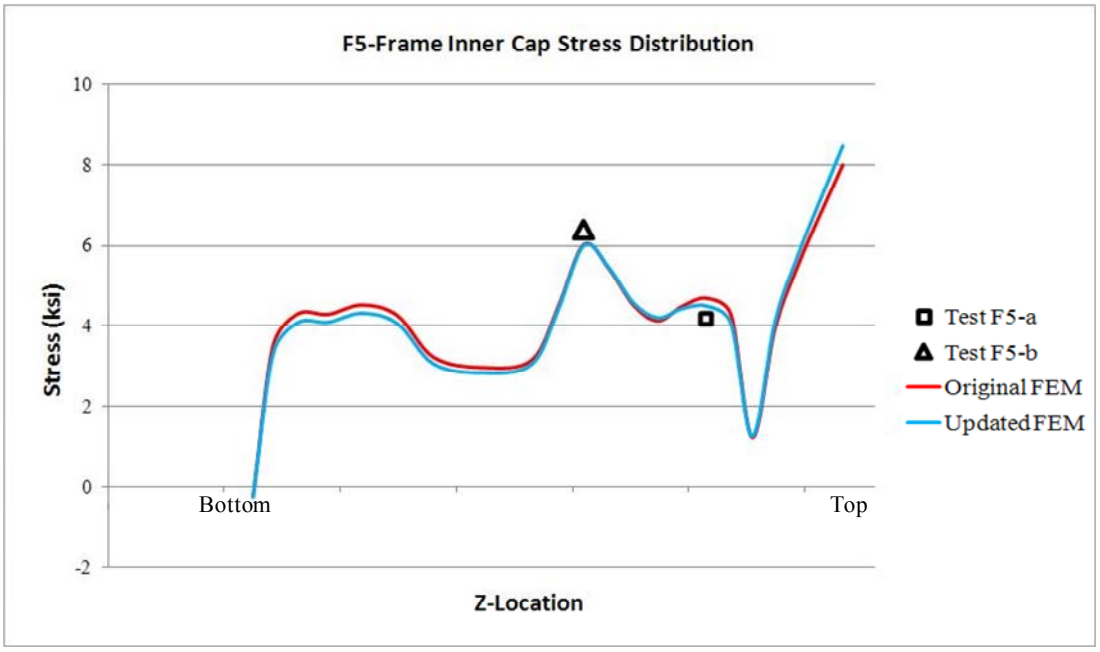

Figure 4.6.6: Updated F5-Frame inner cap stress distribution

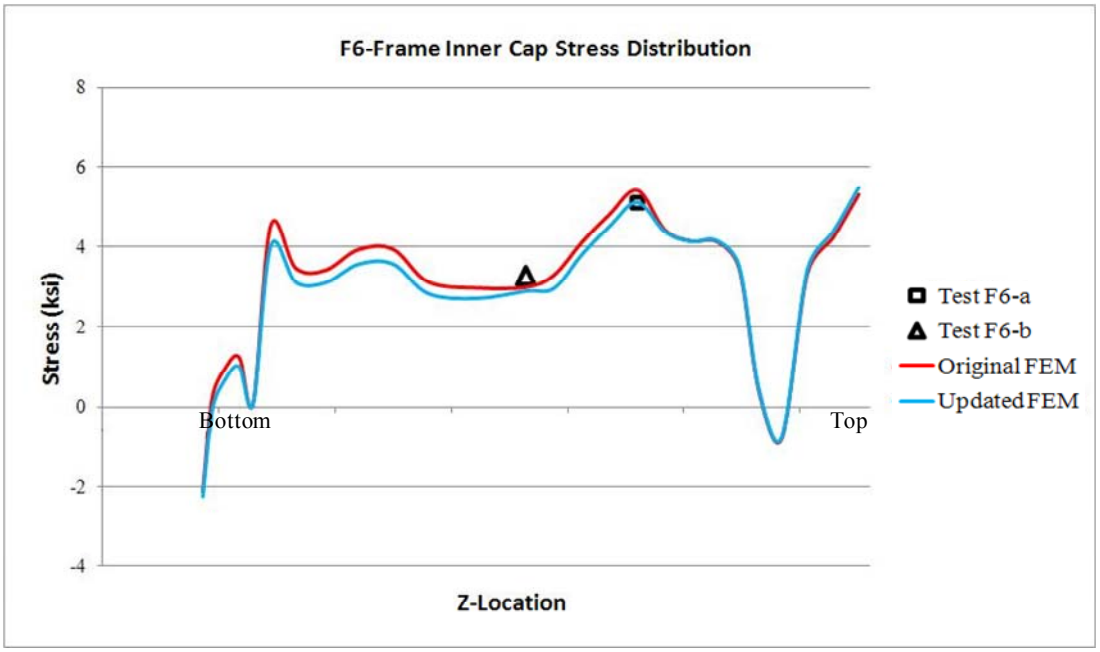

Figure 4.6.7: Updated F6-Frame inner cap stress distribution

The updated rear tie bar located at F12 provides better correlation for F12 frame. Updating the rear tie bar also changes the bending deformation at the top of the frame F12 as it is the case for the front tie bar. For frame F13, updated results show better correlation with the test results than the original FEM ones. A huge differences in stress variations are observed at the top of the frame F13. For the F14 and F17 frames, updates do not affect the original FEM results. Updated F-12, F13, F14 an F17 frames inner cap stress variations through the height of the frames is plotted with the test and original FEM results from Figure 4.6.8 and Figure 4.6.11 respectively for comparison purposes.

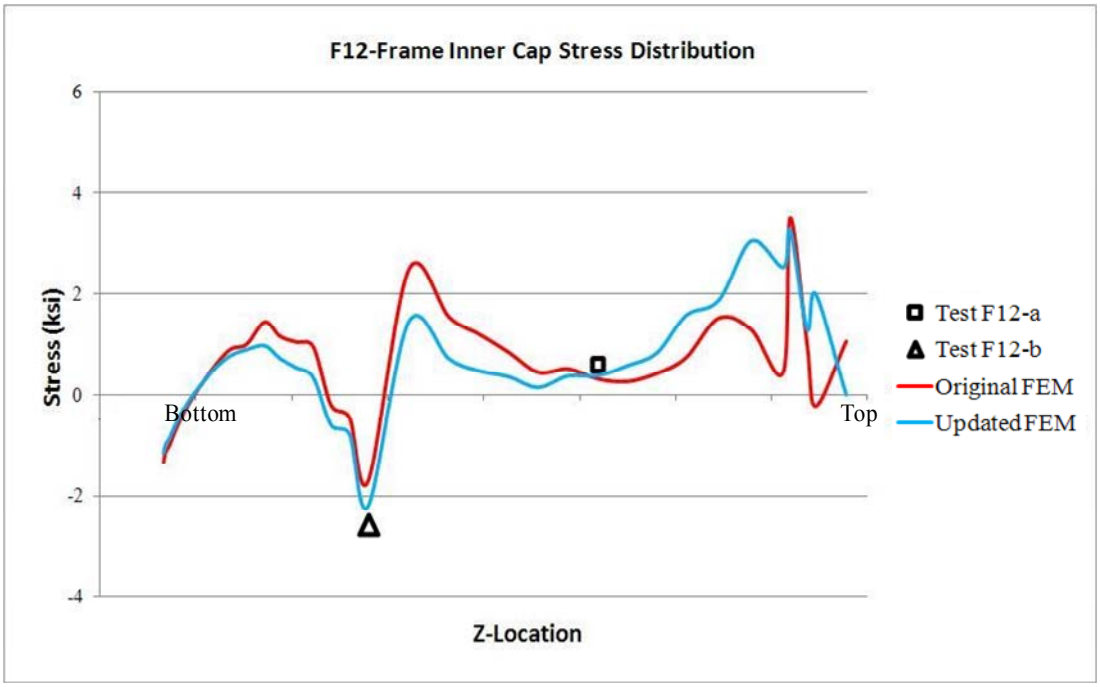

Figure 4.6.8: Updated F12-Frame inner cap stress distribution

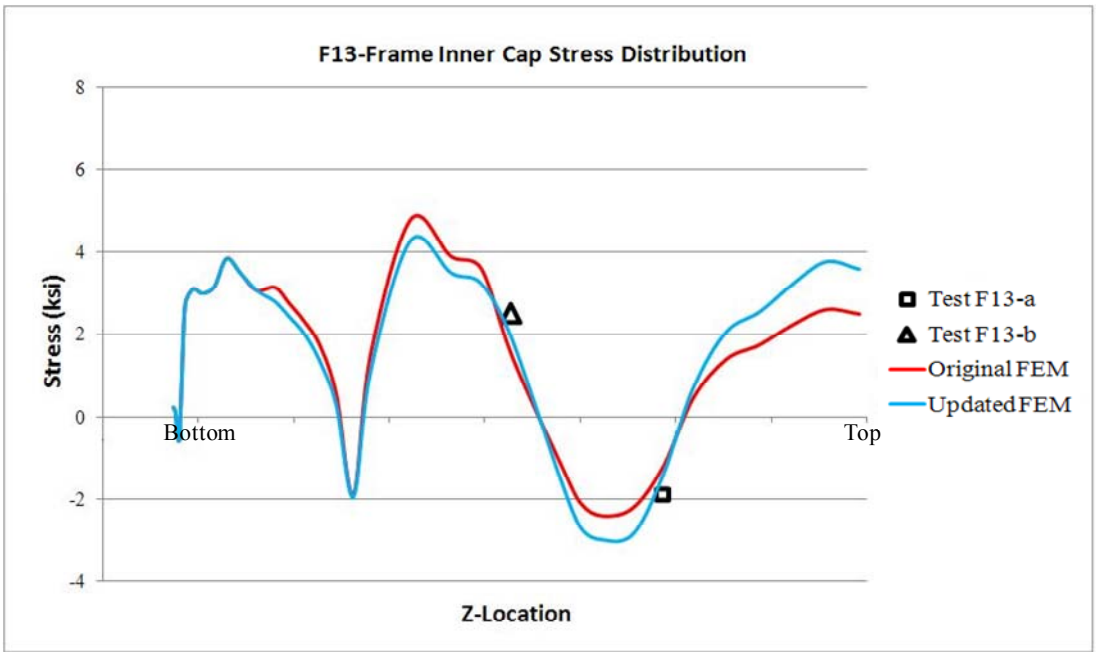

Figure 4.6.9: Updated F13-Frame inner cap stress distribution

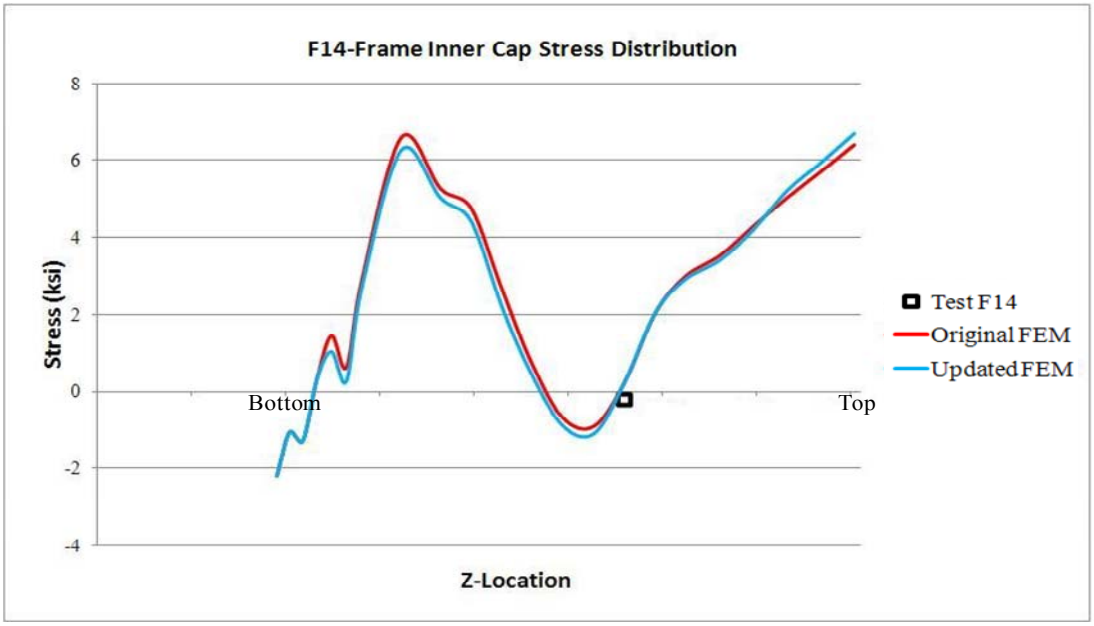

Figure 4.6.10: Updated F14-Frame inner cap stress distribution

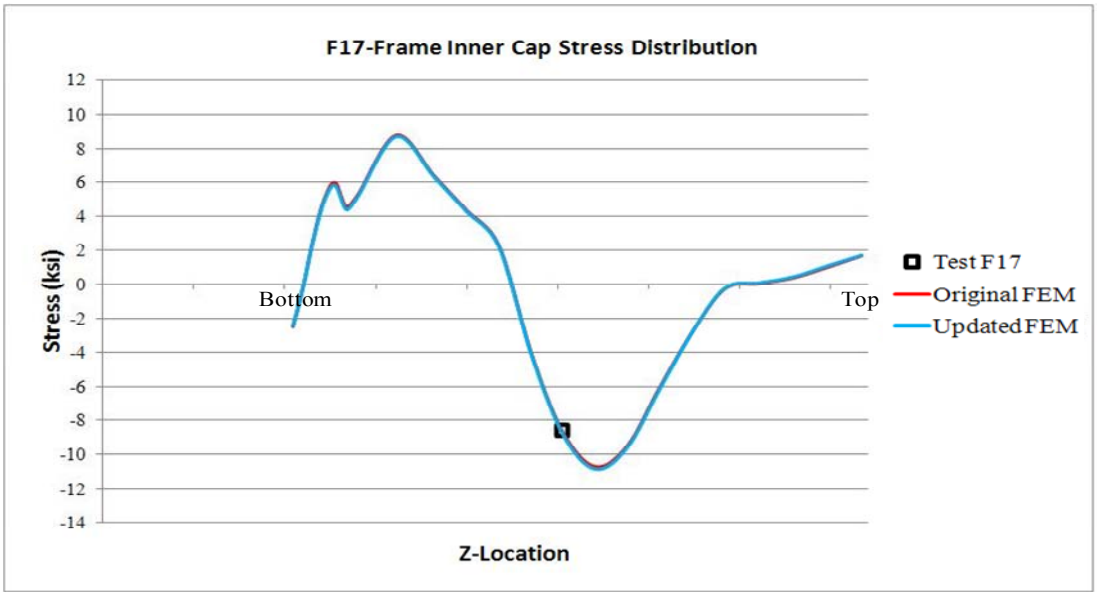

Figure 4.6.11: Updated F17-Frame inner cap stress distribution

As it can be seen from the Table 4.6.3, while updates do not affect the results for the skin and bulkhead upper caps much, better correlation is obtained on the tie bars and the sheet support results after the updates performed for these structures.

4.7 Summary

In this section, after confirmations made for the reliability of the FEA, the methodologies defined in order to gather the results are presented. Then, the comparisons between FEA and test results are made and correlations are checked. In order to get better correlation, some actions for updating the FEM are performed and updated results are re-checked to observe the improvements in the correlation. For the longeron webs, a good correlation is satisfied with the original FEM and thus updates do not affect the results much. However, for the longeron inner and outer flanges, updates affect the results in considerable levels and better correlation is achieved in comparison with the test results. Because of the update locations, results do not change in considerable levels from frame F15 through the rear end of the cockpit. All of the tested points located at the frame inner caps capture the stress trends obtained from the original FEM except at F4-a location. After performing further updates, FEA results show better correlation with the test results and expected results for F4-a location are also obtained. For the frames F3, F12 and F13, stress variation through the height of the frames change in significant levels after the updates performed for the tie bars. After updating, the results for skin and bulkhead upper cap do not change much and for the tie bars and sheet support, better correlation is obtained.

CHAPTER 5

CONCLUSION

5.1 General Conclusions

The main aim of this study is to validate a detailed FEM of the jet trainer cockpit structure with ground pressurisation test results. For this purpose, first the load carrying/transfer mechanism of the cockpit structure is investigated. During this process, assumptions for the FE modelling are made such that to ensure the necessary and sufficient conditions for the correlation study. The assumptions reflect mainly the Global FEM logic. According to these assumptions, the FEM of the cockpit structure is constructed by using commercial finite element software MSC/PATRAN® and MSC/NASTRAN®. After the checks performed for the obtained FEM (i.e. the original FEM), loads and boundary conditions are assigned to the model and linear static FEA is performed.

In order to validate the FEM, cockpit is pressurised on the ground. In the scope of the test procedure, the criteria for the selection of the sensors used for the test, their installations and numbering procedures are presented. After performing the tests, the obtained strain results are then interpreted on the basis of their linear or non-linear responses under the linearly increasing cabin pressure. The installation checks are also made for the strain gauges which show non-linear behaviour. After the confirmation for the installations, it is concluded that their strain values are too low

in comparison to the gauges having linear responses. It is thought that the strain gauges may not response to the low strain values properly and then, in order to make a physical comparison with FEA, the obtained strain results are converted to their corresponding stress values.

For the correlation study performed between FEM and the test results, first, the response of the structures under cabin pressure is checked. Having obtained reasonable deformation results, methodologies to gather the stresses from the FEA results are explained. This part of the study is as important as the modelling techniques applied for the FEM as the commercial finite element software, NASTRAN®, extracts and offers different types of stress values after the analysis performed and therefore, in order to make true comparison with the test results, the methodology chosen by the engineer in gathering the FEA results is vital.

The results obtained from the FEA are compared with the test results and checks are made for the correlation. At the first run of the model, the obtained stress results are in reasonable levels for most of the points measured during the test. Moreover, the differences in stress levels are too low when compared with the material yield stress limit. However, especially for the longeron inner and outer flanges and for some of the frames, a need arises for the refinement of the stress results to achieve a better correlation. For this reason, some actions are taken to update the original FEM. The updates are performed for some of the lateral structures in the cockpit. After this second run of the model, the results obtained from the FEA are re-checked for the correlation purposes. The desirable stress values are then obtained for all of the points measured in the test and FEM is finalised after achieving a good correlation between the FEA and the test results. This final form of the FEM (i.e. updated FEM) of the cockpit structure is now ready to serve as a benchmark for any future modification and/or correlation studies by also proving itself a very reliable one.

5.2 Recommendations for the Future Work

This structural analysis study can also be performed by considering the damage tolerance issues regarding the aging of the aircraft.

The fasteners can be modelled with their elastic properties at the desired primary structure connections. This application can be performed in order to get knowledge of the refined stresses for further fatigue analyses and/or for the repairing purposes to be performed at specific locations.

The obtained updated model can be correlated with flight tests under some specific load case; such as pull-up manoeuvre combined with cabin pressure as in the case of flight above 8000 [ft]. For this purpose, canopies and the windshield with its close shape should be modelled to transfer the aerodynamic loads to the cockpit. It may also require modelling of the centre fuselage in order to simulate boundary condition effects at the end of the rear cockpit in a better way. In addition to the model updates, also temperature compensation should be used during the flight tests.

The experiments can be performed by changing the locations of the strain gauges and locating them over the structure where they provide higher strains.

REFERENCES

[1] Northrop Grumman Corporation, http://www.as.northropgrumman.com/products/t38talon/index.html, last visited on November 18th, 2011.

[2] NASA Dryden Flight Research Center Photo Gallery, http://www.dfrc.nasa.gov/Gallery/Photo/T-38/Large/ED06-0072-8.jpg, last visited on November 18th, 2011.

[3] Wikipedia The Free Encyclopedia, http://en.wikipedia.org/wiki/Dassault/Dornier_Alpha_Jet, last visited on November 18th, 2011.

[4] BAE Systems Company, http://www.baesystems.com/ProductsServices/bae_prod_air_hawk.html, last visited on November 18th, 2011.

[5] U.S. Department of Transportation Federal Aviation Administration, *Airframe and Powerplant Mechanics Airframe Handbook*, 1972.

[6] Yusuf, K., Nukman, Y., Dawal, S. Z., Chandra D., Sofia, N. (2010, April). Conceptual Design of Fuselage Structure of Very Light Jet Aircraft, *Latest Trends on Theoretical and Applied Mechanics, Fluid Mechanics and Heat & Mass Transfer.*

[7] Megson, T.H.G. (2007). Aircraft Structures. UK: Elsevier Aerospace Engineering Series.

[8] Aircraft Design: Synthesis and Analysis Textbook, Stanford University, http://adg.stanford.edu/aa241/AircraftDesign.html, last visited on November 24th, 2011.

[9] Chun, M., Niu, Y. (1988). Airframe Structural Design. California: Conmilit Press Ltd.

[10] Defence Industry Daily, http://www.defenseindustrydaily.com/france-modernizing-alpha-jet-trainer-avionics-04661/, last visited on November 24th, 2011.

[11] Seshu, P. (2006, June). Finite Element Analysis. Prentice Hall.

[12] Pepper, D. W., Heinrich J. C. (1992). The Finite Element Method: Basic Concepts and Applications. US: Hemisphere Publishing Corporation.

[13] Chandrupatla, T. R. (2004). Finite Element Analysis for Engineering and Technology. India: Universities Press.

[14] Bhavikatti, S.S. (2005). Finite Element Analysis. New Delhi: New Age Publishers.

[15] Liu, G.R., Quek, S.S. (2003). The Finite Element Method: A Practical Course. UK: Elsevier.

[16] Schaeffer, H.G. (2001). MSC.Nastran Primer for Linear Analysis. US: MSC.Software Corporation.

[17] *Practical Application of Finite Element Analysis to Aircraft Structural Design* (1986). AGARD Lecture Series No.147. US.

[18] Flight Global, http://www.flightglobal.com/airspace/media/militaryaviation1946-2006cutaways/images/82812/aermacchi-m346-cutaway-drawing.jpg, last visited on November 28th, 2011.

[19] Montana State University, College of Engineering, Introduction to Aerospace Lecture Notes, http://www.coe.montana.edu/me/faculty/cairns/Introduction%20to%20Aerospace-Web/Internal%20Loads.pdf, last visited on November 28th, 2011.

[20] *An Assessment of the State-of-the-art in Multidisciplinary Aeromechanical Analyses* (2008, January). AMES Research Center Report. US.

[21] Chun, M., Niu, Y. (1999). Airframe Stress Analysis and Sizing. Hong Kong: Conmilit Press Ltd.

[22] ANSYS®, User's Manual for Revision 5.1, ANSYS® Inc., 1994

[23] ABAQUS®, User's Manual Version 6.4, ABAQUS® Inc., 2003

[24] MSC.NASTRAN®, User's Guide, MSC.Software©, 2001

[25] Sharpe, Jr., William N. (2008). Springer Handbook of Experimental Solid Mechanics. New York: Springer.

[26] Window, A.L. (1992, November). Strain Gauge Technology. Springer.

[27] *Strain Gauge Measurements on Aircraft* (1976, April). AGARDograph No.160 Vol.7. London: Technical Editing and Reproduction Ltd.

[28] *Certification Specifications for Normal, Utility, Aerobatic, and Commuter Category Aero planes, CS-23-AMC 23.307*(2010, September). European Aviation Safety Agency.

[29] Vishay® Inc, http://www.vishaypg.com/docs/11298/250un.pdf, last visited on February 2nd, 2012.

[30] Vishay® Inc, http://www.vishaypg.com/docs/11225/125ur.pdf, last visited on February 2nd, 2012.

[31] Endevco® Inc, http://www.endevco.com/product/prodpdf/8540-500.pdf, last visited on February 2nd, 2012.

[32] National Instruments®, http://www.ni.com/pdf/manuals/375102d.pdf, last visited on February 2nd, 2012.

[33] National Instruments®, http://sine.ni.com/nips/cds/view/p/lang/en/nid/208800,last visited on February 2nd, 2012.

[34] LabVIEW User Manual, National Instruments® Inc., 2011

[35] University of Glasgow, http://www.mech.gla.ac.uk/~sharpj/strain_extra.pdf, last visited on February 3rd ,2012.